N°d'ordre NNT : xxx

THESE de DOCTORAT DE L'UNIVERSITE DE LYON
opérée au sein de
l'Ecole des Mines de Saint-Etienne

Ecole Doctorale N° 488
Sciences, Ingénierie, Santé

Spécialité de doctorat : Science et Génie des Matériaux

Soutenue publiquement le 11.03.2019 , par :
Antonios Choleridis

Experimental and Mechanical Analysis of Wear-Induced Delamination for DLC Coated Automotive Components

Devant le jury composé de :

Professeur Jean Denappe	ENI Tarbes	Rapporteur
Professeur Jean-Yves Buffière	INSA Lyon	Rapporteur
Professeur Ali Erdemir	Argonne National Laboratory	Examinateur
Directeur de recherches Etienne Barthel	ESPCI Paris	Examinateur
Ingénieur de recherches Sylvie Descartes	INSA Lyon	Examinatrice
Ingénieur de recherches Marie-Alix Leroy	IREIS, HEF Group	Examinatrice
Directeur de recherches Helmut Klöcker	Mines Saint Etienne	Directeur de thèse
Professeur Christophe Donnet	UJM Saint Etienne	Directeur de thèse
Ingénieur de recherches Sergio Sao-Joao	Mines Saint Etienne	Co-encadrant de thèse

Spécialités doctorales	**Responsables :**	**Spécialités doctorales**	**Responsables**
SCIENCES ET GENIE DES MATERIAUX	K. Wolski Directeur de recherche	MATHEMATIQUES APPLIQUEES	O. Roustant, Maître-assistant
MECANIQUE ET INGENIERIE	S. Drapier, professeur	INFORMATIQUE	O. Boissier, Professeur
GENIE DES PROCEDES	F. Gruy, Maître de recherche	SCIENCES DES IMAGES ET DES FORMES	JC. Pinoli, Professeur
SCIENCES DE LA TERRE	B. Guy, Directeur de recherche	GENIE INDUSTRIEL	N. Absi, Maitre de recherche
SCIENCES ET GENIE DE L'ENVIRONNEMENT	D. Graillot, Directeur de recherche	MICROELECTRONIQUE	Ph. Lalevée, Professeur

EMSE : Enseignants-chercheurs et chercheurs autorisés à diriger des thèses de doctorat (titulaires d'un doctorat d'État ou d'une HDR)

ABSI	Nabil	MR	Génie industriel	CMP
AUGUSTO	Vincent	CR	Image, Vision, Signal	CIS
AVRIL	Stéphane	PR2	Mécanique et ingénierie	CIS
BADEL	Pierre	MA(MDC)	Mécanique et ingénierie	CIS
BALBO	Flavien	PR2	Informatique	FAYOL
BASSEREAU	Jean-François	PR	Sciences et génie des matériaux	SMS
BATTON-HUBERT	Mireille	PR2	Sciences et génie de l'environnement	FAYOL
BEIGBEDER	Michel	MA(MDC)	Informatique	FAYOL
BLAYAC	Sylvain	MA(MDC)	Microélectronique	CMP
BOISSIER	Olivier	PR1	Informatique	FAYOL
BONNEFOY	Olivier	PR	Génie des Procédés	SPIN
BORBELY	Andras	MR(DR2)	Sciences et génie des matériaux	SMS
BOUCHER	Xavier	PR2	Génie Industriel	FAYOL
BRODHAG	Christian	DR	Sciences et génie de l'environnement	FAYOL
BRUCHON	Julien	MA(MDC)	Mécanique et ingénierie	SMS
CAMEIRAO	Ana	MA(MDC)	Génie des Procédés	SPIN
CHRISTIEN	Frédéric	PR	Science et génie des matériaux	SMS
DAUZERE-PERES	Stéphane	PR1	Génie Industriel	CMP
DEBAYLE	Johan	MR	Sciences des Images et des Formes	SPIN
DEGEORGE	Jean-Michel	MA(MDC)	Génie industriel	Fayol
DELAFOSSE	David	PR0	Sciences et génie des matériaux	SMS
DELORME	Xavier	MA(MDC)	Génie industriel	FAYOL
DESRAYAUD	Christophe	PR1	Mécanique et ingénierie	SMS
DJENIZIAN	Thierry	PR	Science et génie des matériaux	CMP
BERGER-DOUCE	Sandrine	PR1	Sciences de gestion	FAYOL
DRAPIER	Sylvain	PR1	Mécanique et ingénierie	SMS
DUTERTRE	Jean-Max	MA(MDC)		CMP
EL MRABET	Nadia	MA(MDC)		CMP
FAUCHEU	Jenny	MA(MDC)	Sciences et génie des matériaux	SMS
FAVERGEON	Loïc	CR	Génie des Procédés	SPIN
FEILLET	Dominique	PR1	Génie Industriel	CMP
FOREST	Valérie	MA(MDC)	Génie des Procédés	CIS
FRACZKIEWICZ	Anna	DR	Sciences et génie des matériaux	SMS
GARCIA	Daniel	MR(DR2)	Sciences de la Terre	SPIN
GAVET	Yann	MA(MDC)	Sciences des Images et des Formes	SPIN
GERINGER	Jean	MA(MDC)	Sciences et génie des matériaux	CIS
GOEURIOT	Dominique	DR	Sciences et génie des matériaux	SMS
GONDRAN	Natacha	MA(MDC)	Sciences et génie de l'environnement	FAYOL
GONZALEZ FELIU	Jesus	MA(MDC)	Sciences économiques	FAYOL
GRAILLOT	Didier	DR	Sciences et génie de l'environnement	SPIN
GROSSEAU	Philippe	DR	Génie des Procédés	SPIN
GRUY	Frédéric	PR1	Génie des Procédés	SPIN
HAN	Woo-Suck	MR	Mécanique et ingénierie	SMS
HERRI	Jean Michel	PR1	Génie des Procédés	SPIN
KERMOUCHE	Guillaume	PR2	Mécanique et Ingénierie	SMS
KLOCKER	Helmut	DR	Sciences et génie des matériaux	SMS
LAFOREST	Valérie	MR(DR2)	Sciences et génie de l'environnement	FAYOL
LERICHE	Rodolphe	CR	Mécanique et ingénierie	FAYOL
MALLIARAS	Georges	PR1	Microélectronique	CMP
MOLIMARD	Jérôme	PR2	Mécanique et ingénierie	CIS
MOUTTE	Jacques	CR	Génie des Procédés	SPIN
NAVARRO	Laurent	CR		CIS
NEUBERT	Gilles			FAYOL
NIKOLOVSKI	Jean-Pierre	Ingénieur de recherche	Mécanique et ingénierie	CMP
NORTIER	Patrice	PR1	Génie des Procédés	SPIN
O CONNOR	Rodney Philip	MA(MDC)	Microélectronique	CMP
PICARD	Gauthier	MA(MDC)	Informatique	FAYOL
PINOLI	Jean Charles	PR0	Sciences des Images et des Formes	SPIN
POURCHEZ	Jérémy	MR	Génie des Procédés	CIS
ROUSSY	Agnès	MA(MDC)	Microélectronique	CMP
ROUSTANT	Olivier	MA(MDC)	Mathématiques appliquées	FAYOL
SANAUR	Sébastien	MA(MDC)	Microélectronique	CMP
SERRIS	Eric	IRD		FAYOL
STOLARZ	Jacques	CR	Sciences et génie des matériaux	SMS
TRIA	Assia	Ingénieur de recherche	Microélectronique	CMP
VALDIVIESO	François	PR2	Sciences et génie des matériaux	SMS
VIRICELLE	Jean Paul	DR	Génie des Procédés	SPIN
WOLSKI	Krzystof	DR	Sciences et génie des matériaux	SMS
XIE	Xiaolan	PR0	Génie industriel	CIS
YUGMA	Gallian	CR	Génie industriel	CMP

Mise à jour : 30/08/2018

Table of contents

General Introduction

Amorphous Diamond-Like Carbon (DLC) coatings are known for their outstanding properties such as low friction coefficients, and wear resistance. These properties allow a variety of technical applications (wear protection of cutting and forming tools, biomedical components, mechanical components). DLC coatings on moving automotive components lead to decreased fuel consumption (decreased friction coefficient) [1] and sustainable industrial development (reduced component wear). Worldwide, more than *100 million DLC coated automotive components per year* correspond to market volume of several 100 million € [2].

Moving automotive components undergo several in service degradation mechanisms (smooth wear, tribochemical wear…). Among all these mechanisms, local coating delamination is occasionally detected, in spite of the development of intermediate adhesion layers between the DLC film and the substrate. Vast efforts have been dedicated to the *theoretical* mechanical analysis of interface *crack* ***propagation*** *in model systems*. If the theoretical aspects of delamination and crack propagation mechanisms in "model" configurations are well understood, ***damage nucleation in real world components*** is still the open question. Enormous efforts have also been spent on experimental coating characterization. Bull presented a very interesting classification of thin film failure modes based on scratch test results. *However, in service damaged coatings exhibit* ***all*** *the listed failure modes*. Despite the major energies spent on debonding theory, no method to guarantee perfect working integrity of tribological films is available. Yet, for car (and bio-implant) manufacturers, the latter is mandatory.

The scientific objective of the present PhD is to develop a better understanding of the delamination process of DLC films by the development of a methodology to characterize delamination, blistering and crack propagation induced by severe tribological loading.

Present PhD will be organized as follows.

Delamination analysis implies the knowledge of the coating material. A short, non-exhaustive literature overview of today's knowledge on DLC will be given. This short overview will be followed by a presentation of the classical delamination and contact models. Since the first attempts to analyse experimentally coating delamination, the available equipment dedicated to the experiments was dramatically enhanced. Present work will make extensive use of the latest developments in surface characterization. For this reason, chapter 2 is completely dedicated to the synthetic presentation of coating elaboration and advanced characterization techniques as Atomic Force Microscopy, Focused Ion Beam milling and nano pillar compression.

The first two chapters define the state of the art as well as for the theoretical background concerning interface fracture as for the latest experimental techniques. Chapter 3 will be devoted to the experimental characterization of coating delamination during severe tribological loading. Blister topology, neighbourhood and interface cracks are analysed in function of the applied loading. The main results of this chapter have been published recently in Surface & Coatings Technology [3]. The tribological test used in present work leads to a network of blisters with a typical size and spacing. The blister nucleation mechanism was revealed by original SEM observations and very local chemical analysis after FIB milling. These original experimental observations concerning interface fracture cry out for a new model of the delamination of the thin hard DLC coatings. A first, very simple attempt, to model thin coating delamination is given in chapter 4.

This work is part of the scientific program of the LABEX MANUTECH-SISE, dedicated to surface and interface science and technology, as part of the scientific Axis “Knowledge-Based Design” dedicated to the investigation of surface concepts applied to challenging engineering applications in the field of low energy consumption.

[1] C.OULD, C.HEAU, J.FONTAINE, C.DONNET, Influence of hydrogen content on DLC tribological behavior: tests in mineral base oils, Proceedings of the World Tribology Congress (8-13 sept. 2013, Torino, Italy), Politecnico di Torino (editor), pp.640-643.

[2] K.BEWILOGUA, D.HOFMANN, History of diamond-like carbon films — From first experiments to worldwide applications, Surface & Coatings Technology 242 (2014) 214–225.

[3] A.CHOLERIDIS, S.SAO-JOAO, J.BEN-MOHAMED, D.CHERN, V.BARNIER, G.KERMOUCHE, C.HEAU, M.-A.LEROY, J.FONTAINE, S.DESCARTES, C.DONNET, H.KLOCKER, Experimental study of wear-induced delamination for DLC coated automotive components, Surface and Coatings Technology, 352 (2018) 549-560.

Chapter 1 State of the art

1.1 Diamond-Like-Carbon coatings

1.1.1 DLC: material structure and characteristics

Carbon is one of the most significant elements of the periodic table and can be found either in a crystalline or an amorphous structure (figure 1). It forms many other substances with notable properties such as high hardness and thermal conductivity for structures similar to diamond.

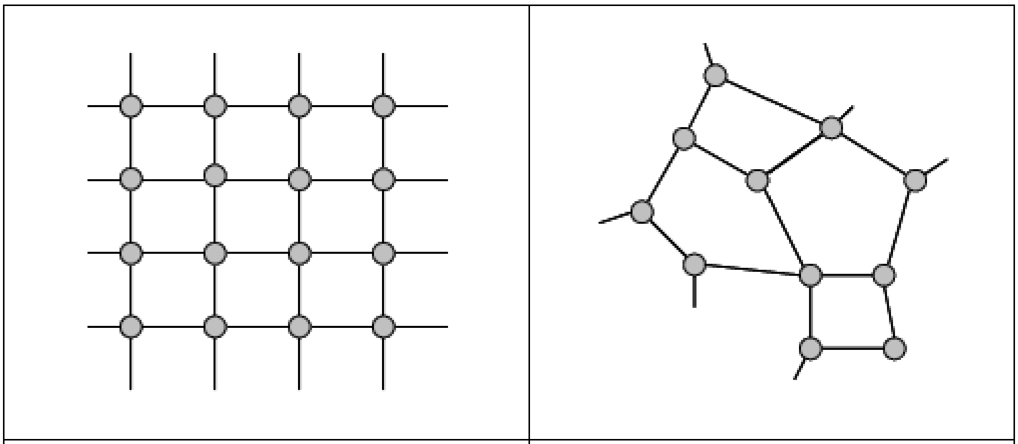

-a- -b-

Figure 1: Illustration of a crystalline (a) and an amorphous (b) arrangement of atoms [1]

Carbon can establish a wide variety of crystalline and disordered structures due to its ability to exist in three hybridizations, sp^3, sp^2 and sp^1 (figure 2).

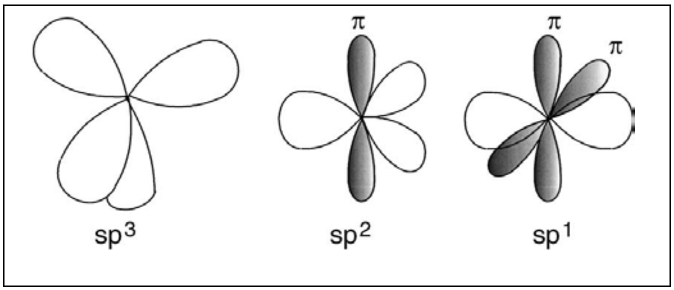

Figure 2: Carbon hybridized bonding [1]

One of these structures is the Diamond-Like-Carbon, a metastable form of amorphous carbon containing a significant fraction of sp^3 bonds [1]. Due to their interesting mechanical and tribological properties and performance characteristics, DLC films attract the attention of the scientific and the industrial community last 30-40 years. They are used in in a wide range of engineering applications to control friction and wear [2].

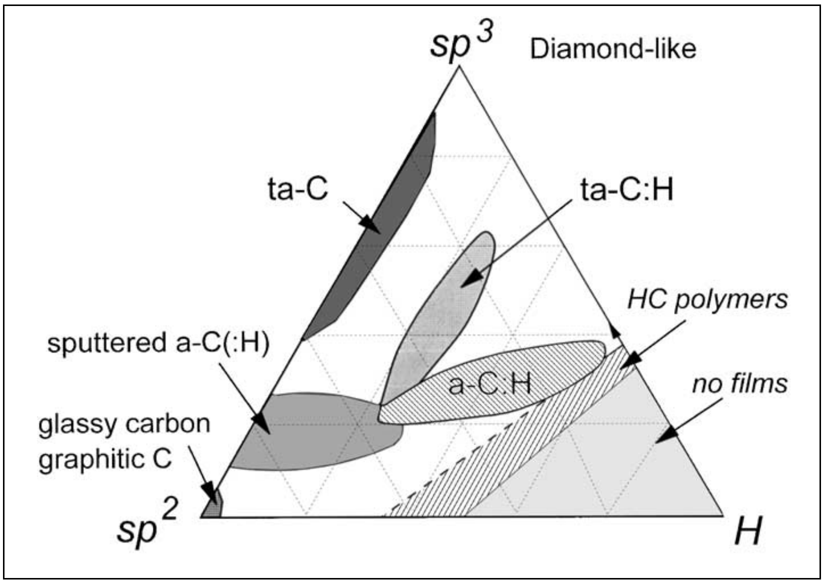

Figure 3: Ternary phase diagram of amorphous carbon-hydrogen alloys [1]

Figure 3 presents a ternary phase diagram, proposed by Robertson, illustrating the domains of several carbon-based coatings with respect to their sp^2 - sp^3 bonding and their content in hydrogen. The family of DLC coatings is one of the largest and has been studied extensively. Schmellenmeier [3] is one of the first to study these coating in early 50s. However, more detailed research was done two decades later by Eisenberg and Chabot [4] and a growth in interest in DLC films was noticed during the 90s [5,6].

The chemical composition of these films (hydrogen content or alloying elements) controls the resulting mechanical and tribological properties of the structure such as hardness and stiffness which plays an important role in their ability to carry the load and, consequently, their wear resistance [2]. An example of an amorphous a-C:H system is shown in figure 4. The black and grey points represent the sp^2 and sp^3 carbon atoms respectively. The white open circles are the hydrogen atoms [7].

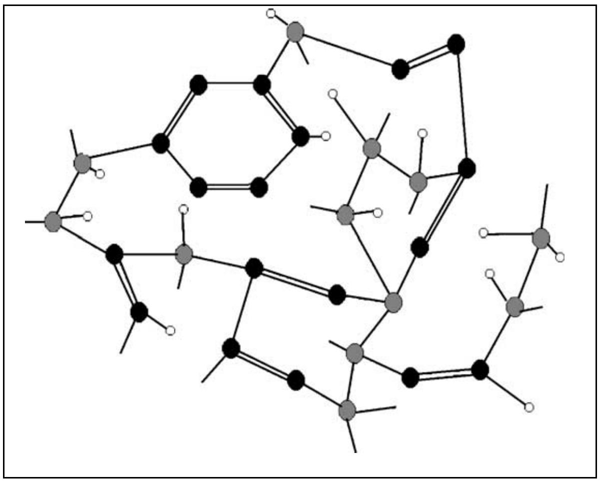

Figure 4: Schematic representation of amorphous Diamond-Like-Carbon [2]

Diamond-Like-Carbon presents some extreme properties similar to diamond, such as the hardness, elastic modulus and chemical inertness. Meanwhile, these properties are achieved in an isotropic disordered thin film without grain boundaries [1]. Moreover, production of these films is cheaper than diamond itself, and this is a huge advantage for various applications. Characteristic properties of several forms of amorphous carbon are presented in table 1 in comparison to diamond and graphite.

	sp^3 (%)	H (%)	Density (g cm^{-3})	Hardness (GPa)	Reference
Diamond	100	0	3.515	100	[8]
Graphite	0	0	2.267		[9]
Glassy C	0	0	1.3-1.55	3	[10]
Evaporated C	0	0	1.9	3	[10]
Sputtered C	5	0	2.2		[11]
ta-C	80-88	0	3.1	80	[11,12,13]
a-C:H hard	40	30-40	1.6-2.2	10-20	[14]
a-C:H soft	60	40-50	1.2-1.6	<10	[14]
ta-C:H	70	30	2.4	50	[15]

Table 1: Comparison between several amorphous carbons and reference materials

The industrial success of DLC coatings, especially in tribological applications, depends strongly on their adhesion properties. Typically, DLC films adhere well on substrates containing elements forming carbides [2]. Usually, in many applications, intermediate layers are deposited on the substrate prior to DLC film deposition.

1.1.2 DLC films interest and applications

DLC coatings are widely used at a significant part of industrial products. Their deposition on mechanical components covers a broad field of sectors including among others the automotive industry, aeronautic applications, biomedical parts production and machining equipment. They are usually applied for friction reduction and higher wear resistance of the coated mechanical part leading to an increased component lifetime. In some cases, especially in the automotive industry, they can reduce indirectly the fuel/energy consumption or even the emission of pollutants depending on the application. In automotive industry, DLC coatings typically work in lubricated conditions and lead to low friction between the surfaces in contact. They are generally deposited on steel substrates. However, the steel component should be carefully prepared depending on the application and its mechanical characteristics. Sometimes one or more intermediate layers are deposited onto the substrate prior to the DLC film deposition. This is the case of components subject to severe loadings. Of course, in order to deposit such a multilayer, adequate deposition processes are required. Moreover, the surface of the substrate to be coated should be carefully prepared. Its roughness needs to be smaller than a typical threshold in order to ensure the successful adhesion between the coating and the substrate. On the coated part, high roughness can cause local coating failure due to stress concentration. In the following subsections some usual applications of DLC films will be presented.

1.1.2.1 DLC automotive and industrial applications

Diesel injection system

During the last decades, DLC coatings found widespread industrial application in the enhancement of fuel injection systems of the diesel engines. The increased injection pressure inside a modern diesel motor, forced the automotive constructors to apply coatings on injection parts [16]. Typically, a multilayer is deposited having a top layer of DLC, usually of a-C:H structure.

Internal combustion engine components

The high loads encountered in modern engines under elevated pressures, especially in turbo motors, led to the use of hard surface coatings on several parts of the valve train system such as tappets (figure 5a), crankshaft components and piston pins (figure25b).

-a- -b-

Figure 5: DLC coating on a tappet (a) and on piston pins (b) [17]

The use of DLC coatings on tappets started at early 2000s and increased steadily until nowadays. About 10% of coated tappets have a DLC-family film as top layer. The cost reduction of mechanical components is the driving force for DLC coatings on piston pins [2].

Gears

In the last decades, application of DLC films on gears was boosted by the important friction coefficient reduction which and the resultant lower failure rate due to micropitting [18]. The advantage of these coatings is that, due to their good tribological properties, they can extend the period until catastrophic failure in the case of an unexpected loss of lubrication conditions [19]. This could be the case of a helicopter for example or a large windmill where the maintenance can be more expensive than the DLC film deposition.

Cutting tools

DLC coatings are also used on cutting tools. Typically this kind of films are deposited on aluminum or steel substrates. They can cover drills providing good performance by maintaining the cutting effort at low levels and preventing an increase in temperature. They also facilitate the chip evacuation and prevent the sticking on the tool.

1.1.2.2 Biomedical use of DLC protective films

Diamond-Like-Carbon presents interesting tribological properties and is compatible with the human body (chemical inert). Many in vivo and in vitro experiments show that DLC is biocompatible. Moreover, it can reduce the wear independently of the lubricated conditions leading to an improved tribological performance. This interesting combination is the driving force for the biomedical use of DLC films.

Figure 6: DLC-coated head of a hip joint [2]

For these reasons, DLC coatings have been applied in several artificial implants. One of the most well-known applications of DLC in bioengineering is the thin DLC layer deposited on hip joint implants (figure 6). However, some unexpected problems were highlighted recently [20], such as the reaction of the body fluids with the wear products.

1.1.3 Deposition techniques of DLC coatings

Through the last decades several deposition methods have been developed to produce amorphous carbon films with mixed sp^2 and sp^3 bonding. Depending on the sp^2/sp^3 fraction as well as the content in hydrogen, various structures can be obtained (a-C, a-C:H, ta-C:H etc.). Some deposition techniques are more suitable and preferable to achieve specific DLC compositions. For example, plasma enhanced chemical vapor deposition (PECVD) can reach the interior of the ternary phase diagram presented in figure 3, producing a-C:H films [14]. Moreover, some methods are more suitable for industrial production whereas others for laboratory study. Some of the principal and widely used deposition techniques will be discussed in the following paragraphs.

1.1.3.1 Ion assisted sputtering

One of the first DLC films was prepared using ion beam deposition [21]. In this method, the DLC film is condensed from a beam containing medium energy (~100eV) carbon or hydrocarbon ions [1]. These ions induce the sp^3 bonding in the growing film. Thus, it consists a physical process.

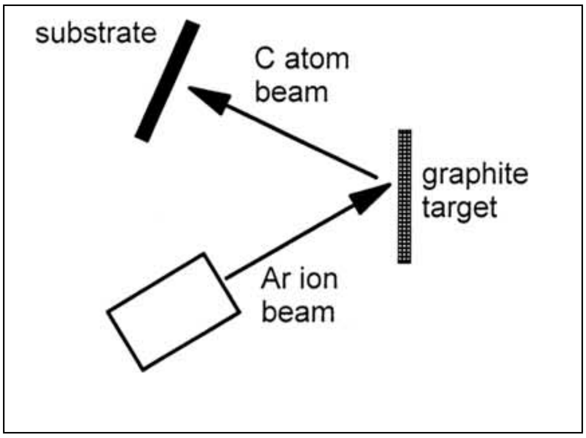

Figure 7: Ion assisted sputtering deposition [1]

In a typical ion beam deposition system, carbon ions are produced by the plasma sputtering of a graphite cathode in an ion source [22,23]. Alternatively, a hydrocarbon gas is ionized by a plasma. An ion beam is then extracted through a grid from the plasma source by a bias voltage. The carbon or hydrocarbon ions are then accelerated to form the ion beam in the high vacuum deposition chamber.

1.1.3.2 Sputtering

DLC deposition using sputtering is one of the most common industrial processes [24,25]. Typically, the DC or radio frequency (RF) sputtering of a graphite electrode by an Ar plasma is used. To increase the deposition rate, magnetron sputtering is often implemented (figure 8).

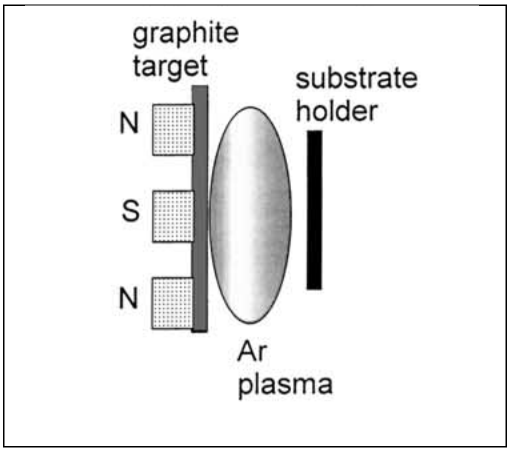

Figure 8: Sputtering deposition [1]

Magnets are placed behind the target to cause the electrons to spiral and increase their path length and therefore to increase the degree of ionization of the plasma [1]. As ion bombardment helps the formation of sp^3 bonding, the magnetic field can be configured to enhance the ionization rate (responsible for plasma densification and deposition rate increase) and to pass across to the substrate, enabling Ar ions to also bombard the substrate. A DC bias can be applied to the substrate to vary the ion energy.

1.1.3.3 Cathodic vacuum arc

A not so common method either for laboratory or for industrial production of coatings is the cathodic vacuum arc deposition. An arc initiated in a high vacuum by touching the graphite cathode with a small carbon striker electrode and withdrawing the striker.

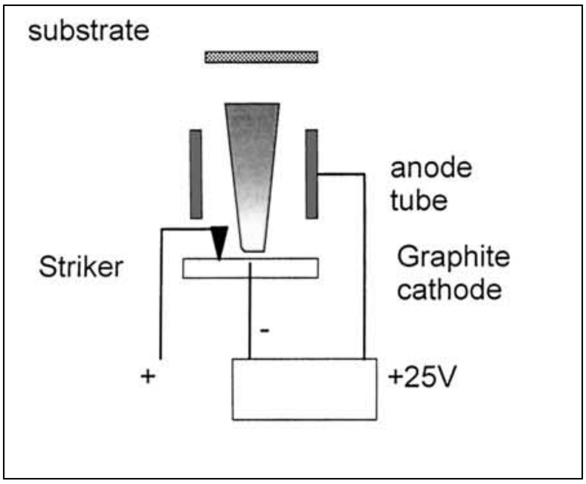

Figure 9: Cathodic arc deposition [1]

The latter, produces an energetic plasma with a high ion density [26]. This technique is widely used to deposit hard coating materials, but is less extensively carried out for DLC deposition. This method is developed to deposit more particularly ta-C, with high Csp^3 content.

1.1.3.4 Pulsed laser deposition

Pulsed excimer lasers give very short, intense energy pulses capable of vaporizing materials as an intense plasma [1,27,28] which, then, expands towards the substrate. A schematic representation of this method is shown in figure 10.

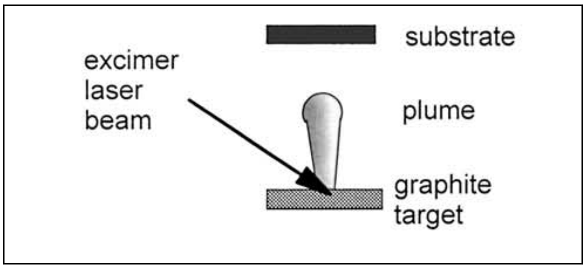

Figure 10: Pulsed laser deposition [1]

The mean ion energy is proportional to the laser fluence concentrated at the target spot. The advantage of the pulsed laser deposition is that it is a laboratory scale method which can be used for several materials' deposition, from superconductors to hard coatings [1,29].

1.1.3.5 Plasma assisted deposition

The most popular deposition technique is the plasma enhanced chemical vapor deposition (PECVD) illustrated in figure 11.

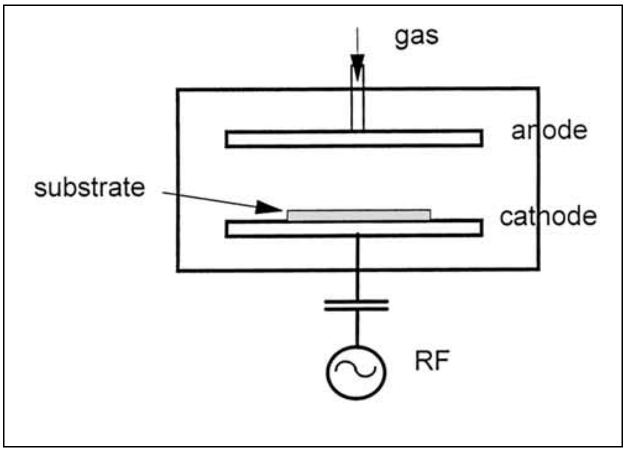

Figure 11: Pulsed laser deposition [1]

The deposition process includes the use of two electrodes. The first one is earthed while the other is connected to the radio frequency power supplier. On the latter, the substrate is mounted. A plasma is produced between the electrodes with the aid of reacting gases introduced into the chamber. The plasma develops a positive voltage. The radio frequency voltage is divided between the electrodes. The electrode with smaller capacitance requires larger bias voltage and becomes negative with respect to the other. This electrode is the substrate one. Positive ions are accelerated due to the negative voltage and bombard the surface of the substrate. In order to deposit DLC coatings, the lowest pressure is needed to maximize the fraction of the plasma [1, 31].

1.1.4 Residual stresses after film deposition

1.1.4.1 Stresses in a thin film

During the deposition process of a thin film on a thick substrate residual stresses arise. These stresses have intrinsic or thermal origins. Intrinsic stresses did not concern thermal expansion mismatches. They, usually, appear after a change in volume which creates stresses due to the constraint of the substrate or other layers. Estimation of the intrinsic stresses is mostly obtained by experimental measurements. Thermal stresses are due to the change in temperature during deposition [32] and thermal expansion coefficient mismatch between substrate and coating. In the following analysis a very thin film on a thick substrate (h/H<<1) is considered. Both of them are considered isotropic with different Young's modulus (E), Poisson's ratio (v) and coefficient of thermal expansion (α). Moreover, only stresses far away from the edges are taken into consideration.

A thin film deposited at temperature T_0 presents intrinsic stresses: $\sigma_{11}=\sigma_{22}=\sigma^I$ with possible variation through the thickness of the film (direction 3). An elastic response is assumed. The temperature variation is represented by: $\Delta T=T-T_0$. If the resulting stress change is expressed as $\Delta\sigma_{ij}$ then the total stress will be: $\sigma_{ij}=\sigma_{ij}^I + \Delta\sigma_{ij}$. Consequently, ε_{ij} are the strains relative to the state at T_0. In the case of thin films, the influence of the film on the substrate is small and the substrate imposes its inplane strains on the film (eq. 1.1):

$$\left(\varepsilon_{\alpha\beta}\right)_{\text{film}} = \left(\varepsilon_{\alpha\beta}\right)_{\text{substrate}} \tag{1.1}$$

Bending of the film is not taken into account for the moment. It will be analyzed in the following paragraphs. Thus for both the film and the substrate strains can be described by eq.1.2:

$$\varepsilon_{\alpha\beta} = \alpha_S \Delta T \delta_{\alpha\beta} \tag{1.2}$$

Note, this equation is valid for a CTE independent of the temperature. The component ε_{33} of the film is considered unconstrained thus $\sigma_{33}=0$ corresponding to plane stress conditions. The inplane components in the film should satisfy then the equation:

$$\varepsilon_{\alpha\beta} = \frac{1+\nu}{E}\Delta\sigma_{\alpha\beta} - \frac{\nu}{E}\Delta\sigma_{\gamma\gamma}\delta_{\alpha\beta} + \alpha\Delta T\delta_{\alpha\beta} \tag{1.3}$$

Which solving for the stress becomes:

$$\Delta\sigma_{\alpha\beta} = \frac{E}{1-\nu^2}\left[\left(1-\nu\right)\varepsilon_{\alpha\beta} + \nu\varepsilon_{\gamma\gamma}\delta_{\alpha\beta}\right] - \frac{E\alpha\Delta T}{1-\nu}\delta_{\alpha\beta} \tag{1.4}$$

And because of the eq.1.2 we obtain the thermal stress in the interior of the film:

$$\Delta\sigma_{\alpha\beta} = \frac{E\Delta\alpha\Delta T}{1-\nu}\delta_{\alpha\beta} \tag{1.5}$$

$$\Delta\sigma_{33} = 0 \tag{1.6}$$

where α and β represent directions 1 and 2 respectively and Δα is the coefficient of thermal expansion mismatch between the film and the substrate.

Finally, the film is subject to the equi-biaxial inplane stress state:

$$\sigma^R = \sigma^I + \frac{E\Delta\alpha\Delta T}{1-\nu} \tag{1.7}$$

1.1.4.2 Stresses in a multilayer

Let's take into consideration a multilayer with N layers as shown in figure 12. The intrinsic stress and deposition temperature for the 'i^{th}' layer are denoted as σ_i^I and T_0^i respectively.

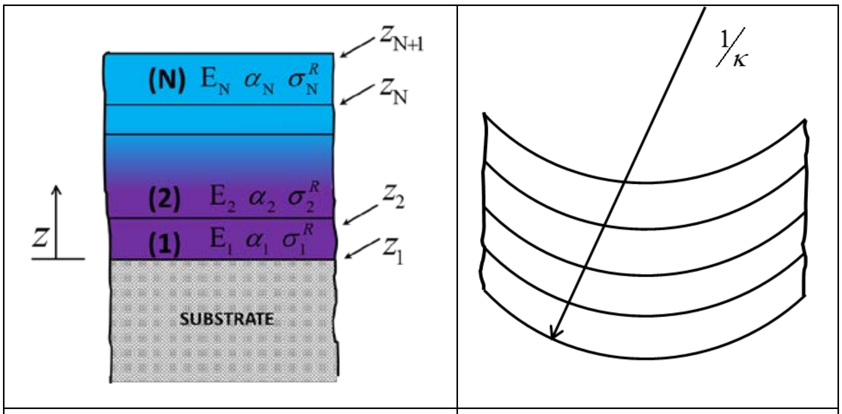

- a - - b -

Figure 12 : Multilayer deposition on thick substrate (a) and release of the multilayer from the substrate (b)

Subscript i denotes the number of the layers. Thus, in each layer at a given temperature T, the stress is:

$$\sigma_i^R = -\frac{E_i(\alpha_i - \alpha_S)}{(1-\nu_i)}\left(T - T_0^i\right) + \sigma_i^I \tag{1.8}$$

where $\sigma_{11} = \sigma_{22} = \sigma_i^R$.

If we consider that the multilayer is released from the substrate at temperature T, the in-plane strain change relative to the attached state is:

$$\Delta\varepsilon_{11} = \Delta\varepsilon_{22} \equiv \Delta\varepsilon = \Delta\varepsilon_0 - z\kappa \tag{1.9}$$

where $\Delta\varepsilon_0$ is the value at the bottom of the multilayer (z=0) and κ is the curvature change at the release. Thus, the inplane stress change in the ith layer after release is:

$$\Delta\sigma_{11} = \sigma_{22} \equiv \Delta\sigma = \frac{E_i}{(1-\nu_i)}\left(\Delta\varepsilon_0 - z\kappa\right) \tag{1.10}$$

And the total stress in the ith layer can be calculated by:

$$\sigma = \sigma_i^R + \Delta\sigma = \frac{E_i}{(1-\nu_i)}\left(\Delta\varepsilon_0 - z\kappa\right) + \sigma_i^R \tag{1.11}$$

Equilibrating forces (eq.1.12) and moments (eq.1.13) in the multilayer leads to the linear system (1.14-1.15) of equations for the two unknowns $\Delta\varepsilon_0$ and κ.

$$\int_0^{Z_{N+1}} \sigma dz = 0 \quad , \quad \int_0^{Z_{N+1}} \sigma z dz = 0 \tag{1.12-1.13}$$

This system is shown below:

$$C_{11}\Delta\varepsilon_0 - C_{12}\kappa = A_1 \tag{1.14-1.15}$$

$$C_{12}\Delta\varepsilon_0 - C_{22}\kappa = A_2$$

The components of C are defined in eqs.1.16-1.18:

$$C_{11} = \sum_{i=1}^{N} \frac{E_i t_i}{(1-\nu_i)} \tag{1.16}$$

$$C_{12} = \sum_{i=1}^{N} \frac{E_i\left(z_{i+1}^2 - z_i^2\right)}{2(1-\nu_i)} \tag{1.17}$$

$$C_{22} = \sum_{i=1}^{N} \frac{E_i\left(z_{i+1}^3 - z_i^3\right)}{3(1-\nu_i)} \tag{1.18}$$

The second hand vector A is given in eq. 1.19-1.20:

$$A_1 = -\sum_{i=1}^{N} t_i \sigma_i^R \tag{1.19}$$

$$A_2 = -\sum_{i=1}^{N} \frac{1}{2}\left(z_{i+1}^2 - z_i^2\right)\sigma_i^R \tag{1.20}$$

$z=z_{i+1}$ designates the top of the ith layer and $z=z_i$ its bottom.

Once the in-plane strain change $\Delta\varepsilon_0$ and the curvature κ are calculated, the average stress (eq. 1.21) in the ith layer can be determined by:

$$\bar{\sigma} = \frac{E_i}{(1-\nu_i)}\left[\Delta\varepsilon_0 - \frac{1}{2}(z_i + z_{i+1})\kappa\right] + \sigma_i^R \tag{1.21}$$

If a bilayer is considered (N=2), and under the assumption that both layers are deposited at the same temperature T_0 with zero intrinsic stresses, then a relation between the average stress in the film and its curvature can be established.

Previously presented equations for the stress at the top of the layer 2 and its average stress can be expressed as follows:

$$\xi = \frac{h_2}{h_1} \tag{1.22}$$

For DLC coatings analyzed here, the film thickness h_2 is much smaller than the substrate thickness h_1. Hence $\xi << 1$. Typical values to be considered in present work are:

ξ=0.2/400 то 2.5/400 in the deflection test on coated Si wafers,

ξ=0.2/5000 то 2.5/5000 in the tribological test samples (M2-steel coated samples).

$$\Sigma = \frac{E_2/(1-\nu_2)}{E_1/(1-\nu_1)} \tag{1.23}$$

Σ represents the ratio of film (coating) and substrate plane strain moduli. For hard coatings, Σ will be larger than 1. In the following chapter the reduced modulus of the DLC will be shown to be much larger than the corresponding modulus of the substrate steel.

$$\sigma^T = \frac{E_2}{(1-\nu_2)}(\alpha_1 - \alpha_2)(T - T_0) \tag{1.24}$$

σ^T / E_2 increases with high deposition temperatures (large $(T - T_0)$) and large misfits in the thermal expansion coefficients. The misfit stress is proportional to the film Young's modulus. Hard coatings tend thus to exhibit large misfit stresses.

$$\frac{\bar{\sigma}}{\sigma^T} = \frac{1 + \Sigma\xi^3}{\left(\Sigma\xi^2 - 1\right)^2 + 4\Sigma\xi(\xi + 1)^2} \tag{1.25}$$

$$\frac{\sigma}{\sigma^T} = \frac{1 - 3\Sigma\xi^2 - 2\Sigma\xi^3}{\left(\Sigma\xi^2 - 1\right)^2 + 4\Sigma\xi(\xi + 1)^2} \tag{1.26}$$

Consequently, the curvature can be calculated by:

$$\kappa = \frac{6\xi^2(1+\xi)}{\left(\Sigma\xi^2 - 1\right)^2 + 4\Sigma\xi(\xi + 1)^2}\left[\frac{(1-\nu_1)\sigma^T}{E_1 h_2}\right] \tag{1.27}$$

In these equations σ^T is the misfit stress, being the stress in the upper layer which would occur if the lower layer was infinitely thick ($\xi=h_2/h_1 \sim 0$). Thus, the average residual stress is essentially the misfit stress when the film is thin.

For small Σ, there is no important variation of stress values and misfit stress can be eliminated:

$$\kappa = \frac{1+\xi}{1+\Sigma\xi^3}\frac{6(1-\nu_1)h_2\overline{\sigma}}{E_1h_1^2} \tag{1.28}$$

For $\xi \ll 1$ and $\Sigma\xi^3 \ll 1$, we can obtain the well-known relation, first presented by Stoney [32]:

$$\kappa = \frac{6(1-\nu_1)h_2\overline{\sigma}}{E_1h_1^2} \tag{1.29}$$

$\Sigma\xi^3 \ll 1$ is always satisfied for coatings in the range of 0.2µm to 2.5µm on substrates thicker than 400µm.

This relation (1.29) links the average stress in the film to the curvature and in the absence of external loading allows the determination of residual stress with a simple measurement of the film's curvature.

1.1.5 Typical adherence testing of DLC coatings

Once the multilayered film is deposited to the substrate its adhesion is tested with standard experimental techniques presented below. Note, these techniques are mostly qualitative and lead to general characteristics of the coating although they are commonly implemented tools in coatings' characterization for engineers.

1.1.5.1 Rockwell Indentation

The Rockwell method is a commonly applied technique for adhesion testing of coatings. Typically, a conventional Rockwell hardness test is carried out followed by an analysis of the network of coating cracks and flaking around the edges of the indentation using an optical microscope (figure 13).

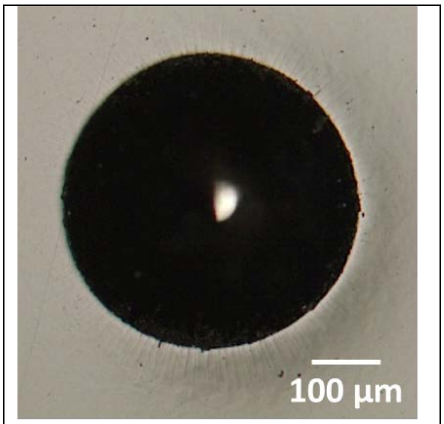

Figure 13: Rockwell indentation test: optical view of a typical imprint

Coating's adhesion is then assigned to one of the following six adhesion classes (figure 14).

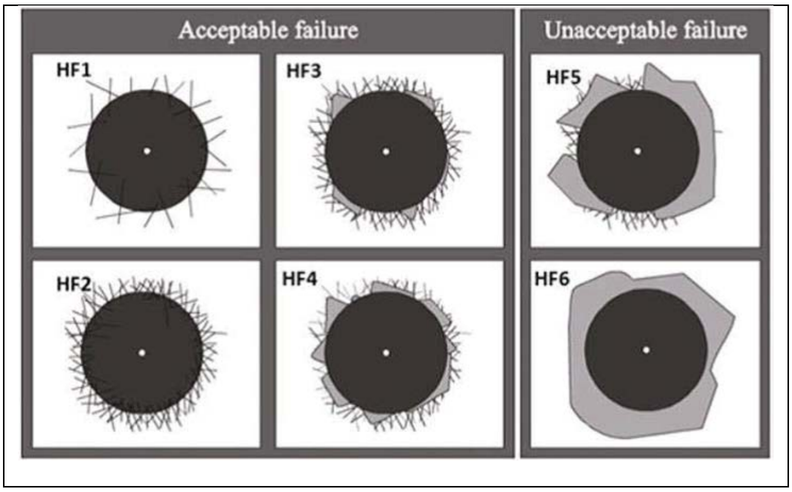

Figure 14: Adhesion classes of Rockwell indentation imprints [2]

The presence of micro-cracks in a network around the imprint (thinner HF1 or thicker HF2) is considered as acceptable failure of the coating and doesn't reveal adhesion issues. Similarly, limited flaking (HF3 and HF4) is observed in some cases without proving poor adhesion between the coating and the substrate. On the contrary, large scale flaking (HF5 and HF6) leads to the conclusion that the adhesion is not sufficient enough and thus is characterized as unacceptable failure.

1.1.5.2 Scratch test

In order to assess the adhesion of thin had coatings the scratch test is a useful tool to develop coatings and assure their quality. Yet, due to several not adhesion-related intrinsic and extrinsic factors, the outcome of this test is semi-quantitative. The complexity of the stress state around a moving indenter scratching a coating/substrate system gives rise to difficulties in determining the stresses leading to detachment of the film. Furthermore, the interfacial defects responsible for failure are unknown. However, by a careful analysis of the observed failure modes in the scratch test (not all of which are related to adhesion) it is possible to identify adhesive failures and in some cases these occur in regions where the stress state is relatively simple and quantification can be attempted.

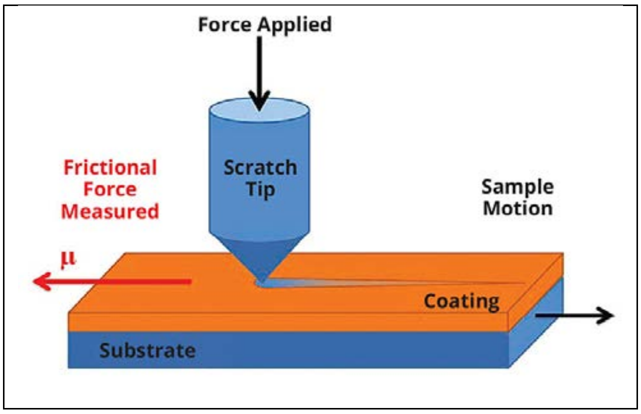

Figure 15: Schematic representation of the scratch test facility

The principle of this experiment is the following. A sharp diamond tip is scratching the surface of the sample with increasing predefined normal load. The result of this procedure is then observed with an optical microscope to analyze the failure of the coating/substrate system. An example of this observation is presented at figure 16.

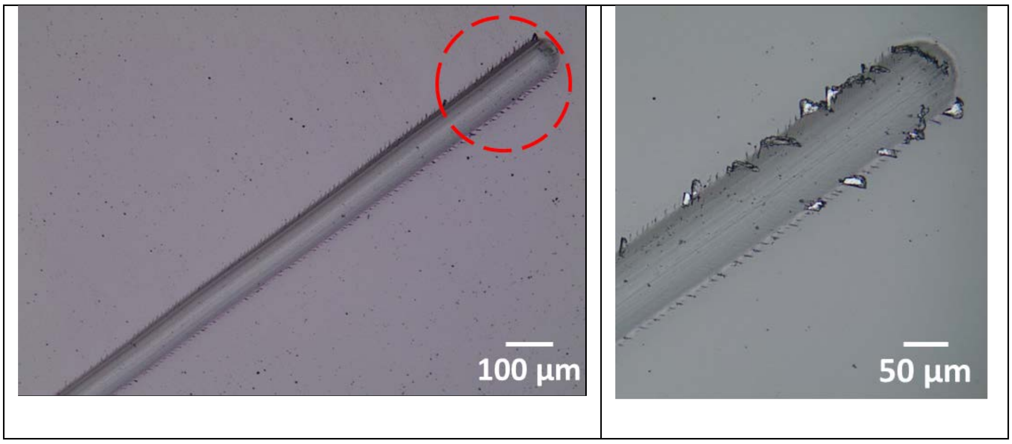

Figure 16: Typical observation of a scratch test imprint

However, even if, for adhesion analyses, the scratch test and Rockwell indentation are the most popular characterization techniques, they are not suitable for quantifying the in-service delamination analysis of DLC coatings. Enormous efforts have also been spent on experimental coating characterization. Numerous papers were dedicated to finite element simulations of these tests [35-37]. Steinmann et al. [38] presented a thorough experimental analysis of the intrinsic and extrinsic parameters influencing scratch test results on coated surfaces. Bull [39] presented a very interesting classification of thin film failure modes based on scratch test results. Drory and Hutchinson [40] published and overview of the best suited tests for characterizing coating adhesion. However, *in service* damaged coatings exhibit all the listed failure modes.

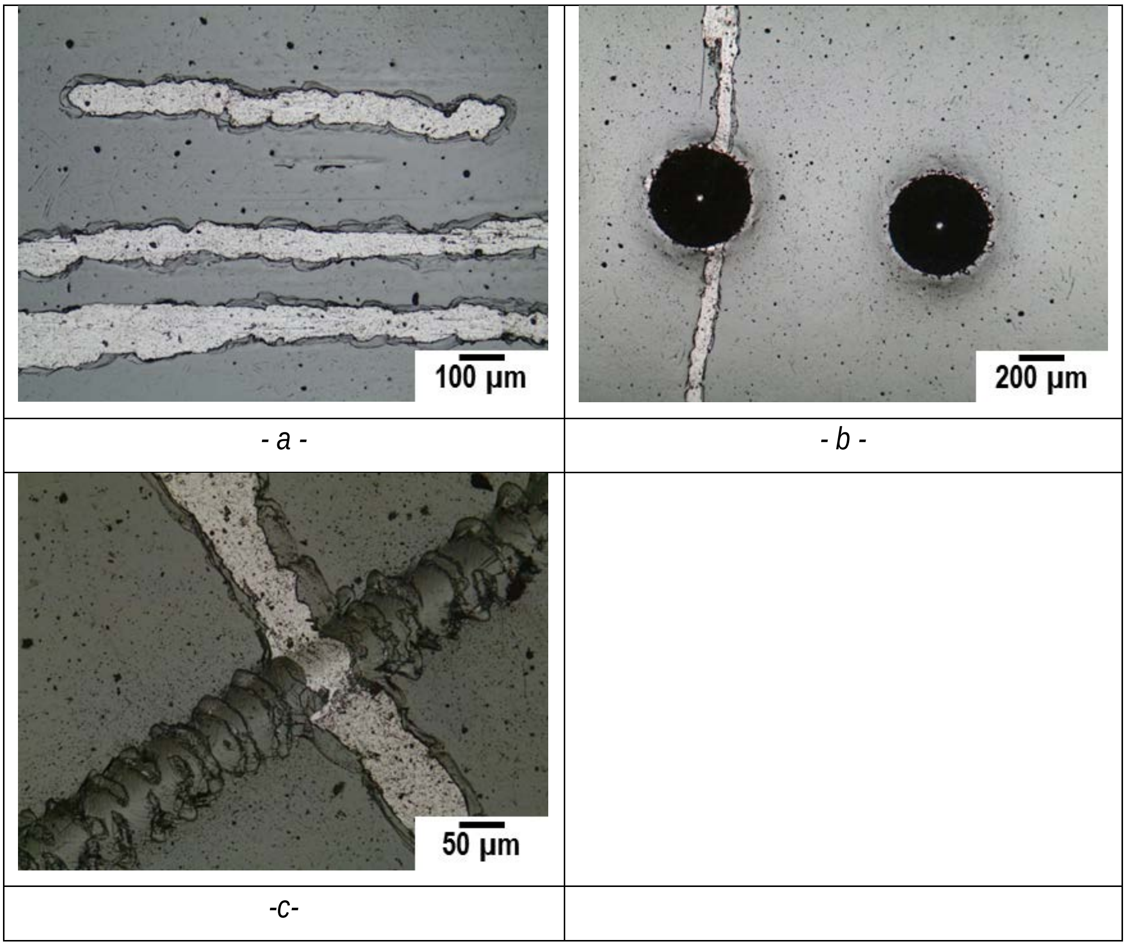

- a -

- b -

-c-

Figure 17: (a) Wear induced delamination, (b,c) Classical adhesion tests DLC coated M2 steel. (a) Scratch test: wear trace for 2 different loads (30 and 40 N). b Rockwell indentation on damaged coating [17]

Hence, *in service* coating delamination seems still enigmatic. Adhesion tests like scratch testing or Rockwell indentation carried out, after in service coating debonding, on the remaining film, reveal no adhesive failure (Figure 17b, c). The previous short literature survey highlights one major fact. Despite the major energies spent on debonding theory, no method to guarantee perfect *working* integrity of tribological films is available. Yet, for car manufacturers, the latter is mandatory. The purpose of the current thesis is to characterize and understand, in use, delamination failure mechanisms in apparent contradiction with classical adhesion tests.

1.2 Notions of interface and fracture mechanics

1.2.1 Crack propagation in homogeneous solids

Before analyzing interface crack mechanics, the principal notions of crack mechanics in homogeneous solids should be presented. In fracture mechanics there are several principal quantities defining the propagation conditions of a crack, the stress state around the crack tip as well as the material's resistance to crack propagation. An important quantity, first defined by Irwin, is the stress intensity factor

K_I, K_{II}, K_{III} depending on the mode of fracture (figure 18). Mode I concerns the opening of a crack, mode II is the in-plane shear and mode III corresponds to out-of-plane shear.

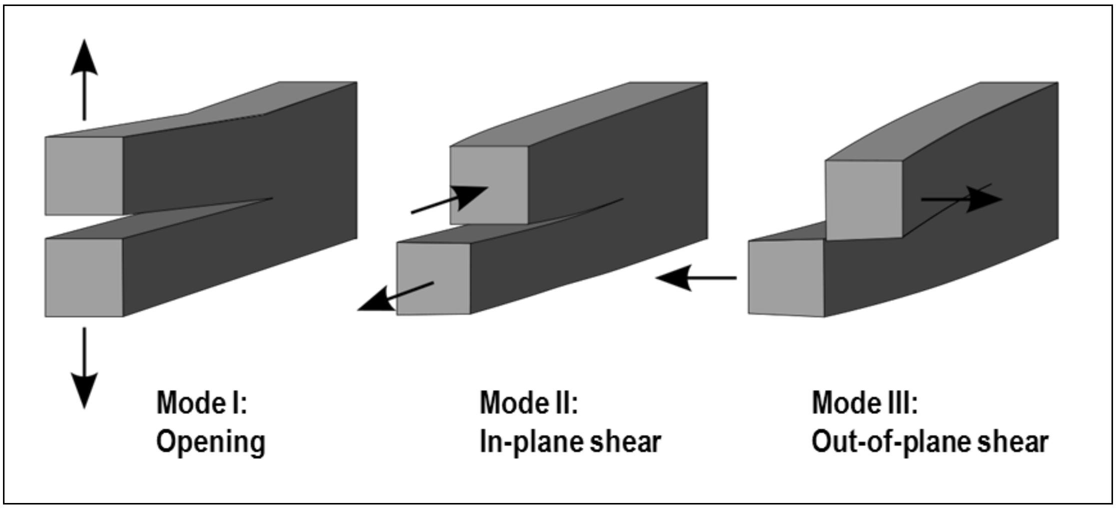

Figure 18: Fundamental modes of fracture [41]

The stress intensity factor (K) describes the severity of the stress state at a crack tip. To initiate crack propagation, the stress intensity factor (SIF) must reach a material defined threshold Kc, i.e. the toughness. Except fatigue induced crack propagation, the SIFs are not intended to describe crack propagation, but only the starting of crack propagation. The magnitude of K depends on the sample geometry, the size and the location of the crack, the magnitude of the remote loading as well as the distribution of the load. In linear elastic fracture mechanics, stress intensity factors have dimension stress x length$^{1/2}$.

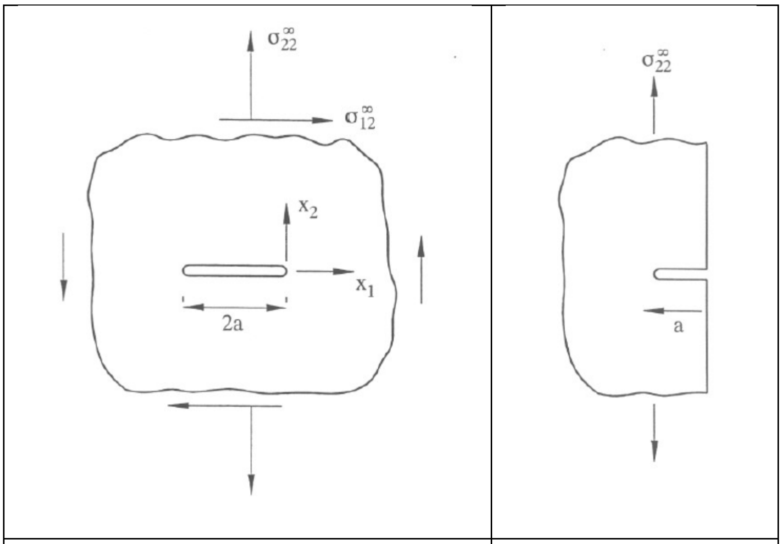

-a- -b-

Figure 19: Plane strain crack problem [43]

Tada, Paris and Irwin [42] defined stress intensity factors for several loading conditions. Two classical problems in fracture mechanics are shown in figure 19. In both cases, plain strain elasticity is considered. Figure 19a presents a straight crack of length 2a in an infinite body submitted to remote stresses σ_{ij}^{∞}. Axis x_1 is parallel to the crack while x_2 is vertical to the crack tip. The stress intensity factors for this problem are:

$$K_I = \sigma_{22}^{\infty}\sqrt{\pi a} \tag{1.30}$$

$$K_{II} = \sigma_{12}^{\infty}\sqrt{\pi a} \tag{1.31}$$

$$K_{III} = \sigma_{23}^{\infty}\sqrt{\pi a} \tag{1.32}$$

They depend only on the loading and the length of the crack. Material's properties such as Young's modulus and Poisson's ratio do not influence the stress intensity factor. Figure 17b illustrates the problem of an edge crack of length a in a semi-infinity half-space subject to remote stress σ_{12}^{∞} parallel to the free surface. In this case, the stress intensity factor reads:

$$K_I = 1.1215\sigma_{22}^{\infty}\sqrt{\pi a} \tag{1.33}$$

Another important quantity in fracture mechanics is the strain energy release rate (G). G designated the derivative of the potential Π with respect to the crack area A.

$$\begin{gathered} G = -\frac{d\Pi}{dA} \\ \Pi = U_{elast} - W_{ext} \end{gathered} \tag{1.34a}$$

The potential energy Π measures the difference between the internal elastic energy U_{elast} and the external work W_{ext}. A positive value of the energy release rate G (also called crack driving force), corresponds hence to either a decrease in the stored elastic energy U_{elast}, or a positive value of the external work delivered to the specimen. GdA measures the energy at disposal to increase the cracked are by a quantity dA. On the other hand, increasing the cracked area by dA will lead to energy dissipation of $2\gamma_s dA$. Designates the surface energy. The coefficient 2 arises because an increase in cracked area dA will lead to 2dA fresh surface, when considering the lower and upper crack lips. Hence, an elementary energy balance leads to the following result, valid in *linear elastic fracture mechanics*:

$$\begin{gathered} G < 2\gamma_s : \text{no propagation} \\ G \geq 2\gamma_s : \text{propagation} \end{gathered} \tag{1.34b}$$

The excess energy ($G>2\gamma_s$) is transformed into kinetic energy.

In a given state, G is independent of whether the load is prescribed or displacement is prescribed or any combination thereof. Irwin defined a connection for plane strain:

$$G = \frac{1-\nu^2}{E}\left(K_I^2 + K_{II}^2\right) \tag{1.35}$$

The energy release rate has dimensions of surface energy (~Jm^{-2}) in fracture mechanics. A similar approach may also be used if the material locally plastifies (small scale yielding). The fracture energy taking into account the surface energy and eventual dissipation to localized yielding at the crack tip is than called Γ_c.

Equation (1.35) establishes a relation between the stress intensity factors K_I, K_{II} and the energy release rate G. The corresponding critical values, i.e. the toughness KIc and fracture energy satisfy a similar relation. In pure mode I failure we have:

$$\Gamma_c = \frac{1-\nu^2}{E} K_{Ic}^2 \tag{1.36}$$

1.2.2 Interface fracture mechanics

1.2.2.1 Interface cracks and interface toughness

After presenting the basic quantities of linear elastic fracture mechanics of homogeneous solids, let discuss their application to on the interface between two dissimilar, isotropic, elastic solids (figure 20). These two solids have different Young's moduli (E_1, E_2) and Poisson's coefficients (ν_1, ν_2).

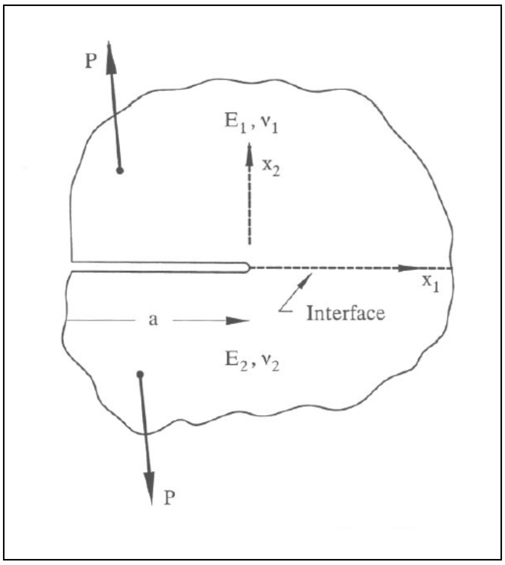

Figure 20: Interface crack [43]

Axis x_1 is placed parallel to the interface at the crack tip while the x_2 is perpendicular to the tip. Plane strain assumption is considered. Due to the dissimilarity in elastic properties of the materials 1 and 2, typically some asymmetry exists near the crack tip, even for symmetric geometry and loading. Universal crack tip field exist for the bimaterial interface crack with two stress intensity factors. However, stress fields in this case are more complicated than those for an homogeneous solid. Usually, interface cracks tend to be mixed mode.

The plane stain solution to the edge-crack problem [44] involves the two Dunders' elastic mismatch parameters:

$$\alpha = \frac{\bar{E}_1 - \bar{E}_2}{\bar{E}_1 + \bar{E}_2} \quad (1.37)$$

$$\beta = \frac{1}{2}\left[\frac{\mu_1(1-2\nu_2) - \mu_2(1-2\nu_1)}{\mu_1(1-\nu_2) + \mu_2(1-\nu_1)}\right] \quad (1.38)$$

where

$$\bar{E}_i = \frac{E_i}{1-\nu_i^2} \quad (1.39)$$

$$\mu_i = \frac{E_i}{2(1+\nu_i)} \quad (1.40)$$

represents the plane strain tensile modulus and the shear modulus respectively for i=1,2. Both parameters (α,β) vanish in the absence of any mismatch. In general, α is the most important of these parameters for interfacial fracture problems. When β is non-zero, the stress intensity factors have a complex values. The distinction between mode 1 and 2 does no longer operate. If the parameter β=0, the stresses intensity factors have real values. And similarly to the homogeneous solid, K_I controls the normal stress ahead of the tip and K_{II} controls the shear stress. In some cases, parameter β can be ignored without major error in stress calculation. More details will be given in a following section (1.2.3).

The definition of Dunders' parameters permits to define a relation between the energy release rate and the stress intensity factors for crack advance in the interface:

$$G = \frac{1-\beta^2}{2}\left(\frac{1-\nu_1^2}{E_1} + \frac{1-\nu_2^2}{E_2}\right)\left(K_I^2 + K_{II}^2\right) \quad (1.41)$$

This equation is a generalized form of Irwin's expression (eq.1.35). In this equation one can notice that the role of the second Dunders parameter is of minor importance given that β^2 is usually much smaller than 0.1, even for pretty dissimilar materials.

As mentioned previously, interfacial cracks are usually mixed mode. Thus, both intensity stress factors (K_I, K_{II}) are necessary to correctly characterize stresses on the interface. The mode mixity is generally measured by the angle ψ defined as follows:

$$\psi = \tan^{-1}\left(\frac{K_{II}}{K_I}\right) \quad (1.42)$$

which defines the mode mixity. When ψ=0, pure mode I exists, while when ψ=±90 pure mode II. Typically, the pair of energy release rate (G) and mode mixity (ψ) is used to fully characterize the intensity of an interface crack.

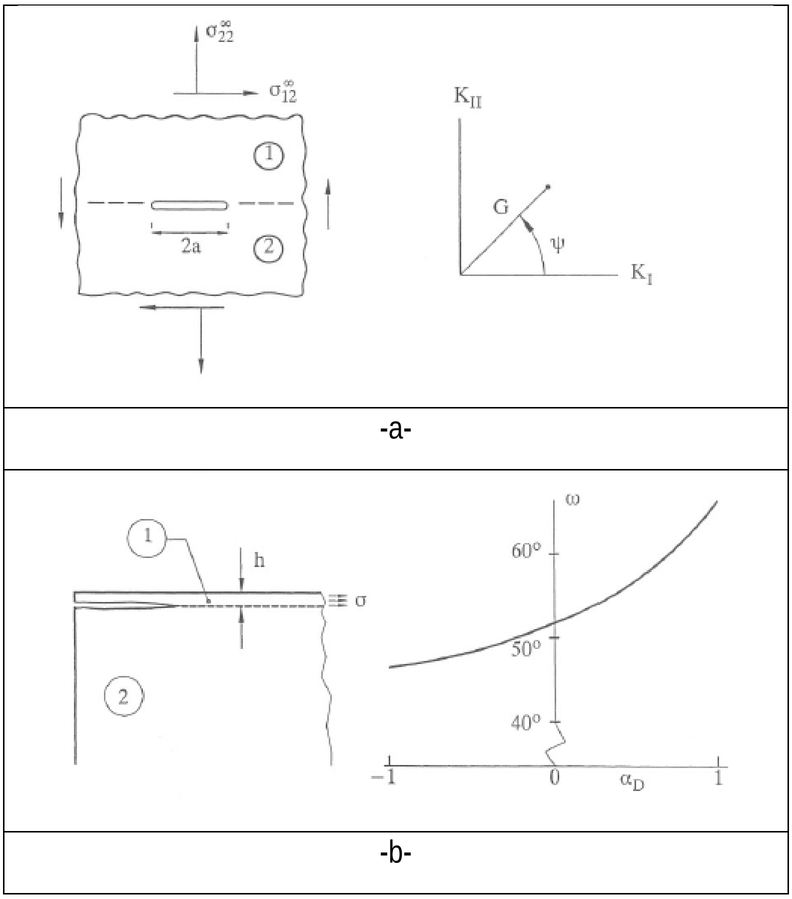

-a-

-b-

Figure 21: Remotely stressed interface crack (a) and interface crack between a thin film and a substrate [43]

Let us consider a crack of length 2a at the interface of an infinite bimaterial (figure 21a). For β=0, there is no influence of the elastic mismatch and, taking into account eq.1.30-1.32, the G,ψ pair reads:

$$G = \frac{1}{2}\left(\frac{1-\nu_1^2}{E_1} + \frac{1-\nu_2^2}{E_2}\right)\pi a\left({\sigma_{22}^{\infty}}^2 + {\sigma_{12}^{\infty}}^2\right) \tag{1.43}$$

$$\psi = \tan^{-1}\left(\frac{\sigma_{12}^{\infty}}{\sigma_{22}^{\infty}}\right) \tag{1.44}$$

In the case of a crack on the interface between a thin film subject to uniform residual tension and the substrate, the G,ψ pair is defined as:

$$G = \frac{1}{2}\frac{\left(1-\nu_1^2\right)\sigma^2 h}{E_1} \tag{1.45}$$

$$\psi = \omega(\alpha) \tag{1.46}$$

Note, the mode mixity (ψ) is a function of the first Dunders parameter. Moreover, the energy release rate depends on the film characteristics and the residual stress.

Interface toughness is defined as the critical value of G needed to advance the crack with the assumption that it propagates at the interface and is denoted as previously mentioned Γ_c. It has been found that interface toughness strongly depends on the mode mixity [42]. Consequently, it can be written as $\Gamma_c(\psi)$.

1.2.2.2 Conditions for crack kinking or deflection at an interface

In order to study if crack propagation in a loaded interface will continue at the interface or it will kink out of it and propagate into either of the adjoining materials, the energy release rates as well as the relative toughness of the interface and the adjoining materials should be compared.

Crack kinking out of an interface

Let us consider an initially interface kink crack loaded to a pair G,ψ having a length a (figure 22). The intensity of the kink crack tip can be denoted as G_{tip}, ψ_{tip}. A zero second Dunders parameter is supposed.

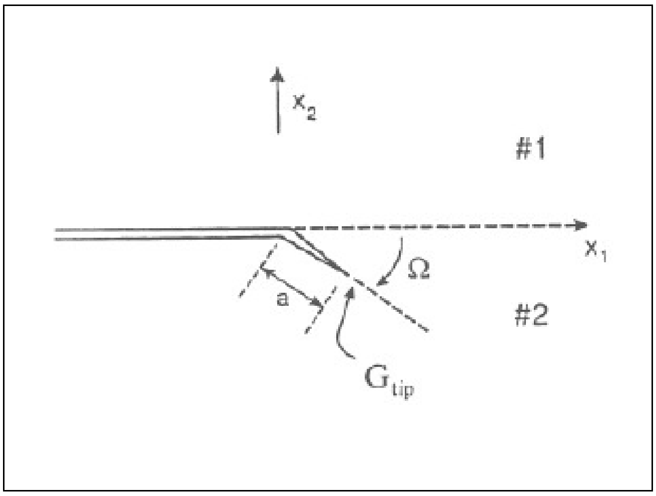

Figure 22: Illustration of a crack kinking out of an interface [43]

If a is very small compared to the parent interface crack, one can define G_{tip},ψ_{tip} as a function of Ω, ψ and α:

$$\frac{G_{tip}}{G} = f_1(\Omega, \psi, \alpha) \tag{1.47}$$

$$\psi_{tip} = f_2(\Omega, \psi, \alpha) \tag{1.48}$$

Ω denotes the kink crack angle between the interface and the crack tip. The solution to the elasticity problem for the kink crack provides the functions f_1 and f_2. As presented by He and Hutchinson [43], to a pretty good approximation, the kink angle which maximizes the energy release rate of the kink crack corresponds to mode I.

Whether the crack kinks or advances along the interface depends on the relative toughnesses. Let us designate by $\Gamma_c^{(2)}$ the toughness of material 2 and by $\Gamma_c(\psi)$ the toughness of the interface. If:

$$\frac{G}{\left(G_{tip}\right)_{max}} < \frac{\Gamma_c(\psi)}{\Gamma_c^{(2)}} \tag{1.49}$$

the condition $G_{tip}(max)= \Gamma_c^2$ will be satisfied prior to the condition $G= \Gamma_c(\psi)$ and the crack will kink. On the contrary, if the inequality of eq.1.49 is switched, the crack will continue to propagate at the interface.

Crack deflection at an interface

Let's consider a parent crack perpendicular to the interface with its tip at the interface (figure 23). The conditions for penetrating into material 1 or deflecting into the interface will be established. The remote stress is supposed to be symmetric with respect to the parent crack.

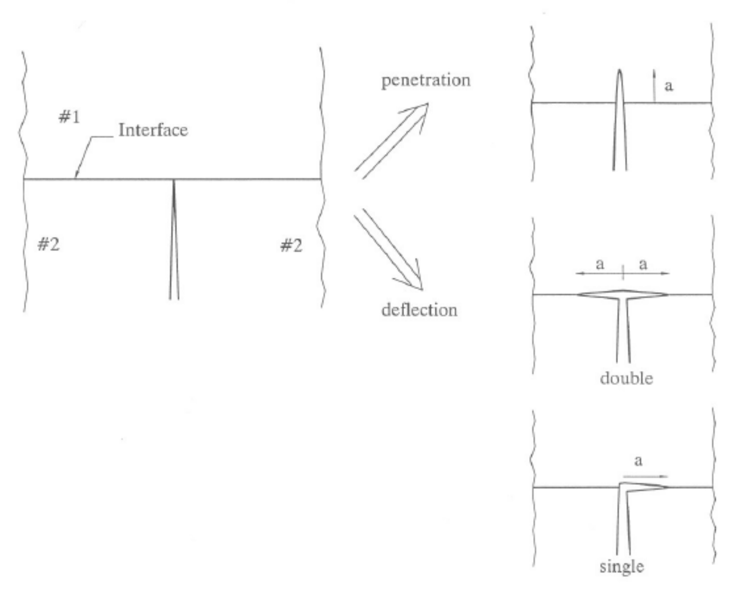

Figure 23: Arrested crack at the interface and possible crack propagation paths [43]

The energy release rate of the penetrating crack is denoted as $(G_{tip})_p$. This crack is a mode I crack. The energy release rate of the deflected interface crack is denoted as $(G_{tip})_d$ and mode mixity as ψ_{tip}.Dunders second parameter (β) is once again supposed zero. At equal crack lengths, the ratio of the competing crack propagation modes depends only on the first Dunders parameter (α) [42]. The competition between deflection and penetration is settled by the ratio of the interface toughness to that of material #1. In a similar way to this of the previous section, if:

$$\frac{\left(G_{tip}\right)_{deflection}}{\left(G_{tip}\right)_{penetration}} < \frac{\Gamma_c(\psi)}{\Gamma_c^{(1)}} \tag{1.50}$$

the conditions for penetration will be attained prior to those for deflection.

1.2.3 Buckling driven delamination under compressive residual stress

After recalling principal phenomena and quantities in linear elastic fracture mechanics (sec. 1.2.1) and interface mechanics (sec. 1.2.2), delamination at the interface between a thin elastic film bonded to a substrate will be discussed. The film is subject to equi-biaxial compression. The focus in this section is on the circular delamination features.

A thin film under compression will undergo buckling-driven delamination if an initially debonded patch of interface exists and the compressive stress is sufficiently high. Buckling induces a crack driving force which will cause the interface crack to advance if the interface toughness is sufficiently low. The equi-biaxial compressive stress state is produced in the unbuckled film during deposition as presented in section 1.1.4.

Buckling-driven delamination involves the nonlinear coupling of buckling and fracture and is usually observed in thin film/substrate systems. Mode mixity plays an important role on this phenomenon as interface toughness depends on the combination of mode I (tension) and mode II (shear) of fracture. Especially in the case of the circular delaminated features studied in this section, typically called "blisters", the ratio of mode II to mode I will determine the evolution of delamination.

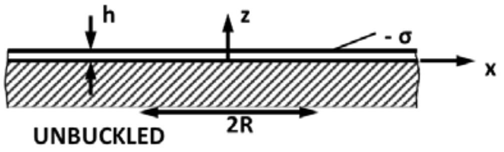 	
-a-	
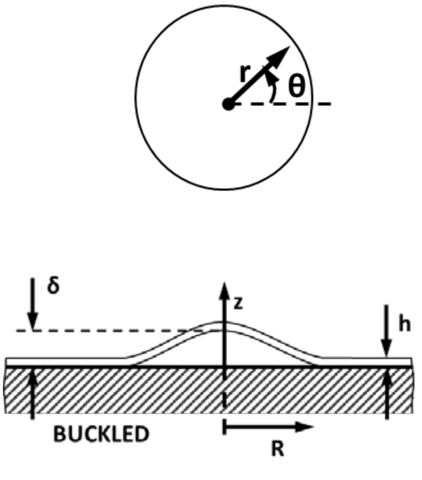 	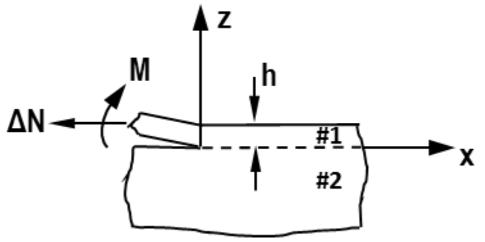
b-	-c-

Figure 24: Unbuckled thin film under compression (a), buckled circular blister (b) and forces and moments at the borders (c)

To analyze thin film blistering, an isotropic film is assumed, with Young's modulus E_1, Poisson's ratio v_1 and a thickness h. The substrate is supposed to be infinitely thick with Young's modulus E_2 and

Poisson's ratio ν_2. In the unbuckled state (figure 24a), uniform equi-biaxial compression σ in the film is considered.

A circular crack is supposed to exist at the film / substrate interface, such that the film is unbonded for r≤R. When the film is unbuckled, the deflection, denoted δ, at the center of the blister (r=0) is zero. As a consequence, the stress intensity factors and the energy release rate of the interface crack are zero too. On the contrary, when the film starts to buckle away from the substrate (figure 24b), the crack driving force is nonzero. In this case, the buckled film is modeled as a clamped circular plate according to von Karman nonlinear plate theory. Of course, the assumption R/h>>1 should be valid.

Thus, Hutchinson and al. [45] developed an equation linking the critical buckling stress to the blister's characteristics:

$$\sigma_c = 1.2235 \frac{E_1}{\left(1-\nu_1^2\right)} \left(\frac{h}{R}\right)^2 \tag{1.51}$$

For stresses larger than this critical stress σ_c, the film buckles away from the substrate forming a blister of height δ (maximal deflection of the circular plate).

$$\frac{\delta}{h} \cong \left[\frac{1}{c_1}\left(\frac{\sigma}{\sigma_c} - 1\right)\right]^{1/2} \tag{1.52}$$

$$c_1 = 0.2473\left(1+\nu_1\right) + 0.2231\left(1-\nu_1^2\right) \tag{1.53}$$

Equations (1.52)-(1.53) link the post-buckling stress in the film to its deflection. This model remains a good approximation of δ/h, even for high excess of stress (7% for σ/σc=10 and 25% for σ/σc=50) [45].

In order to determine the energy release rate and the stress intensity factors of the interface crack, the coupling of the buckled plate solution to the solution to the plane strain edge-crack problem (figure 24c) is necessary. After buckling of the film, the driving force for crack propagation is developed at the interface under the form of a moment M and a resultant stress change ΔN. Of course, in this analysis the two Dunders elastic mismatch parameters should be considered. However, due to the fact that the second parameter (β) complicates the solution and the assumption β=0 does not influence much the accuracy of the blister problem analysis, it will be neglected. For β=0, stresses ahead of the crack tip can be described as a function of the stress intensity factors as following:

$$\sigma_{zz} = \frac{K_1}{\sqrt{2\pi x}} \tag{1.54}$$

$$\sigma_{xz} = \frac{K_2}{\sqrt{2\pi x}} \tag{1.55}$$

The energy release rate, can also be related to the stress intensity factors as:

$$G = \frac{K_1^2 + K_2^2}{E_\bullet} \tag{1.56}$$

where

$$\frac{1}{E_{\bullet}}=\frac{1}{2}\left(\frac{1}{\overline{E}_1}+\frac{1}{\overline{E}_2}\right) \tag{1.57}$$

Finally, taking into account the developed moment M and force ΔN, the energy release rate reads:

$$G=\frac{6\left(1-\nu_1^2\right)}{E_1h^3}\left(M^2+\frac{1}{12}h^2\Delta N^2\right) \tag{1.58}$$

and the mode mixity will be:

$$\tan\psi\equiv\frac{K_{II}}{K_I}=\frac{\cos\omega+\left[h\Delta N/\left(\sqrt{12}M\right)\right]\sin\omega}{-\sin\omega+\left[h\Delta N/\left(\sqrt{12}M\right)\right]\cos\omega} \tag{1.59}$$

Thus, as presented in the section of interface mechanics (1.2.2), the fracture problem is fully characterized by the pair G,ψ.

The stored elastic energy in the unbuckled film can be calculated by:

$$G_0=\left(1-\nu_1\right)\frac{h\sigma^2}{E_1} \tag{1.60}$$

The ratio G/G_0 depends only on σ/σc and v_1 and is determined by:

$$\frac{G}{G_0}=c_2\left[1-\left(\frac{\sigma_c}{\sigma}\right)^2\right] \tag{1.61}$$

where

$$c_2=\left[1+0.9021\left(1-\nu_1\right)\right]^{-1} \tag{1.62}$$

From equation (1.51) the σ/σc ratio is expressed as:

$$\frac{\sigma}{\sigma_c}=0.8173\left(1-\nu_1^2\right)\frac{\sigma}{E_1}\left(\frac{R}{h}\right)^2 \tag{1.63}$$

showing that σ/σ_c can increase either due to an increase in blister radius R or to an increase in the buckled film stress, given that the other parameters in this equation are constant.

From the equation representing the mode mixity (1.59), one can notice that ψ depends only on the elastic mismatch (through ω(α)) and on the term hΔN/(√12M). This term can be determined as:

$$\frac{h\Delta N}{\sqrt{12}M}=0.2486\left(1+\nu_1\right)\frac{\delta}{h} \tag{1.64}$$

where δ/h can be found from equation (1.52). Thus, as σ/σ_c increases, $|\psi|$ increases too and the crack tip becomes more mode II compered to mode I.

Interface toughness mechanics presented in the previous section is still valid. The criterion for crack advance under combined mode I and II reads:

$$G = \Gamma(\psi) \tag{1.65}$$

Mode dependence of interface toughness is essential to the blistering failure. If a mode-independent was chosen such as:

$$G = \Gamma_{1c} \tag{1.66}$$

then because G increases with σ/σ_c , the blister would spread without limit when this criterion is attained. However, based on the observation of several stable morphologies, Hutchinson and al [45] proposed a mode mixity coupled to a mode-dependent interface toughness Γ(ψ) model.

Thus, toughness is represented by:

$$\Gamma(\psi) = \Gamma_{1c} f(\psi) \tag{1.67}$$

where Γ_{Ic} is the mode I toughness and

$$f(\psi) = 1 + \tan^2\left[(1-\lambda)\psi\right] \tag{1.68}$$

Consequently, there is a one-parameter family of toughness functions. For λ=1, it takes the form of (1.66) while for λ=0 it reduces to a criterion based on a critical value of K_I, independent of K_{II}.

Hutchinson and al [45] defined also a mode-adjusted crack driving force:

$$F = \frac{G}{f(\psi)} \tag{1.69}$$

such that the fracture criterion becomes:

$$F = \Gamma_{1c} \tag{1.70}$$

In order to better understand the blister spreading conditions, the fracture criterion (1.65) could be written:

$$\sigma\left[\frac{(1-\nu_1)h}{E_1\Gamma_{1c}}\right]^{1/2} = \left(\frac{G_0}{F}\right)^{1/2} \tag{1.71}$$

The right hand of this equation is a function of σ/σ_c

Thus, there would be no blister spreading regardless of the size of the initial debond if:

$$\sigma\left[\frac{(1-\nu_1)h}{E_1\Gamma_{1c}}\right]^{1/2} < y(\lambda) \tag{1.72}$$

where y(λ) is the minimum value necessary for blister propagation. This limit is important because it ensures that wide-spread delamination will not occur for the case of a circular blister.

However, this criterion underestimates the stress a film can tolerate when initial delamination is small. As small initial debond is defined one which satisfies R≤R* where:

$$R^* \cong 1.5h\left[\frac{E_1}{\left(1-\nu_1^2\right)\sigma}\right]^{1/2} = 1.5h\left[\frac{\left(1-\nu_1\right)E_1 h}{y^2\left(1-\nu_1^2\right)^2 \Gamma_{1c}}\right]^{1/4} \qquad (1.73)$$

In the following chapter, we will apply this theory to analyze the blistering of DLC coatings on M2-steel samples submitted to tribological loadings. DLC coatings of different thickness will be tested and the Young's modulus will be determined by micropillar compression. The residual stress prior to tribological loading will be determined by deflection measurements on coated Si-wafers. The post buckling stress s is an unknown. The deflection h and the radius of the blisters R will be determined by AFM measurements. These data allow a first estimation of the post buckling stress. The exact calculation of the stress induced by the tribological loading may be attempted by simulating the contact between the ring-shaped tool and the coating.

1.3 Basics of contact mechanics

1.3.1 Tangential loading and sliding contact

Hertz [in 46] was one of the first to analyze the stress field due to the contact of a plane surface and a cylindrical one (slider) as shown in figure 25. There is a relative velocity between these surfaces at their point of contact. Johnson assumes the point of initial contact as a fixed origin and considers the material of the lower surface flowing through the contact region from the left to the right with a steady velocity V. The x-axis is chosen to be parallel to the direction of sliding while the z-axis is vertical starting from the initial point of contact as illustrated in figure 25. The plane is defined as body 1 and the slider as body 2. A normal force P presses the two bodies together creating a contact length 2a. A tangential force of friction Q acts on each surface in a direction opposite to the motion. The bodies are considered to have a steady sliding motion so that the force Q represents the force of kinetic friction between the surfaces. Note, in the absence of friction force Q, the model reduces to classical Hertz theory of contact and contact stresses would not be affected by the sliding motion.

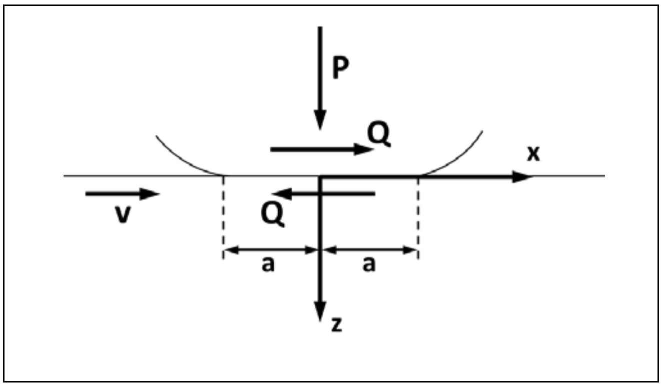

Figure 25: Schematic illustration of a sliding contact

In order to calculate the elastic stresses due to the tangential and normal tractions, the Hertz theory is applied. The two bodies can each be considered as an elastic half-space in the proximity of the contact region.

The contact area can be calculated by:

$$\alpha^2 = \frac{4PR^*}{\pi L E^*} \tag{1.74}$$

where P is the normal force, R^* the reduced radius (eq.1.75), E^* the reduced modulus (eq.1.76) and L is the length of the contact. The equation for R^* is valid for the contact of two cylindrical bodies. In current analysis the radius of the plane is taken as infinite thus the term concerning R_1 vanishes. E_i and v_i denote the Young's modulus and the Poisson's ratio of each body respectively.

$$R^* = \frac{1}{\frac{1}{R_1} + \frac{1}{R_2}} \tag{1.75}$$

$$E^* = \frac{1}{\frac{1-\nu_1^2}{E_1} + \frac{1-\nu_2^2}{E_2}} \tag{1.76}$$

Once the contact area determined, the relationship between the pressure and the tangential tractions in sliding contact should be defined. Typically, Amontons law [47] of sliding friction can be applied:

$$\frac{|q(x,y)|}{p(x,y)} = \frac{|Q|}{P} = \mu \tag{1.77}$$

This law defines the ratio between the forces presented previously as a constant coefficient of kinetic friction, widely known as the friction coefficient μ. This expression is found to be approximately valid when the sliding surfaces are separated by thin lubricating films.

The normal load P is shown to have a distribution of the form:

$$p(x) = \frac{2P}{\pi a^2}\sqrt{\left(a^2 - x^2\right)} \tag{1.78}$$

while the tangential friction Q:

$$q(x) = \pm\frac{2\mu P}{\pi a^2}\sqrt{\left(a^2 - x^2\right)} \tag{1.79}$$

where the negative sign is associated with a positive velocity V as shown is figure 23.

Both of these forces (P, Q) have a maximum value, denoted p_0 and q_0 respectively. These values are linked to each other simply by the friction coefficient:

$$q_0 = \mu p_0 \tag{1.80}$$

Moving towards stresses calculation during the contact of a plane and a cylindrical slider, let give the generic form of stress distribution equations shown in figure 26.

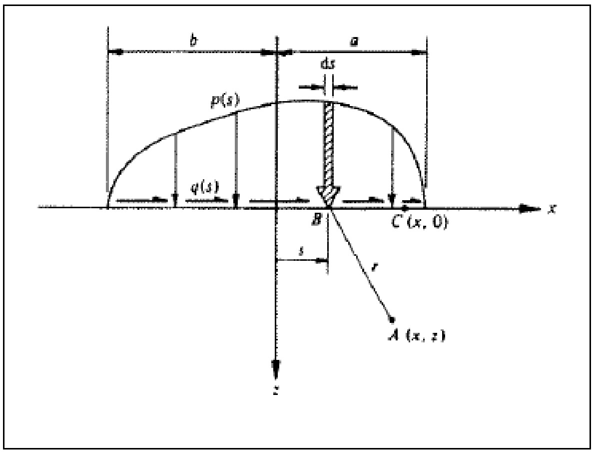

Figure 26: General scheme of force distribution is sliding contact [44]

In the general case, the contact area has a value of a+b and arbitrary distributions of p(x) and q(x) are considered. Axis x and z are identical to those of figure 24. The stresses due to the contact are given by the following equations:

$$\sigma_x = -\frac{2z}{\pi}\int_{-b}^{a}\frac{p(s)(x-s)^2}{\left\{(x-s)^2+z^2\right\}^2}ds - \frac{2}{\pi}\int_{-b}^{a}\frac{q(s)(x-s)^3}{\left\{(x-s)^2+z^2\right\}^2}ds \qquad (1.81)$$

$$\sigma_z = -\frac{2z^3}{\pi}\int_{-b}^{a}\frac{p(s)}{\left\{(x-s)^2+z^2\right\}^2}ds - \frac{2z^2}{\pi}\int_{-b}^{a}\frac{q(s)(x-s)}{\left\{(x-s)^2+z^2\right\}^2}ds \qquad (1.82)$$

$$\tau_{xz} = -\frac{2z^2}{\pi}\int_{-b}^{a}\frac{p(s)(x-s)}{\left\{(x-s)^2+z^2\right\}^2}ds - \frac{2z}{\pi}\int_{-b}^{a}\frac{q(s)(x-s)^2}{\left\{(x-s)^2+z^2\right\}^2}ds \qquad (1.83)$$

As illustrated by these equations, the stress can be separated in two parts, one due to the normal force and the other coming from the friction tractions. In elasticity, these stresses can be superposed and give the total stress.

Moving back to the sliding contact model analyzed previously, the two parts of stresses for calculating the stress component σ_x are given by:

$$(\sigma_x)_p = -\frac{p_0}{\alpha}\left\{m\left(1+\frac{z^2+n^2}{m^2+n^2}\right)-2z\right\} \qquad (1.84)$$

$$(\sigma_x)_q = \frac{q_0}{\alpha}\left\{n\left(2-\frac{z^2-m^2}{m^2+n^2}\right)-2x\right\} \qquad (1.85)$$

The stresses due to the normal load and the friction tractions are a function of the contact area (a), the maximum value of pressure or traction (p_0 or q_0), the x-z coordinates and the parameters m and n. These parameters can be calculated by:

$$m^2 = \frac{1}{2}\left[\left\{\left(a^2 - x^2 + z^2\right)^2 + 4x^2z^2\right\}^{1/2} + \left(a^2 - x^2 + z^2\right)\right] \tag{1.86}$$

$$n^2 = \frac{1}{2}\left[\left\{\left(a^2 - x^2 + z^2\right)^2 + 4x^2z^2\right\}^{1/2} - \left(a^2 - x^2 + z^2\right)\right] \tag{1.87}$$

and depend only on the size of the contact area (a) and the x-z coordinates. Note, in case of very small size of contact zone, these parameters can cause numerical precision problems and create calculation issues.

The normal force part $(\sigma_z)_p$ of the σ_z stress component is determined by the following equation:

$$\left(\sigma_z\right)_p = -\frac{p_0}{\alpha} m\left(1 - \frac{z^2 + n^2}{m^2 + n^2}\right) \tag{1.88}$$

However, calculation of the friction traction part needs the use of the normal part of the shear component τ_{xz}.

$$\frac{\left(\sigma_z\right)_q}{q_0} = \frac{\left(\tau_{xz}\right)_p}{p_0} \tag{1.89}$$

The latter can be obtained by a similar-form equation to $(\sigma_x)_p$ and $(\sigma_z)_p$:

$$\left(\tau_{xz}\right)_p = \frac{p_0}{\alpha} n\left(\frac{m^2 - z^2}{m^2 + n^2}\right) \tag{1.90}$$

Finally, the friction traction contribution to the shear stress field $(\tau_{xz})_q$ is determined by:.

$$\frac{\left(\tau_{xz}\right)_q}{q_0} = \frac{\left(\sigma_x\right)_p}{p_0} \tag{1.91}$$

By superposing the two parts of each stress component, one can calculate the total stress in the case of an elastic contact between a plane and a cylinder. Nevertheless, for problems including plasticity of the bodies in contact or thin films under residual stress, more complicated models are necessary and the application of finite element simulations should be considered.

We would like to emphasize here that, the present elastic analysis is of course useful to obtain the overall picture of the stress field. Unfortunately, in the following chapters, it will become more and more obvious that the very local stress, strain field beneath the contact area controls to a large extend blister nucleation. Local yielding has to be analyzed by finite element simulations. The difficulty of these simulations is discussed in the last part of this section.

References

[1] J.Robertson, Diamond-like amorphous carbon, Materials science and engineering R 37 (2002), 129-281.

[2] C. Donnet, A. Erdemir, Tribology of diamond-like carbon films: fundamentals and applications, Springer Science & Business Media, 2007.

[3] Schmellenmeier H, 1953, Experimentelle Technik der Physik 1, 49.

[4] S. Eisenberg, R. Chabot, 1971, J. Appl. Phys. 42, 2953.

[5] L. Holland, S.M. Ojha, 1976, Thin Solid Films 38, L17.

[6] E G Spencer, P.H. Schmidt, D.C. Joy, F.J. Sansalone, 1976, Appl. Phys. Lett. 29, 118.

[7] E. Staryga, G.W. Bak, Relation between physical structure and electrical properties of diamond-like carbon thin films, Diamond & Related Materials 14 (2005), 23–34.

[8] J.E. Field, Properties of Diamond, Academic Press, London, 1993.

[9] B.T. Kelly, Physics of Graphite, Applied Science Publishers, London, 1981.

[10] J. Roberston, Adv. Phys. 35 (1986) 317.

[11] G. M. Pharr, D.L. Callahan, S.D. McAdams, T.Y. Tsui, S. Anders, A. Anders, J.W. Ager, I.G. Brown, C.S. Bhatia, S.R.P. Silva, J. Robertson, Appl. Phys. Lett. 68 (1996) 779.

[12] P.J. Fallon, V.S. Veerasamy, C.A. Davies, J. Robertson, G.A.J. Amaratunga, W.I. Milne, J. Koskinen, Phys. Rev. B 48 (1993) , 4777.

[13] D.R. McKenzie, Rep. Prog. Phys. 59 (1996) 1611.

[14] P. Koidi, C. Wagner, B. Dischler, J. Wagner, M. Ramsteiner, Mater. Sci. Forum 52 (1990) 41.

[15] M. Weiler, S. Sattel, K. Jung, H. Ehrhardt, V.S. Veerasamy, J. Robertson, Appl. Phys. Lett. 64 (1994) 2797.

[16] C. P. O. Treutler, Surf. Coat. Technol. 200 (2005) 1969–1975.

[17] IREIS, R&D HEF Group

[18] M. Murakawa, T. Komori, S. Takeuchi, and K. Miyoshi. Surf. Coat. Technol., 120–121: (1999) 646–652.

[19] O. Hurasky-Schönwerth and M. Weck. PVD-coatings and synthetic ester in the tribological system of gear contact (in German), Tagungsband 41, Arbeitstagung: Zahnrad und Getriebeuntersuchungen, WZL, RWTH Aachen 2000.

[20] R. Lappalainen and S. S. Santavirta, Clin. Orthopaedics Relat. Res. 430, 72–79 (2005).

[21] S. Aisenberg, R. Chabot, J. Appl. Phys. 42 (1971) 2953.

[22] E.G. Spencer, P.H. Schmidt, D.C. Joy, F.J. Sansalone, Appl. Phys. Lett. 29 (1976) 118.

[23] T. Mori, Y. Namba, J. Vac. Sci. Technol. A 1 (1983) 23.

[24] N. Savvides, J. Appl. Phys. 59 (1989) 4133.

[25] M. Rubin, C.B. Hopper, N.H. Cho, B. Bhushan, J. Mater. Res. 5 (1990) 2538.

[26] B.F. Coll, M. Chhowalla, Surf. Coatings Techol. 68 (1994) 131.

[27] A.A. Voevodin, M.S. Donley, Surf. Coatings Technol. 82 (1996) 199.

[28] F. Davanloo, E.M. Juengerman, D.R. Jander, T.J. Lee, C.B. Collins, J. Appl. Phys. 67 (1990) 2081.

[29] V.I. Merkulov, D.H. Lowndes, G.E. Jellison, A.A. Puretzky, D.B. Geohegan, Appl. Phys. Lett. 73 (1998) 2591.

[30] Y. Catherine, Diamond and diamond-like carbon thin films, NATO ASI 266 (1991) 193.

[31] M.A. Lieberman, A.J. Lichtenberg, Principles of Plasma Discharges and Materials Processing, Wiley, New York, 1994.

[32] J.W. Hutchinson, Stresses and failure modes in thin films and multilayers, 1996.

[33] G. Stoney, The tension of metallic films deposited by electrolysis, vol. 82, 1909

[34] S.J. Bull, E.G. Berasetegui, An overview of the potential of quantitative coating adhesion measurement by scratch testing, Tribology International 39 (2006) 99–114

[35] P.J. Burnett, D.D.S. Rickerby, The scratch adhesion test: an elastic-plastic indentation analysis, Thin Solid Films 157 (1988) 233–254.

[36] M.T. Laugier, Metallurgical and protective coatings: an energy approach of the adhesion of coatings using the scratch test, Thin Solid Films 117 (1984) (1984) 243–249.

[37] J.L. Bucaille, E. Felder, G. Hochstetter, Mechanical analysis of the scratch test on elastic and perfectly plastic materials with the three-dimensional finite element modeling, Wear 249 (2001) 422–432.

[38] P.A. Steinman, Y. Tardy, H.E. Hintermann, Adhesion testing by the scratch test method: influence of intrinsic and extrinsic parameters on the critical load, Thin Solid Films 154 (1987) 333–349.

[39] S.J. Bull, Failure mode maps in the thin film scratch adhesion test, Tribol. Int. 30 (7) (1997) 491–498.

[40] M.D. Drory, J.W. Hutchinson, Measurement of the adhesion of a brittle film on a ductile substrate by indentation, Proc. R. Soc. Lond. A (1996) 2319–2341.

[41] H.Klöcker, Mécanismes physiques de la rupture.

[42] Tada, H., Paris, Pc. and Irwin, G. (1985) Stress Analysis of Cracks Handbook, Del Research.

[43] He, M.Y., Evans, A.G. and Hutchinson, J.W (1994) "Crack deflection at an interface between dissimilar elastic materials: role of residual stresses", Int. J. Solids Structures 31,3443-3455.

[44] Z. Suo, J.W. Hutchinson, Int. J. Fract. 43, 1 (1990).

[45] Hutchinson, J.W, Thouless, M.D. and Liniger, E.G. (1992) "Growth and configurational stability of circular, buckling- driven film delaminations", Acta Metal!. Mater. 40, 295-308.

[46] K.L. Johnson, Contact mechanics, Cambridge University Press, 1985.

[47] D. Dowson, *History of Tribology*, 2nd edition. (Wiley, New York, 1998), pp 768.

Chapter 2 Experimental methods

2.1 Introduction

In the last 20-30 years Diamond-Like-Carbon coatings increasingly found application in many industrial components. Several deposition processes are proposed depending on the desired DLC structure and properties. At the beginning of this chapter a presentation of a commonly used process, the Plasma Enhanced Chemical Vapor Deposition, will be given. Typical qualitatively and semi-qualitatively techniques exist for testing the adhesion of such thin hard coatings. However, methods like the Rockwell indentation or the Scratch test cannot give quantitative measurable results, like the adhesion energy, as many engineers desire. But, lacking a more efficient experiment they are still used to estimate the adhesion of thin films.

Besides the adhesion between the substrate and the coating, residual stresses, due to the deposition process, can play an important role on the materials behavior. Thus, they should be quantified. The most known and used method is the one proposed by Stoney based on the measurement of the film curvature prior and after deposition. Among other more advanced techniques, the deflection of FIB-milled micro-beams presents interesting potentials.

Of course, the mechanical properties of each substrate/coating system component, is useful to be determined either by costless, easily performed experiments or by more developed and innovative techniques. Nevertheless, the mechanical response of a multilayer material can largely differ from the behavior of its components independently. Furthermore, classical tests are not sufficient to delaminate thin hard adhesive coatings. For that reason, this type of materials should be tested under more severe and complex loading conditions.

Due to the increased complexity of the failure mechanism, more advanced and cutting-edge analysis techniques should be implemented. Moreover, sometimes a combination of experimental equipment such as the AFM, the FIB or even EDX analysis, operating at the microscopic scale, may be necessary in order to observe carefully and characterize damage.

2.2 Material and standard characterization techniques

2.2.1 The M2-steel substrate

Coatings were deposited on M2 high-speed steel cylindrical substrates (Table 1). The M2- steel coupons were tempered followed by a triple quench at 560°C to obtain a Rockwell hardness of 64. The coupons were processed by lapping. A first run, using a rough abrasive, allows achieving flat surfaces and parallelism between opposite faces of the disc. A second lapping phase, with finer abrasive, leads to a mirror polished surface with a roughness Ra below 0.02 µm. Prior to film deposition the mirror polished M2-steel samples were degreased with ethyl acetate and rinsed with ethanol.

C	Mn	Si	Cr	W	Mo	V
0.85	0.28	0.30	4.15	6.15	5.00	1.85

Table 1: Chemical composition of high speed M2 steel.

2.2.2 PECVD thin film deposition

2.2.2.1 The PECVD process

Plasma-Enhanced Chemical Vapor Deposition (PECVD) is typically used to deposit thin films from a gas state to a solid one on a substrate. The reaction gases form a highly reactive plasma. The latter is generated by a radio frequency (RF) (alternating current AC) or direct current (DC) discharge between two electrodes, the space between which is filled with the reacting gases. More details about this process are given in section 1.1.3 of Chapter 1.

2.2.2.2 DLC coatings and interlayer deposition

All coating layers were produced by a hybrid PVD/PECVD technology based on a glow discharge process. The M2-steel samples were placed on a planetary substrate holder in the vacuum deposition machine as illustrated in figure 1. Thus, a homogeneous coating thickness is achieved.

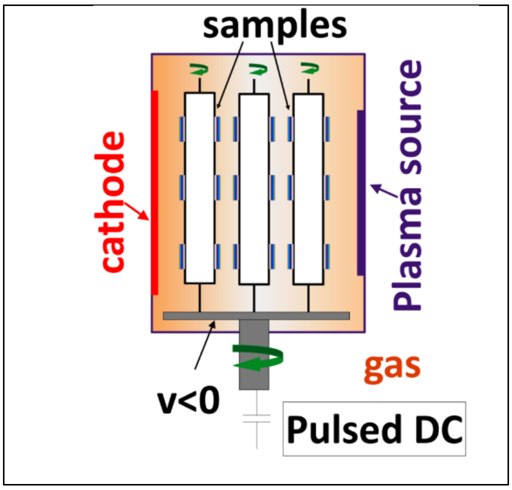

Figure 1: Schematic illustration of the deposition equipment

The cathode, on one side, is used to deposit the metallic interlayer whereas the plasma source (on the opposite location) allows Diamond-Like-Carbon deposition. The air in the chamber was evacuated to 10^{-6} mbar while heating to 150°C for surface degassing. The samples were etched for 1h in a low pressure argon plasma, applying a bias voltage of 150 V.

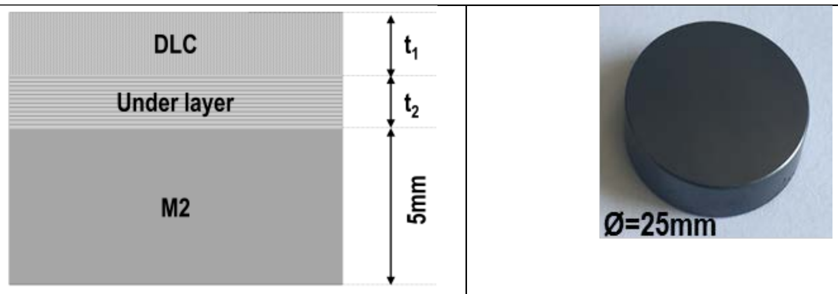

- a - *- b -*

Figure 2: Specimen for tribological test: (a) schematic representation, (b) optical view of a typical sample

First, a tungsten-based interlayer then several DLC coatings with thicknesses (t_1) were deposited (Figure 2). Biasing of the parts during growth was adjusted to obtain an a-C:H layer with 20 at.% of hydrogen [1]. The resulting sp^3 level should be around 20-30%.

2.2.3 Coating's thickness measurement

Once the multilayered film deposited, the substrate its thickness was quantified by a spherical or micro-abrasion wear test (Calotest). The Calotest is used for measuring the thickness of a wide variety of coatings (PVD, CVD, electrochemically applied etc.) from 0.2 to 30 µm.

The Calotest produces a three-body wear system. A steel ball rolls on the surface of the sample and a slurry consisting of water and fine abrasive particles drips continuously onto the ball at the contact region. A spherical indentation is created. The dimensions of the latter are determined and used to calculate coating thickness as illustrated in figure 3. The slurry wears the substrate in a controlled manner and thus assures highly reproducible results [5].

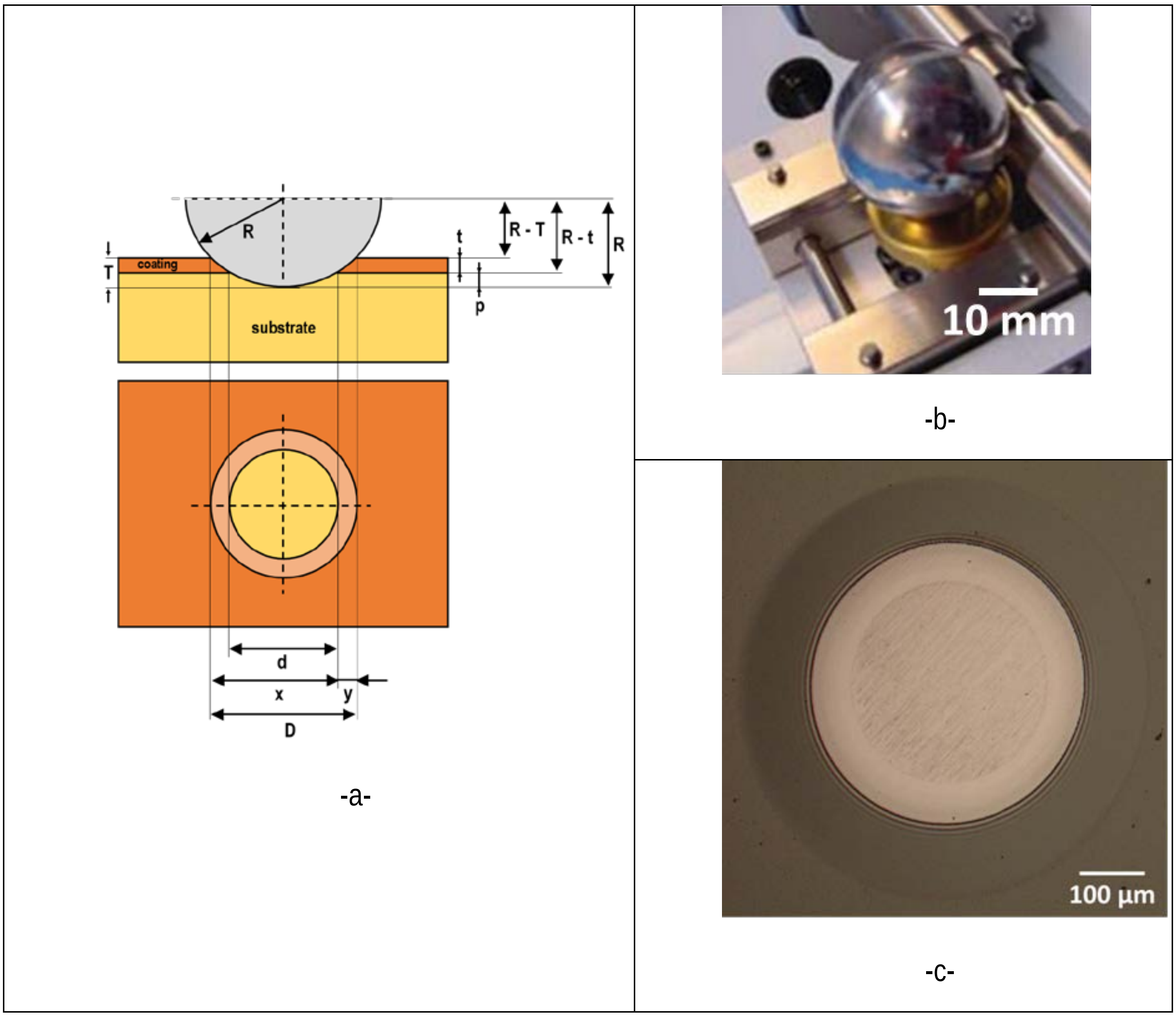

-a-

-b-

-c-

Figure 3: Principle of calotest measurement (a), experimental equipment (b) and an optical view of an imprint for a DLC coating of 2 µm and an interlayer of 0.8 µm (c) [6]

The calotest provides a quick and inexpensive determination of coating's thickness. The rotating sphere with a known diameter is pressed to the coating surface with a preselected load. Both the position of the sphere relative to the center of the sample and the contact load are constant. Optical inspection of the depression reveals the projected surfaces of the abraded coating and substrate sections.

If t is the thickness of the coating then:

$$t = T - p \tag{1}$$

where T and p represent respectively the total depth of penetration and the penetration depth in the substrate:

$$T = R - \left(\frac{1}{2} \sqrt{4R^2 - D^2} \right) \tag{2}$$

$$p = R - \left(\frac{1}{2}\sqrt{4R^2 - d^2} \right) \tag{3}$$

D denotes the imprint diameter in the coating, d the diameter of the imprint in the substrate and R the radius of the rotating sphere. The aim of the following analysis is to eliminate p. Actually, D, d and R are known or can easily be measured. On the contrary, the value of p is difficult measure.

Equation (1) may be written as follows:

$$t = \frac{1}{2}\left(\sqrt{4R^2 - d^2} - \sqrt{4R^2 - D^2} \right) \tag{4}$$

For thin films the penetration depth is small in comparison to the radius of the ball. Thus, the equation can be simplified to:

$$t = \frac{D^2 - d^2}{8R} \tag{5}$$

Or, by substituting D=x+y and d=x-y:

$$\text{thickness} = \frac{x \cdot y}{2R} \tag{6}$$

Where x and y represent respectively the diameter of the ball imprint on the substrate and the semi-difference of the ball imprint between the coating and the substrate.

2.2.4 Residual stresses quantification techniques

As already outlined in chapter 1, after deposition, the film may exhibit high residual stresses. These stresses can potentially cause debonding, local buckling and delamination of the coating. Hence, after coating deposition, residual stresses have to be measured. The oldest and most common way of determining residual stresses in coatings is Stoney's method [9]. An alternative method coupled to a finite element model can equally be applied. Both of them will be presented in this section.

2.2.4.1 Deflection based residual stress determination (Stoney formula) at the macroscopic scale

Residual stress in a film on a plate-like substrate causes the film-substrate compound to warp until mechanical equilibrium is reached, i.e. until both net force and bending moment are zero. A plate-like form of the substrate means that the substrate thickness, h_S, is constant and small in comparison to its in plane dimensions. From the curvature of the ***elastically*** deformed coated substrate the average film stress, σ^f, can be calculated. This method is very popular since the curvature of the bent substrate can easily be measured and no information on the elastic parameters of the film material is necessary. For this test, often silicon is used as substrate material since it is homogeneous with well-known mechanical properties [7].

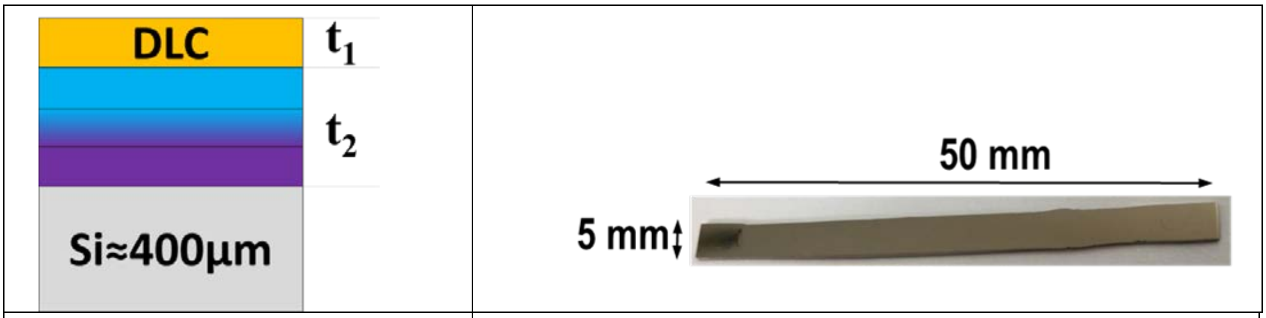

-a-

-b-

Figure 4: DLC coating on Si wafers

In present PhD, thin DLC coatings were deposited on silicon wafers (figure 4). Note, that the film thickness is identical to the one deposited on the M2-steel substrates. The DLC coating is submitted to compressive stresses while the substrate to tensile loads (figure 5a). After the mechanical equilibrium is reached, a slight bending of the wafer is observed.

Considering the wafer in figure 5, its radius of curvature R may be described by:

$$\frac{1}{R} = \frac{d\varphi}{ds} = \frac{\left(\arctan\left(w'\right)\right)' dx}{\sqrt{dx^2 + dw^2}} = \frac{w'' dx}{\left(1 + w'^2\right)^{(3/2)} dx} \cong w'' \tag{7}$$

where w represents the displacement in the z-direction, s and φ are the length and the angle of the arc, which follows the deformation curve of the plate. The latter approximation is valid for small deformations which is equivalent to small w'.

The change in curvature of the samples can be measured by profilometry (figure 6). A Mahr facility (PGK 120) was used for this measurement with a probe head MFW – 250. This probe can measure mechanically the surface roughness and is widely used in curved surfaces measurements.

Based on the previous analysis of plate deformation, Stoney developed an equation to quantify the residual stress in the film:

$$\sigma = \frac{E_S}{6} \frac{h_S^2}{h_f} \left(\frac{1}{R} - \frac{1}{R_0} \right) \tag{8}$$

E_S is the Young modulus of the substrate, h_S its thickness, h_f the film's thickness and R, Ro the curvatures after and prior to deposition.

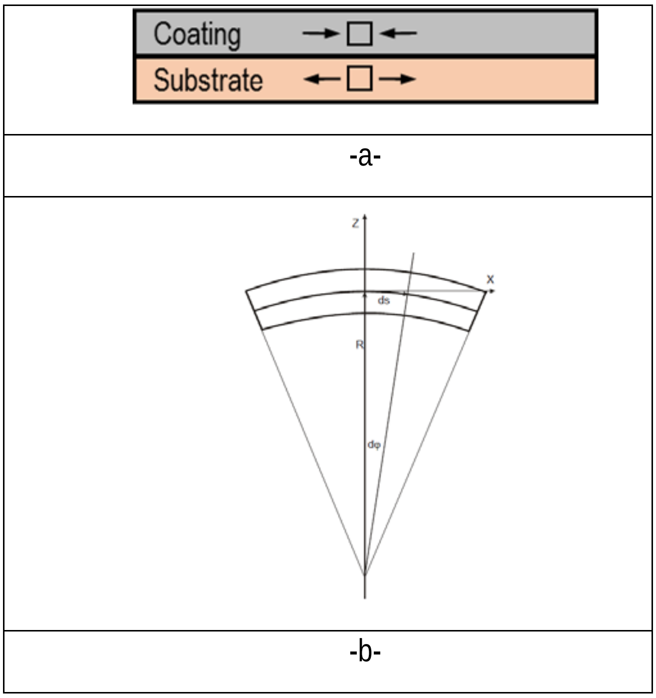

-a-

-b-

Figure 5: Effect of residual stresses in the flexion of a substrate coated with a thin film

Potential sources of errors should be discussed and analyzed. Let us calculate the total error in residual stress measurement.

$$\Delta\sigma = \pm\frac{\Delta E_s}{6}\frac{h_s^2}{h_f}\left(\frac{1}{R}-\frac{1}{R_0}\right)+\frac{E_s}{6}\frac{2h_s}{h_f}\left(\frac{1}{R}-\frac{1}{R_0}\right)(\pm\Delta h_s)$$

$$-\frac{E_s}{6}\frac{h_s^2}{h_f^2}\left(\frac{1}{R}-\frac{1}{R_0}\right)(\pm\Delta h_f)-\frac{E_s}{6}\frac{h_s^2}{h_f}\left(\frac{1}{R^2}\right)(\pm\Delta R)+\frac{E_s}{6}\frac{h_s^2}{h_f}\left(\frac{1}{R_0^2}\right)(\pm\Delta R_0) \qquad (9)$$

The relative error expression reads to:

$$\frac{\Delta\sigma}{\sigma}\leq\underbrace{\frac{\Delta E_s}{E_s}+2\frac{\Delta h_s}{h_s}}_{\text{small}}+\underbrace{\frac{\Delta h_f}{h_f}}_{\text{calotest precision}}+\underbrace{\frac{\Delta R}{R}\left|\left(1-\frac{R}{R_0}\right)\right|}_{\text{profilometry precision}}+\overbrace{\frac{\Delta R_0}{R_0}}^{\text{small}}\left|\left(\frac{R_0}{R}-1\right)\right| \qquad (10)$$

The substrate Young's modulus E_s is known with high accuracy. The substrate thickness h_s may be measured with high accuracy. The initial curvature of the uncoated Si-wafer is very small and reproducible. Hence, the last term of the equation 10 is negligible. On the contrary, film's thickness and change in curvature terms contributes mainly to the relative error estimation. They depend on the Calotest and profilometry precision respectively. Thus, the maximum total error in calculating the residual stress is found to be 14.5% for the thinnest coating (0.2µm of DLC + 0.8 µm of interlayer) and 7.2% for the thickest one (2.5µm of DLC + 0.8 µm of interlayer).

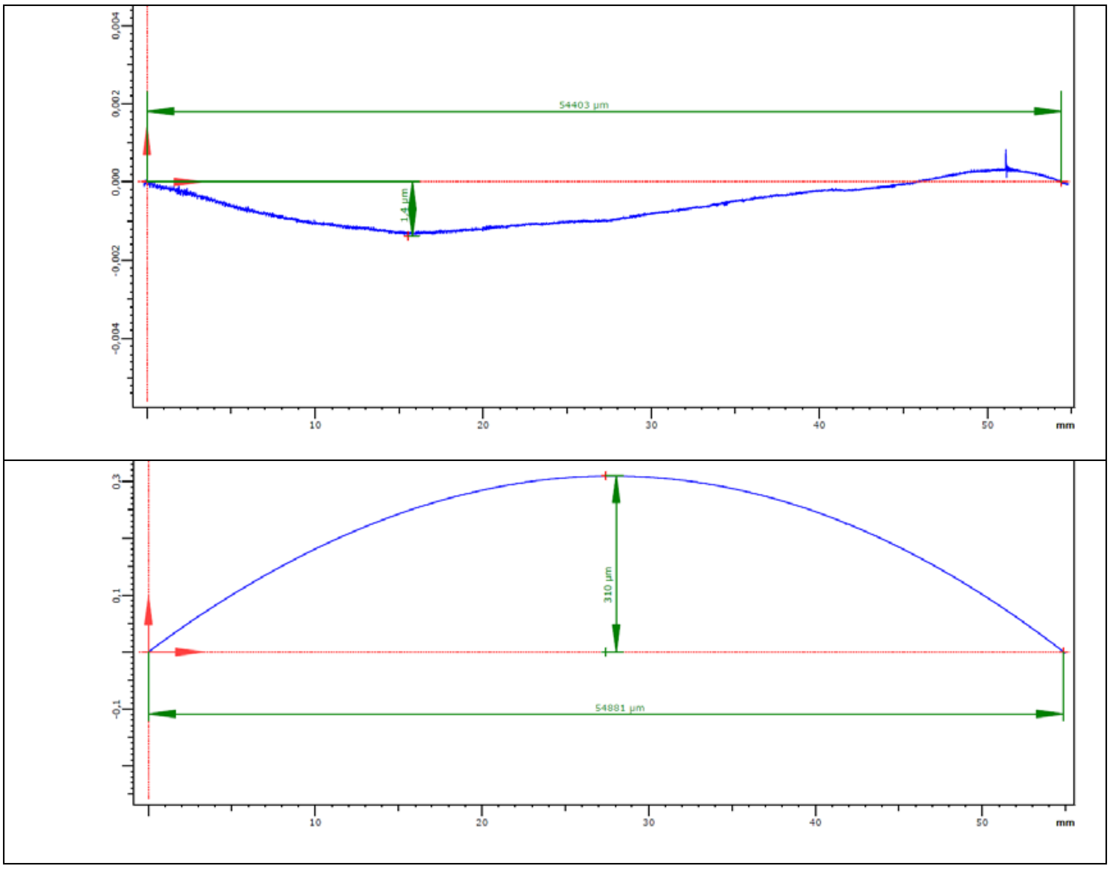

Figure 6: Example of curvature measurement prior and after deposition by profilometry

However, using Stoney's formula requires the respect of the following hypotheses [8]:

- The thickness of the substrate and the coating are smaller than the lateral dimensions
- Deformations and rotations are infinitesimal
- The thickness of the coating is smaller than the thickness of the substrate
- The substrate and the coating are homogeneous, isotropic and linear elastic
- The radius of curvature is equal in all directions (spherical deformation)
- The stress and the radius of curvature are constant on the whole surface of the plate.

Nevertheless, the Stoney formula is frequently used, even if these assumptions are not completely satisfied.

2.2.4.2 Stress measurement based on micro-beams deflection

Stress determination by the Stoney method on silicon wafers is widely applied, but the stress should be quantified on the M2-steel substrate samples too in order to validate the calculations and compare the role of the two different substrates.

In the last ten years, several new methods, based on FIB machining, were developed and especially well-adapted to residual stress thin film determination [9, 10, 11]. One of them, "ion beam layer removal method" [12], involves a micro-beam manufacturing by FIB milling and the analysis of micro-beam bending leads to the residual stress determination. A similar method was adapted here.

After SEM observations of the samples, micro-beams with built-in ends were manufactured (figure 7) using a Thermo Scientific™ Helios NanoLab™ DualBeam™ microscope, with Ga ions source at an acceleration voltage of 30 kV. In order to satisfyingly control the production of micro-beams by FIB-milling the ion current (I) and the incident angle (a) were fixed. The milling direction was optimized to reduce the effect of redeposition. Moreover, in order to improve the micro-beams shape and reduce the curtaining effect, a cross section cleaning (leading to enhanced homogeneity surface smoothness after FIB-milling) was applied. Parameters are summarized in table 3.

	a(°)	I(nA)
Regular cross section	52	9.3
cleaning cross section	53.5	2.5

Table 3: FIB operating conditions

The beam should not be wider than a few microns because imperfect parallel alignment of the ion beam and the film surface can lead to wedge-shaped interlayers and its thickness cannot be measured correctly.

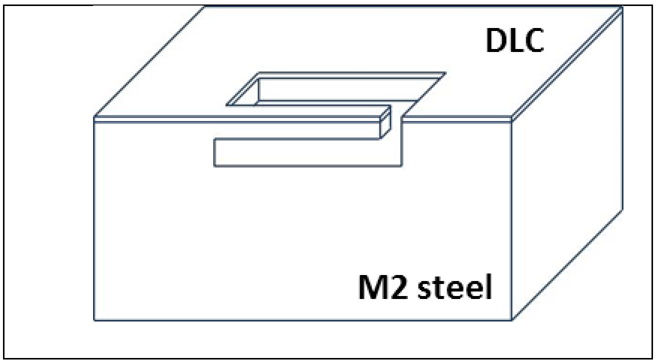

Figure 6: Schematic illustration of micro-beams prepared with a FIB facility

The experimental scheme was optimized in order to avoid micro-beam plastic deformation or failure during the FIB-milling for a beam length about 50 µm. A special sample holder allowed milling in two orthogonal directions (figure 7).

Figure 7: Sample holder used in FIB

After preparation of the built-in micro-beam, one end was cut and, the residual stress induced, deflection measured. To determine the stress in each layer (DLC and interlayer), deflection measurements for at least two different M2-steel thicknesses are required. The deflection of 5 different M2-steel thicknesses (1, 2, 3, 4, 5 µm) for t_1=2.5 µm and t_2=0.8 µm were analyzed.

The experimental stress data may be affected by several errors difficult to quantify. The most significant errors sources are discussed hereafter. FIB-milling can influence the film stress distribution. Implanted ions eventually affect the mechanical properties of the material as well as the residual stress field. By acting on the ion current and incident angle, the effect on the accuracy of the experimental measurements can be minimized. However, implantation depths about 10nm to 30nm were noticed. This corresponds at worst to cross sectional dimension changes smaller than 1%. In the literature [12, 13], grain boundary embrittlement and possible amorphization are also mentioned. Multiplying the number of micro-beams and independent measurements, allows an estimation of the error. The standard deviation of the experimental data is smaller than 8%.

2.3. Multilayer components properties identification

2.3.1 In-situ shear tests

This type of mechanical test is used to measure the strain to failure of the DLC coating. As will be shown in the following chapter, when submitted to tribological loading, the coating debonds, buckles and eventually cracks at the blister boundaries. The strain to failure of the DLC and all the coating components hence controls to a large extend the final film properties.

Shear samples were prepared exactly as the cylindrical samples of the previous sections. The same thicknesses of interlayer and DLC coating were deposited. The aim of this test is to determine the critical strain at coating failure. The strain in the red area (figure 8a) is homogeneous and corresponds to pure shearing.

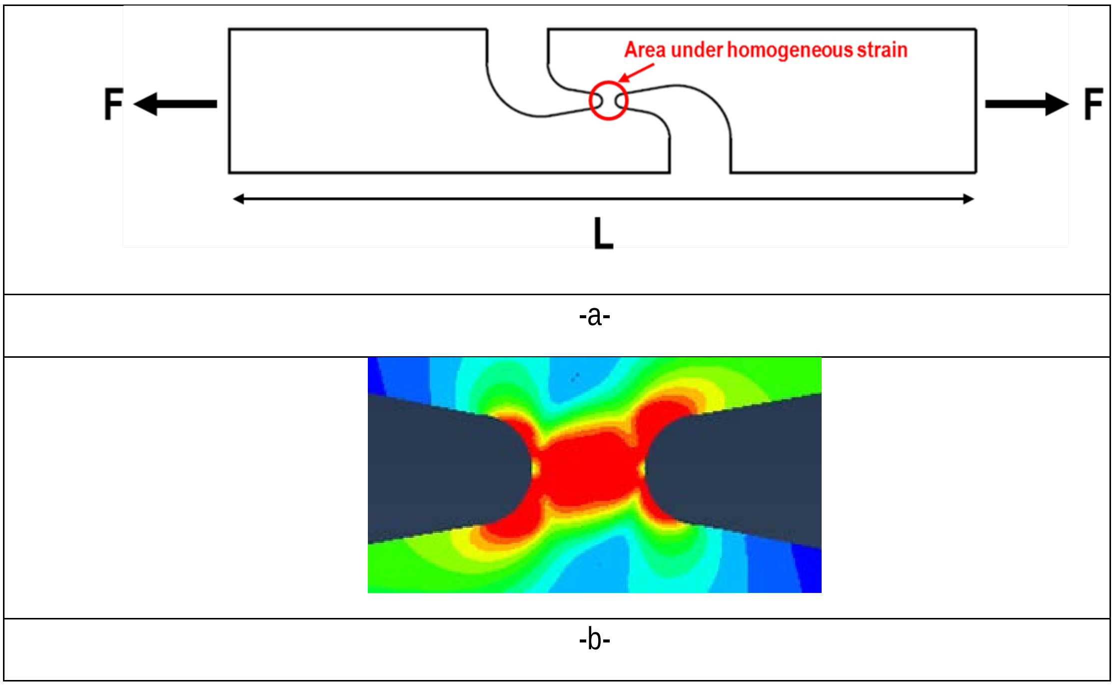

-a-

-b-

Figure 8: Homogeneous strain area during an in-situ shear test

$$\left.\begin{array}{l} \underline{\underline{\varepsilon}} = \begin{pmatrix} \varepsilon_{xx} & \varepsilon_{xy} \\ \varepsilon_{xy} & \varepsilon_{yy} \end{pmatrix} \approx \begin{pmatrix} 0 & \varepsilon_{xy} \\ \varepsilon_{xy} & 0 \end{pmatrix} = \underline{\underline{\varepsilon}}(F)(\text{Finite element}) \\ (F,\Delta L)_{\text{coating failure}} = \text{experimental} \end{array}\right\} \rightarrow \underline{\underline{\varepsilon}}_{\text{failure}} \qquad (11)$$

At failure, lines at 45° to the tensile direction appear. These lines are perpendicular to the principal stress and indicate coating failure. At this precise moment the strain in the coating corresponds to its failure strain. Thus, the load displacement curve (F, L) and the moment at which failure occurs (F_{failure}, L_{failure}) are recorded experimentally. The corresponding strain is determined by finite element simulation. The approach is summarized in equation 11.

$$\underline{\underline{\varepsilon}}' = \begin{pmatrix} \cos(45°) & -\sin(45°) \\ \sin(45°) & \cos(45°) \end{pmatrix} \begin{pmatrix} 0 & \varepsilon_{xy} \\ \varepsilon_{xy} & 0 \end{pmatrix} \begin{pmatrix} \cos(45°) & +\sin(45°) \\ -\sin(45°) & \cos(45°) \end{pmatrix} \qquad (12)$$

$$\underline{\underline{\varepsilon}}' = \begin{pmatrix} \varepsilon_{xy} & 0 \\ 0 & -\varepsilon_{xy} \end{pmatrix} \quad \varepsilon_{\text{coating failure}}^{\text{simple tension}} = \varepsilon_{xy}(F_{\text{failure}}) \qquad (13)$$

Failure at 45° is explained by equations (12) and (13). Loading the sample with simple tension, due to its specific geometry, and by changing the reference system, principal stresses are translated from the general reference system to a local one (figure 9). Thus, finally, a pure shear is observed in the central section of the specimen.

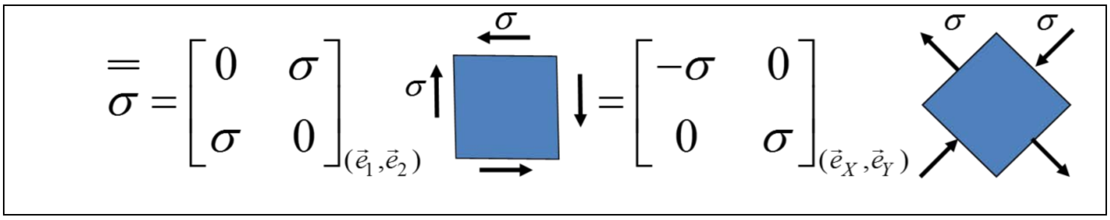

Figure 9: Reference change to obtain pure shearing [12]

The experimental procedure consists in a shear sample (figure 10) loading with a load F. The experiment is run on a Kamrath & Weiss tensile machine installed in the Zeiss SUPRA 55 SEM specimen chamber. The load is recorded on a load cell with maximum capacity of 10kN and accuracy of ±2N. The displacement is recorded on a LVDT sensor with an accuracy of ±1μm.

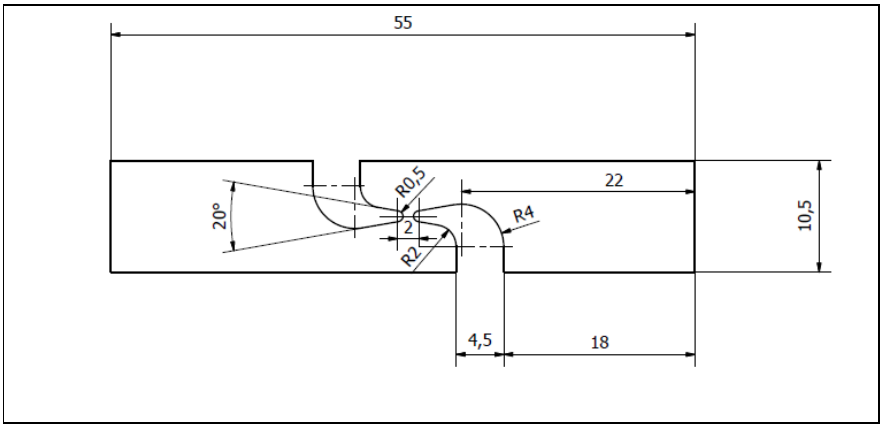

Figure 10: Shear sample geometry

Concerning the finite element simulation, it was done in two steps. Firstly, the simulated load displacement curve F (L) has to correspond to the experimental one. Secondly, the strain to failure is obtained by determining the stain at the experimental value of load at failure.

2.4. Severe tribological solicitation experimental setup ('ring-flat plane')

After standard coating characterization, the latter were submitted to severe tribological loading conditions generated by an experimental setup designed to perform accelerated wear (figure 11). The test facility consists in a rotating ring (diameter 35 mm, width 8 mm) brushing against the surface of the DLC coated sample. At the same time, an oscillating in-plane movement of the specimen takes place.

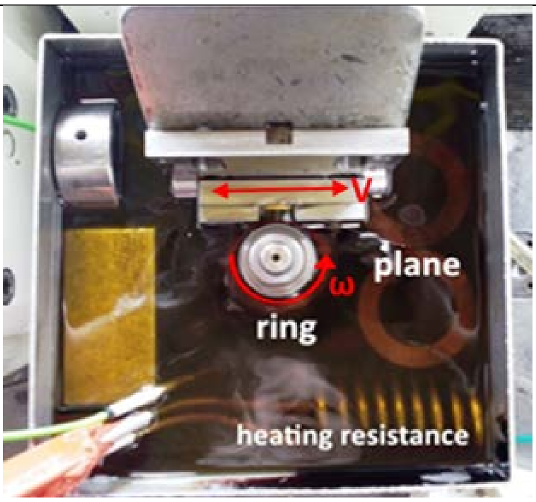

Figure 11: Severe tribological test facility for accelerated wear [6]

A normal load of 1kN is applied to the ring. The temperature of the oil bath is maintained constant (100°C) with a heating resistance. The experimental conditions are summarized in table 2. To measure the normal load, a load cell with a capacity of 8000N and an accuracy of ±10N is used. The tangential load is measured with a different sensor (with capacity of 1000N and precision of ±3N). The temperature sensor determines the oil temperature with an accuracy of ±1°C. The parameters of the tribological test are summarized in Table 2.

Rotational speed (rpm)	Speed (mm/s)	Load (N)	Stabilised friction coefficient	Temperature (°C)
1450 to 350	3	1000	±0.06 to ±0.03	100

Table 2: Tribological test parameters

Successive decreases in rotational speed take place. During the test, the friction coefficient (tangential/normal force) is measured. The test is stopped, when the friction coefficient increases rapidly revealing complete delamination of the DLC. The advantage of this facility is the increased delamination of the coating compared to scratch test or Rockwell indentation.

2.5. Failure and delamination advanced analysis techniques

The tribological experiment allows to achieve coating delamination. This failure has to be analyzed in order to understand the mechanism of cracking initiation and propagation. For this purpose, various experimental techniques and methods were implemented.

2.5.1 Optical and electron microscopy observations

The wear traces after the tribological experiment were initially observed with an optical Olympus microscope at low magnification. Further observation at the SEM was considered necessary due to the microscopic scale of the delaminated features of the DLC coating. A Zeiss SUPRA 55 Scanning Electron Microscope was used. Most observations were done with an accelerating voltage of 15kV and a working distance between 7 and 9 mm. Secondary Electron mode was chosen to analyze damage induced topography. Note, samples were tilted between 50 and 60 degrees to allow better observation of delaminated blisters. Observations at 0^0 cannot reveal the buckled features (figure 12).

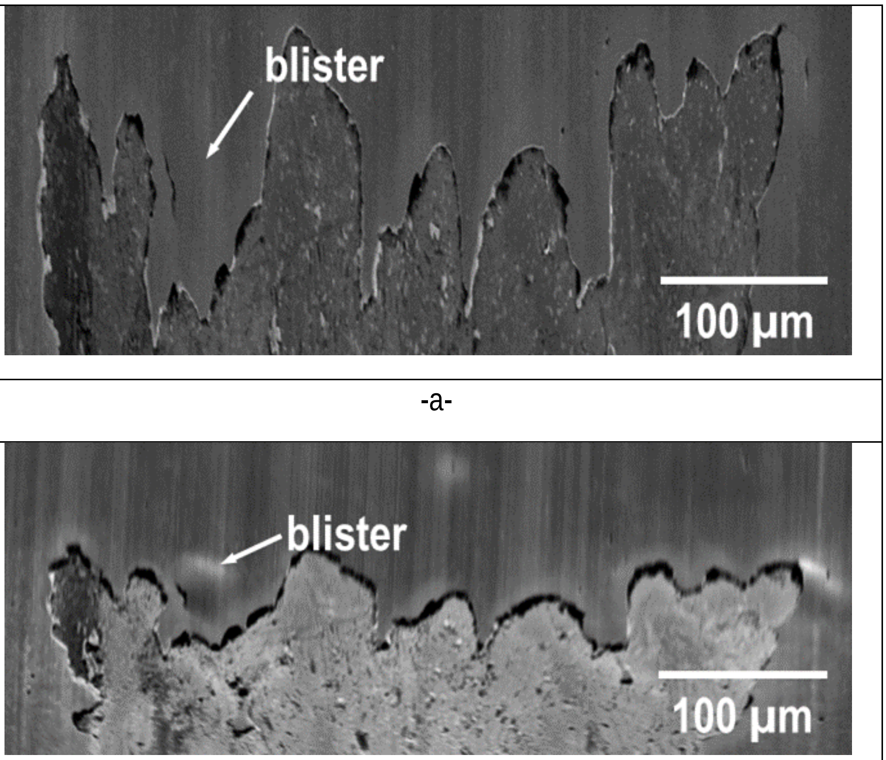

-a-

-b-

Figure 12: Blisters' observation at SEM of a 1.5 µm damaged DLC coating at 0^0 (a) and 60^0 (b)

2.5.2 Atomic Force Microscopy (AFM) measurements of local delaminated topology

<u>Operating principle of AFM</u>

The AFM consists of a cantilever with a sharp tip (probe) at its end that is used to scan the specimen surface. The cantilever is typically made of silicon with a tip exhibiting a radius of curvature of some nanometers. When the tip is brought into proximity of a sample surface, forces between the tip and the sample lead to a deflection of the cantilever according to Hooke's law. Depending on the situation, forces that are measured in AFM include mechanical contact force, van der Waals forces, capillary forces etc. Along with the force, additional quantities may simultaneously be measured through the use of specialized types of probes.

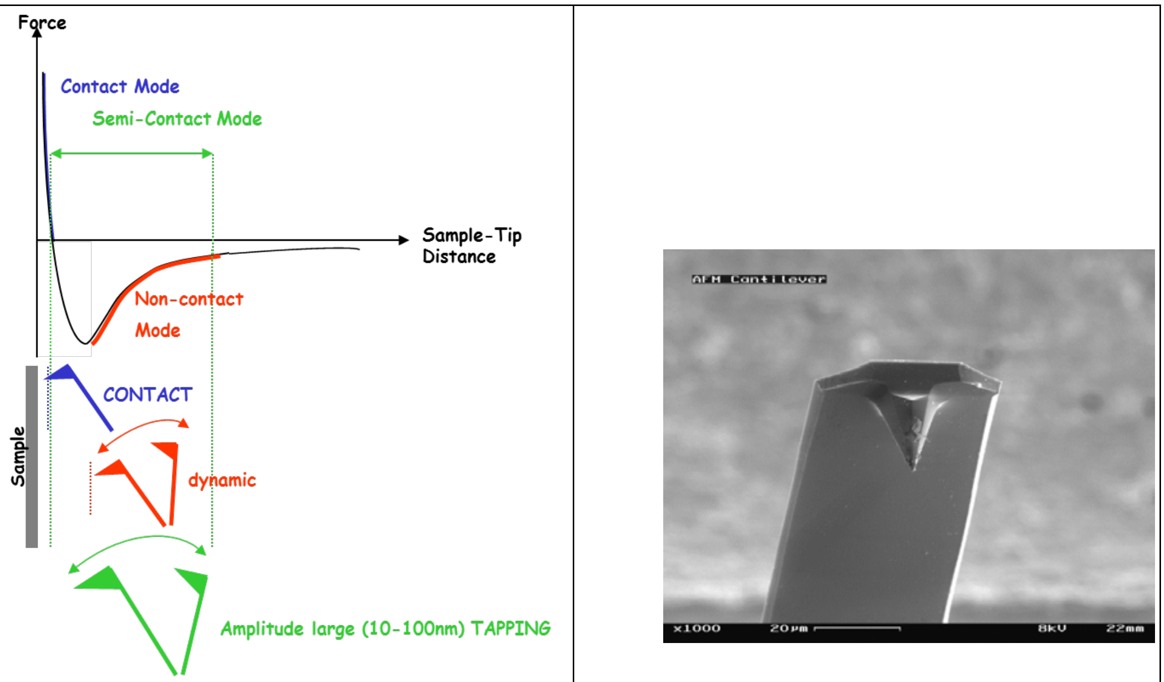

-a- -b-

Figure 13: Different operating modes of AFM (a) and view of an AFM cantilever (b) [16]

The different AFM operating modes are presented above (figure 13a) varying from contact and non-contact mode to the tapping one (or intermittent contact). A typical cantilever and its tip are shown in figure 13b. The cantilever scanning the sample surface is irradiated by a laser beam. The deflection of this beam is captured by a photo-diode and is translated to a topology.

AFM application to DLC coatings analysis

An Atomic Force Microscope (AFM) was used to measure the geometry of local delaminated features of the DLC coating (blisters). This technique was chosen due to the size of the blisters and the accuracy of the measurement. The values measured are the blisters radius (R) and their maximal deflection (δ) as denoted in Hutchinson's model [43] in chapter 1.

To measure the single blisters' geometry, intermittent contact mode was used. This mode is inspired from the non-contact one but permits a larger amplitude. This mode is very stable and provides good measurement resolution. An advantage of this mode is the decreased friction forces during measurement leading to less degradation of the measuring cantilever. A JPK Nanowizard III equipment was used for the measurements. The operating characteristics are summarized in table 4.

AFM	type	frequency	Spring constant
JPK	Nanowizard III	285 kHz	42 N/m

Table 4 : AFM measurement operating conditions

A NANOSENSORS cantilever type PPP-NCHR-SPL was used. The resonance frequency of the cantilever was 285 kHz and its spring constant was 42 N/m. Its geometrical characteristics are summarized in table 5.

Thickness	4±1 µm
Length	125±10 µm
Width	30±7.5 µm
Tip height	10-15 µm

Table 5:Cantilever characteristics

The lateral accuracy of this kind of cantilever is in the order of nanometers. In the case of the DLC blistering analysis, several measurements are needed for one blister due to limitations of the scanning surface (60µm x 60µm).

2.5.3 Focused Ion Beam (FIB) cross-sections of the multilayer

Operating principle of FIB

Focused ion beam (FIB) systems operate in a similar way to a scanning electron microscope (SEM) except, that FIB systems use a finely focused ion beam (usually gallium ions) that can be operated at low beam currents for imaging or at high beam currents for site specific sputtering or milling (figure 14).

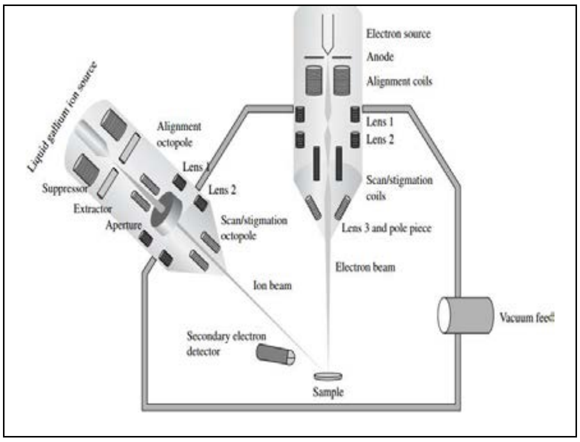

Figure 14: Principle of a Focused Ion Beam [13]

FIB application to DLC coatings analysis

In order to examine the substrate/coating interface, several cross-sections were made by FIB-milling. Thus, the observation of the film delamination can reveal information and localized the film debonding could be observed. Furthermore, these cross-sections reveal the different components of the coating system such as the M2-steel substrate and its microstructure, the interlayer and the DLC layer and opens a field of wide failure investigations.

The sample is placed into the chamber of the microscope and once vacuum is achieved (~10^{-5} mbar), the ion beam can operate and remove the desired volume of material. The experimental procedure consists of removing material layers by the Focused Ion Beam (FIB) Gallium jet. The operating conditions are given in table 6. It presents a lateral resolution of few nanometers. The FIB allows cutting µm-sized slices of almost every material while observing the sample by a Scanning Electron Microscope. Gallium ions hit the surface of the sample and remove a small volume of material. This process continues until the desired geometry is obtained.

FIB	Helios NanoLab	30kV	2.5nA to 80pA

Table 6: FIB milling conditions

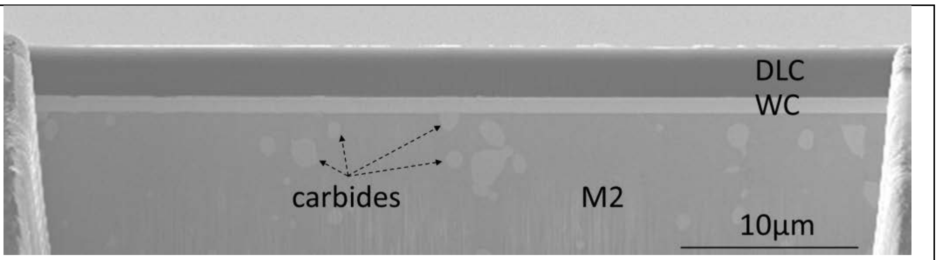

Figure 14: Typical SEM observation after FIB milling of a M2-steel sample with a 2.5µm DLC coating at 15kV and a working distance of 4 mm

In a second phase, after revealing the structure of the sample (figure 14), successive cross-sections (on previously selected single blisters) were performed (figure 15). An initial cross-section was milled next to the blister border (AB), followed by a series of parallel FIB cuts until the center of the blister (A'B'). Thus, a wider view of the failed area is achieved.

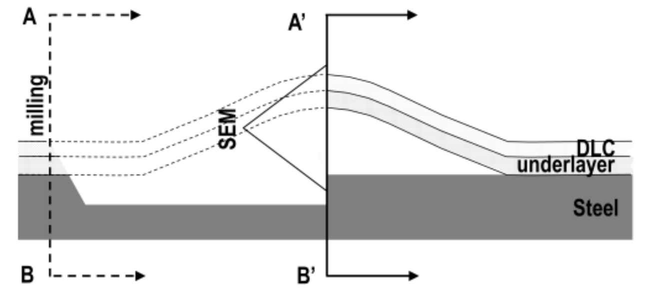

Figure 15: Schematic of FIB milling on a blister.

2.5.4 EDX analysis of the delaminated features

EDX principle

Energy Dispersive X-Ray spectroscopy (EDX) is applied for analyzing the chemistry of a material's surface. Figure 16 shows the different types of observations that can be made of a primary electron beam. X-Rays are typically obtained at a micrometric depth (~µm). Of course, the resulting analysis depth depends on the nature of the analyzed material and the energy of primary electrons.

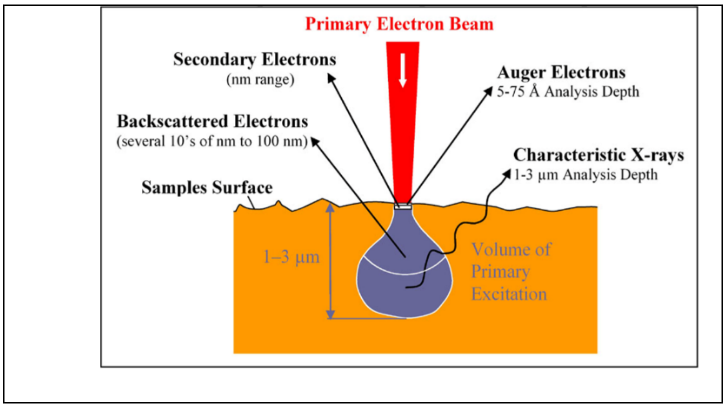

Figure 16: EDX-analysis: Interaction of the primary electron beam with a surface [17]

Application to DLC failure analysis

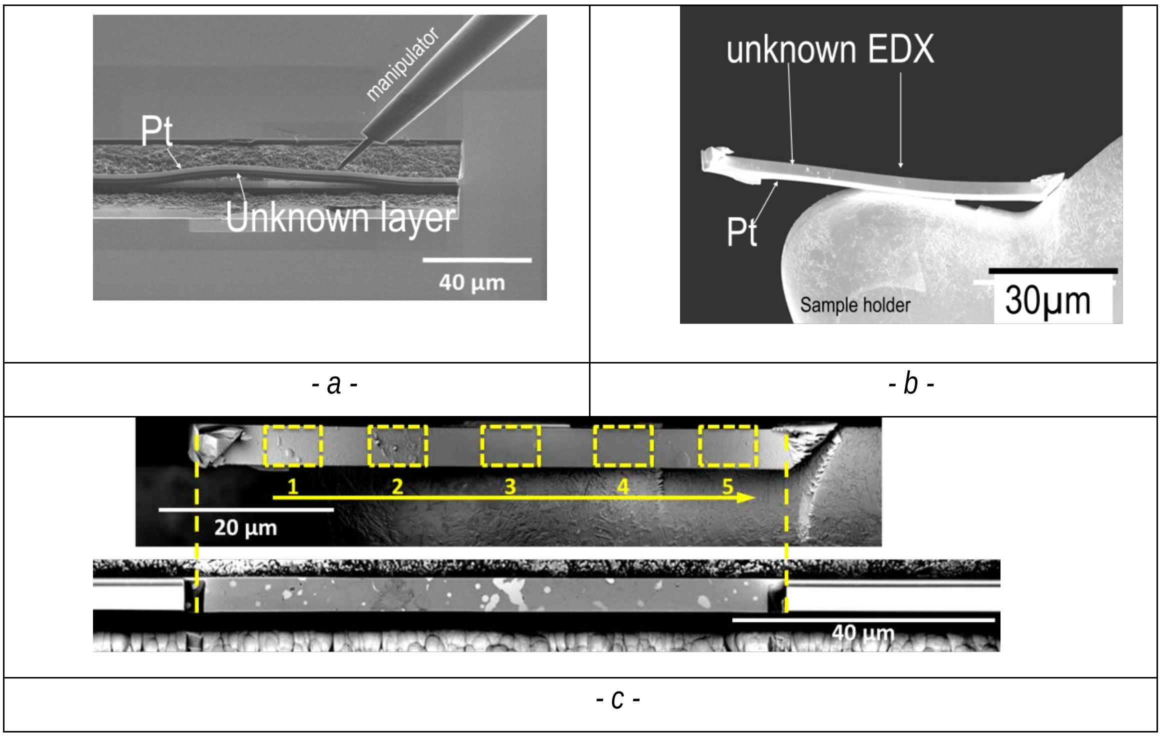

- a -

- b -

- c -

Figure 17: Turning a portion of the blister upside down with the micro manipulator (a,b). The five zones analyzed by EDX (c).

A micro manipulator (“Easy Lift”) of the FIB facility (figure 17) was used to remove a delaminated film. The film was lifted-out and turned upside down in successive steps. It was finally put on a special sample holder (TEM micro-grip) in order to analyze by EDX its internal fractured surface. A Brucker EDS detector was used at 5 keV for this purpose. The electron beam was perpendicular to the surface to be analyzed. Due to the film’s thickness and its positioning into the chamber of the microscope the resulting spectrum is considered as qualitatif.

2.6. Conclusions

In this chapter, the experimental techniques applied to analyze the DLC coating/M2 steel system were presented. The samples preparation was detailed as well as the deposition process. Moreover, the coating's thickness measurement technique and the quantification of residual stress in the film were explained. For that purpose, Stoney's formula was applied and complementary determination of residual stress was done by measuring the deflection of FIB-milled micro-beams.

The tribological experimental setup to test DLC coatings behavior was presented. Failure and delamination of the coatings was analyzed by coupling several ordinary and more advanced techniques. Optical and electron microscopy were used to observe the damaged surface of the samples. Further investigation was done by means of Atomic Force Microscopy due to the size of the delaminated features. A Focused Ion Beam facility was implemented to examine the interface between the coating and the substrate after tribological loading. Finally, EDX analysis took place after FIB-milling in order to investigate the fractured surface of the substrate.

References

[1] C. Ould, C. Héau, J. Fontaine, C. Donnet, Influence of hydrogen content on DLC tribological behavior: tests in mineral base oils, Proceedings of the World Tribology Congress (8-13 sept. 2013, Torino, Italy), Politecnico di Torino (editor), pp.640-643.

[2] Surface Engineering Institute, RWTH Aachen

[3] J. Tunis, X. Wang, X. Li, Experimental and numerical investigation into the adhesion of PVD coatings on minting dies, 13th international conference of fracture (16-21 June 2013,Beijing, China)

[4] S.J.Bull, E.G.Berasetegui, An overview of the potential of quantitative coating adhesion measurement by scratch testing, Tribology International, Volume 39, Issue 2, February 2006, Pages 99-114

[5] K.L.Rutherford, I.M.Hutchings, A micro-abrasive wear test, with particular application to coated systems, Surface and coatings technology, Volume 79, Issues 1–3, February 1996, Pages 231-239

[6] IREIS, R&D HEF Group

[7] N. Schwarzer, F. Richter, On the determination of film stress from substrate bending: Stoney's formula and its limits, 2006

[8] M. R. ARDIGO, M. AHMED, A. BESNARD - Stoney formula: Investigation of curvature measurements by optical profilometer - Advanced in Material research. - Vol. 996, n°IX, p.361-366 – 2014

[9] R. Schöngrundner, R. Treml, T. Antretter, D. Kozic, W. Ecker, D. Kiener, R. Brunner, Critical assessment of the determination of residual stress profiles in thin films by means of the ion beam layer removal method, Thin Solid Films 564 (2014) 321–330

[10] K.J. Kang, N. Yao, M.Y. He, A.G. Evans, A method for in situ measurement of the residual stress in thin films by using the focused ion beam, Thin Solid Films 443 (2003) 71–77

[11] R. Hammer, J. Todt, J. Keckes, B. Sartory, G. Parteder, J. Kraft, S. Defregger, High resolution residual stress gradient characterization in W/TiN-stack on Si(100): Correlating in-plane stress and grain size distributions in W sublayer, Materials and Design 132 (2017) 72–78

[12] H. Klöcker, Mécanismes physiques de la rupture

[13] S. Massl, J. Keckes, R. Pippan, A direct method of determining complex depth profiles of residual stresses in thin films on a nanoscale, Acta Materialia 55 (2007) 4835–4844

[14] E. Salvati, T. Sui, A. J. G. Lunt, A. M. Korsunsky, The effect of eigenstrain induced by ion beam damage on the apparent strain relief in FIB-DIC residual stress evaluation, Materials & Design 92 (2016) 649-65

[15] L. A Giannuzzi, R. Geurts, J. Ringnalda, 2 keV Ga+ FIB milling for reducing amorphous damage in silicon, Microscopy and Microanalysis 11 (2005) 828-829

[16] V. Barnier, Atomic Force Microscopy

[17] SURF group, Belgium

Chapter 3 Experimental results of DLC coating behavior and failure analysis

3.1 Introduction

The wide variety of experimental techniques discussed in chapter 2 for analyzing Diamond-Like-Carbon coatings behavior and failure can boost the understanding of the damage mechanisms of the studied substrate/coating system. In this chapter, basic characteristics of each component will be discussed first. The composition of the substrate material (M2 steel), its heat treatment cycle as well as the resultant microstructure will be detailed. Coating's thickness is quantified with a Calotest equipment and growth defects per unit surface are calculated based on SEM observations. In the following sections, results concerning standard characterization adhesion tests (Rockwell indentation, Scratch test) will be presented. Limits and drawbacks of these methods are discussed. As discussed in chapter 1, the residual stress in the film after deposition and can be important. Thus, this stress were quantified by the Stoney method based on the surface deflection measurement prior and after film deposition.

More advanced characterization techniques were also used. The stress-strain curves of the Diamond-Like-Carbon coating were determined by nanoindentation and micro-pillar compression. Young's modulus and hardness of DLC were measured using nanoindentation. A complementary technique to the classical Stoney's was also used to determine residual stress. Micro-beams were FIB milled and their deflection observed. The constitutive behavior of the substrate is determined by tensile tests and the failure strain of the DLC coating by in-situ shear tests. Finally the integrity of the interfaces DLC/WC and WC/M2-steel after deposition prior to any mechanical loading was confirmed by SEM observations on FIB milled samples.

The delamination of the DLC coating under severe tribological loading is analyzed. Geometry of the failed features (circular blisters) was measured by Atomic Force Microscope. EDX analysis allowed to the study the chemistry of the damaged surfaces. Successive FIB cross-sections reveal the initially intact interface of the coating/substrate system and clarify the damage initiation, crack propagation and blisters interaction.

3.2. Substrate/coating system and preliminary characterizations

As discussed in the previous chapter, after film deposition a series of preliminary characterizations were done prior to tribological loading of the samples. These tests either guarantee the quality of the coatings or indicate potential adhesion issues.

3.2.1 M2 steel substrate material characteristics

As already mentioned previously, the substrate material is a M2 steel (chapter 2). This type of steel is part of the high-speed steels family typically used in cutting tools. It also finds application in impact tools, milling cutters, dies and punches for cold extrusion among others. Major chemical elements are tungsten, molybdenum and chromium. A small quantity of vanadium (less than 2%) is also present.

Prior to film deposition, the substrate material was submitted to a heat treatment (figure 1a) in order to achieve the desired hardness.

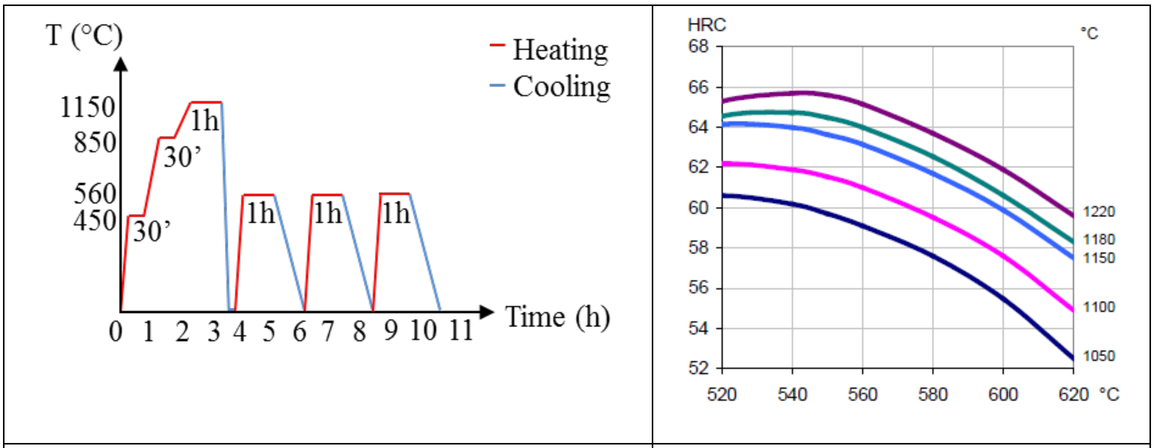

-a- -b-

Figure 1: Heat treatment cycle of M2 steel (a) and hardness in function of austenitization (right axis) and tempering (lower axis) temperature

The M2 samples were heated up to 1150°C (austenitization temperature) for 1 hour with two pre-heating steps of 30 minutes at 450°C and 850°C respectively and air quenched. A triple tempering at 560°C for 1 hour each leads to a hardness of about 64 HRC. Following the heat treatment, the samples were processed by lapping (chapter 2) leading to mirror polished surfaces.

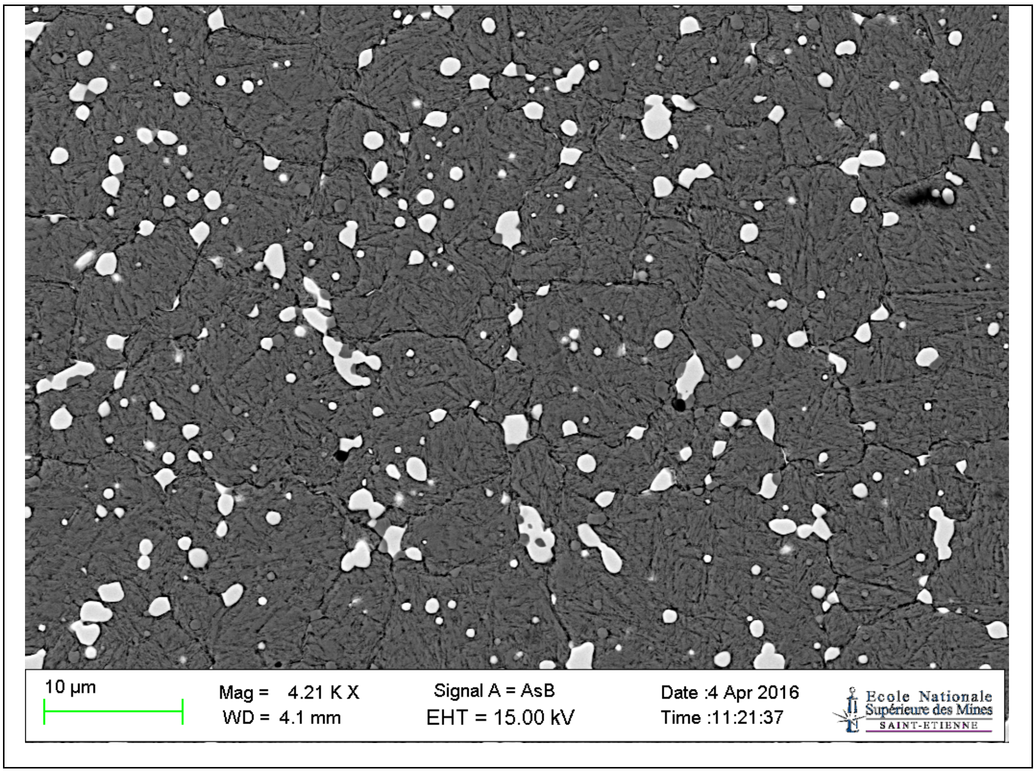

Figure 2: M2 steel microstructure after heat treatment and polishing

The final M2 steel microstructure is shown in figure 2. Steel grains as well as carbides (white features) are revealed. The average grain size is about 10 µm (±2 µm) whereas the carbide size is between 1 µm and 2 µm. Two types of carbides are present, tungsten and chromium ones.

3.2.2 Several Diamond-Like-Carbon films and interlayers

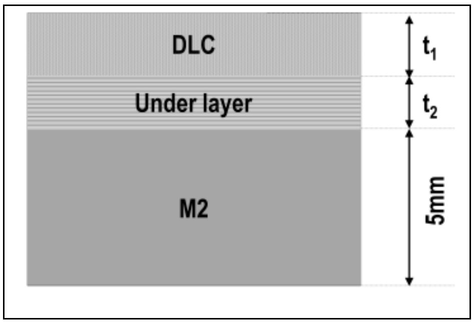

Figure 3: Schematic representation of deposited films

The interlayer and DLC coating thicknesses were systematically determined by calotests using a Genetest apparatus (chapter 2).

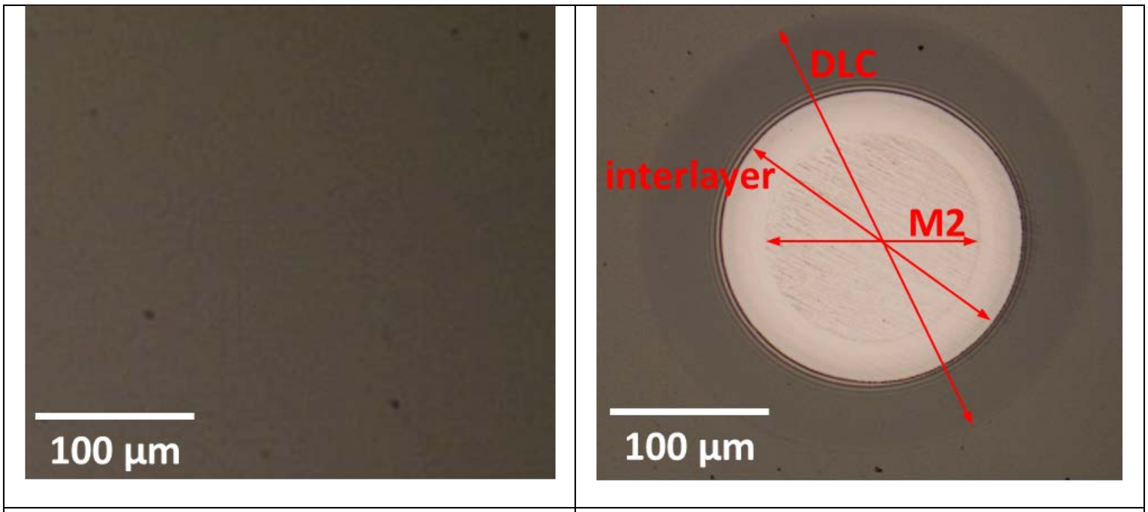

-a- -b-

Figure 4: Sample surface prior (a) and after (b) Calotest

When the calotte is gone through the coating, it is observed using an Olympus Microscope (figure 4b). Measurement of the calotte dimension allows the calculation of layers' thicknesses. The measurements accuracy is estimated to ±0.1 µm. The measured interlayer and coating dimensions are summarized in Table 2. Note, the relative error is important for thin films.

Interlayer t_2 (µm)	0.6	0.8	1.0
DLC t_1 (µm)	0.2	0.2	0.2
	1.2	1.2	1.2
	2.5	2.5	2.5

Table 2: Under-layer and DLC thicknesses, as measured by Calotest.

A variety of coating thicknesses was chosen to test the influence of the interlayer and the DLC coating on the behavior of the multilayer material.

3.2.3 Surface and growth defects of the DLC coating

3.2.3.1 Quantification of defects density by SEM observations

During film deposition, growth defects may be present at the coated material. These defects, if they are numerous, could be a possible site of crack initiation when the sample is submitted to tribological loading. Thus, these defects should be quantified and should be taken into consideration in the analysis of the coating performance.

Growth defects were quantified in a region of 0.27 mm^2 for a thin (0.2 µm) and a thick (2.5 µm) DLC coating. Both of them have an interlayer of 0.8 µm.

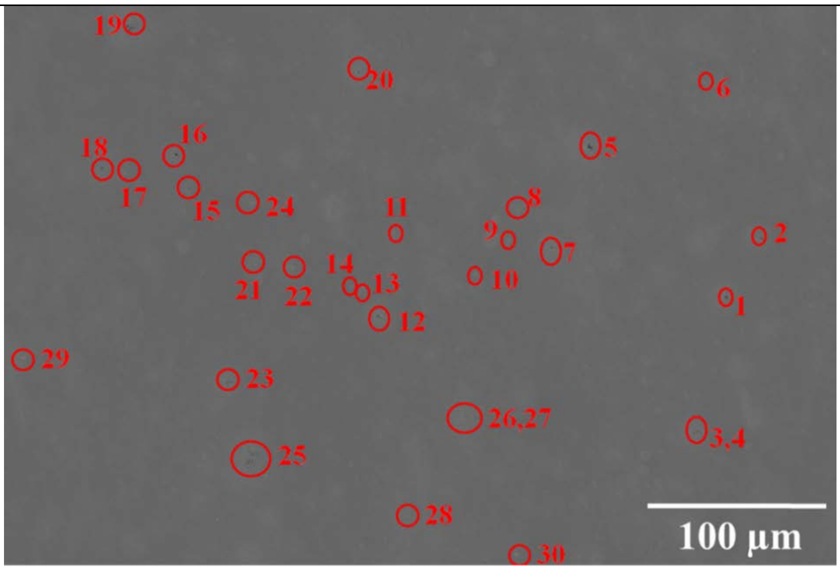

Figure 5: Growth defects for a DLC coating of 0.2 µm

Figure 5 shows a typical image of the 0.2 µm DLC observed in a Scanning Electron Microscope. Among the 30 defects (figure 5) counted for the 0.2 µm coating, 23 are growth defects leading to a number of 86 growth defects per mm^2 which is a rather important amount of defects. Two types of defects were observed, cavities (figure 6a, b) and 'cauliflower type' ones (figure 6c, d).

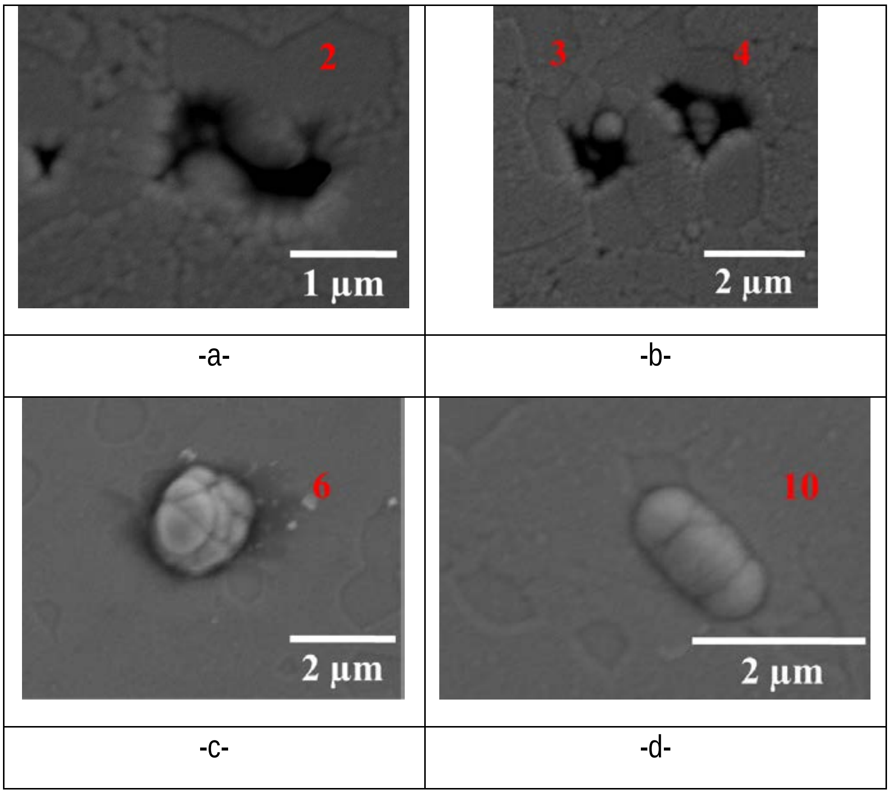

-a-

-b-

-c-

-d-

Figure 6: Surface growth defects types for a 0.2 µm DLC coating

An average diameter of 1 µm (±0.2 µm) was determined for both types of defects.

Exactly the same approach was followed for the 2.5 µm thick DLC coating. Figure 7 shows the defects detected on this film.

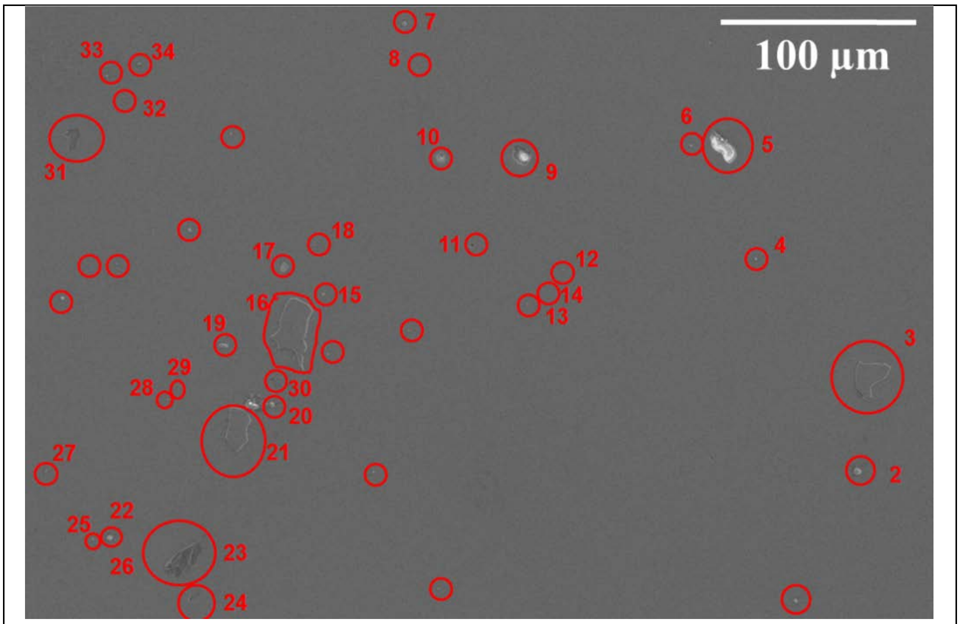

Figure 7: Growth defects for a DLC coating of 2.5 µm

A number of 34 defects were observed on this area. Hence, the number of defects can be estimated to about 90 / mm^2, similar to the 0.2 µm coating.

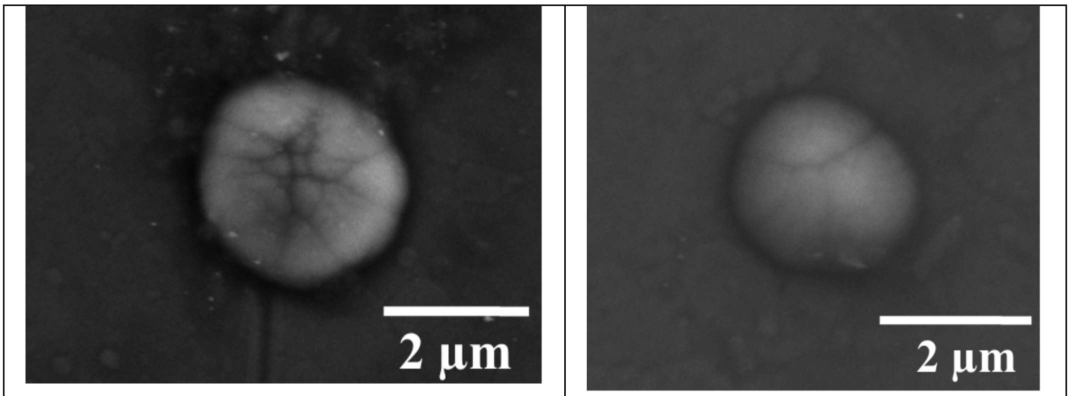

-a- -b-

Figure 8: Surface growth 'cauliflower type' defects for a 2.5 µm DLC coating

The average diameter of the 2.5 µm DLC coating defects is about 1.9 µm (±0.3 µm) almost the double of those found on the thinner coating examined previously. Henceforth, even if both coatings present more or less the same amount of defects, those of the thicker one (2.5 µm) are more prone to cause crack initiation during tribological loading.

3.2.3.2 Defects height measurement in AFM facility

The height of these growth defects was measured by an AFM facility. A surface of 60x90 µm^2 was studied for both, the 0.2 µm and the 2.5 µm DLC coating. Thin coating's defects present an average value of 0.12 µm (±0.08 µm) while those of the thicker one an average of 0.4 µm (±0.14 µm). Thus, the 2.5 µm coating exhibits not only larger but also higher growth defects which turns it into more vulnerable compared to the thin 0.2 µm film.

After having characterized the global size of these defects, a more detailed analysis could be done. A possible variation of their size through the thickness of the film would be useful to investigate. For example, a FIB-milled cross-section at the level of a defect could give important information concerning the local surface of the M2-steel as well as the local growth of the interlayer and the DLC. However, even if these coatings are found not to be perfect, local adhesion, analyzed in the following section, seems satisfying at the scale of the SEM.

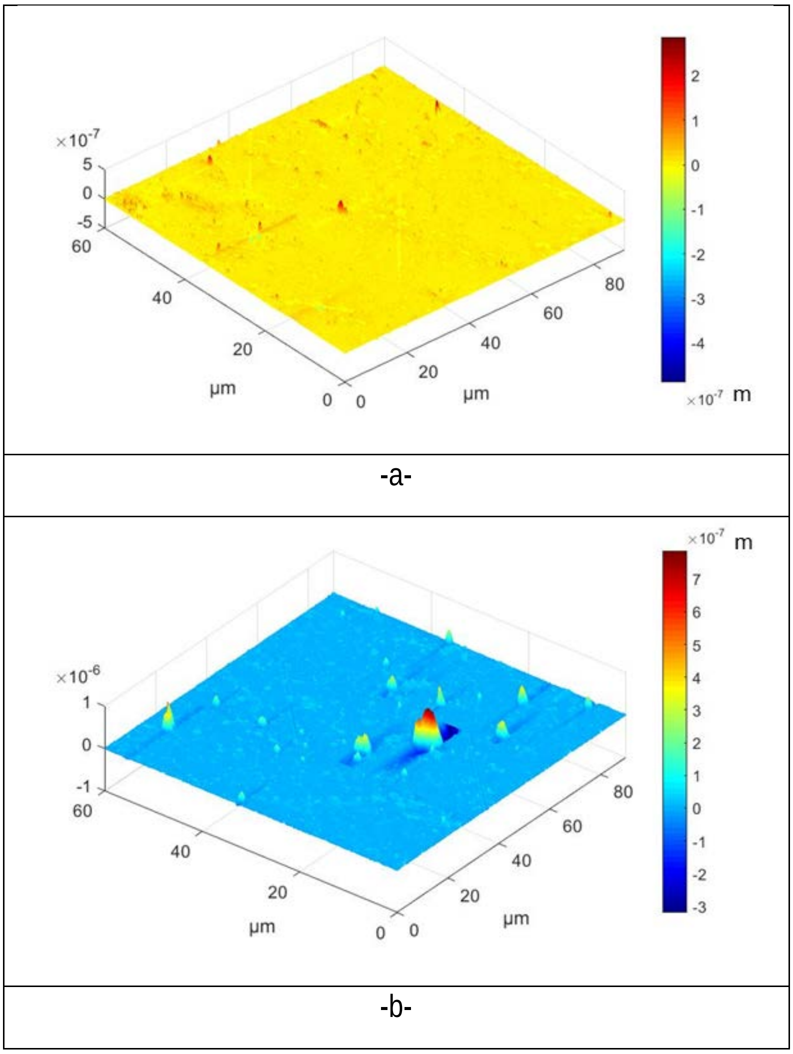

-a-

-b-

Figure 9: AFM measurement of growth defects for a 0.2 µm (a) and a 2.5 µm (b) DLC coating

3.2.4 Preliminary characterization of coating quality

3.2.4.1 FIB-milled interface observation of coated samples

The interface of the substrate/coating system was observed on FIB-milled cross-sections for several coating and interlayer thicknesses.

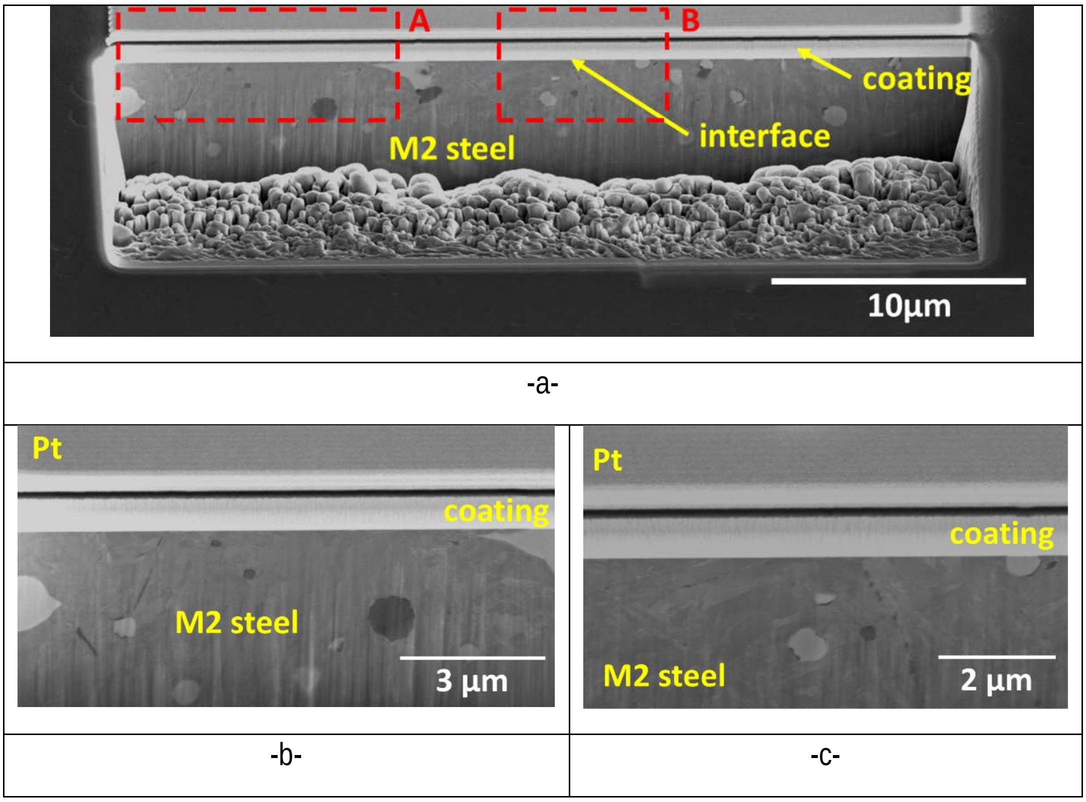

-a-

-b-

-c-

Figure 10: Cross-section of a coating with a 0.8 µm interlayer and a 0.2 µm DLC layer

Figure 10 presents a FIB-milled cross-section of a film having an interlayer thickness of 0.8 µm and a DLC thickness of 0.2 µm. As it is illustrated in details A (figure 10b) and B (figure 10c), the interface of the coated system prior any external loading is intact in the observed area and presents no SEM-visible decohesion or debonding. These observations were made outside the previously presented surface defects zone. Examination of several interlayers and DLC coatings did not reveal local interfacial decohesion.

DLC films present in some zones surface defects, usually close to the borders of the sample. Outside of these zones the interface seems intact on FIB cross-sections. Nevertheless, this does not give the value of the coating's adhesion. A simple and efficient method to classify roughly coatings adhesion is the Rockwell indentation.

3.2.4.2 Rockwell indentation adhesion control

Rockwell indentation can indicate possible adhesion problems by observation of the contour of the imprint. All coated samples were tested and analyzed under an optical microscope. The applied load was 150 kg.

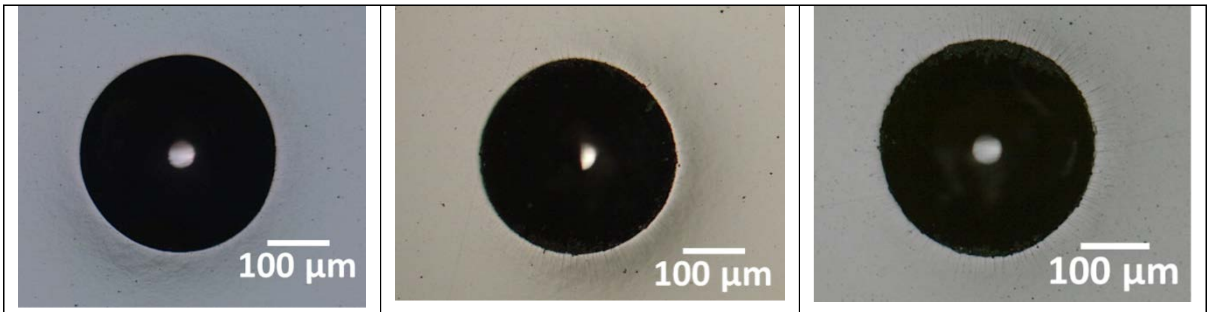

-a- -b- -c-

Figure 11: Rockwell imprints for several DLC coatings (a) 0.2 µm (b) 1.5 µm (c) 2.5 µm

Figure 11 shows the outcome of some tested samples, the smallest DLC thickness (0.2 µm), the largest (2.5 µm) and an intermediate one (1.5 µm). The interlayer was the same in all cases (0.8 µm).The grey and dark area correspond respectively to the DLC and the imprint. The size of the imprint is about 300 µm. The 0.2 µm film presented some circular cracks around the imprint whereas the intermediate one and the 2.5 µm coating show a combination of circular and radial cracks. No decohesion or coating flaking is observed. Thus, for all DLC thicknesses the adhesion is classified as HF2 (chapter 2) and consequently acceptable according to the test standards discussed in chapter 2.

If the Rockwell test leads to satisfying adhesion for all coating thicknesses, in service delamination is eventually observed. Another simple test allowing coating characterization is the scratch test.

3.2.4.3 Scratch testing of the DLC coating

Following the Rockwell indentation, specimen were submitted to scratch tests. Loading conditions in this testing facility are more severe, thus debonding is more likely to appear during this experiment. During this test an indenter starts scratching the surface of the sample with intensity increasing from 10N to 50N. The critical load at failure is determined based on the region where the first decohesion is observed and by correlating this distance to the current loading.

Scratching of the 0.2 µm DLC coating reveals no flaking. Only some small cracks are apparent next to the trace. Thus, the critical load is larger than 50N. The 1.5 µm coating exhibits a critical load of 24N. Cohesive-adhesive flaking is observed and snatching of the trace bottom at about 35N. Concerning the thickest coating (2.5 µm), cohesive flaking is noticed too at about 22N. Snatching of the bottom of the trace is present after the load of 38N. Consequently, no significant delamination is found for all films.

It seems that the critical delamination load decreases rapidly with the DLC coating thickness. In other words, if the thickness of DLC increases, more important residual stresses and hence a decrease of the additional load causing delamination are expected.

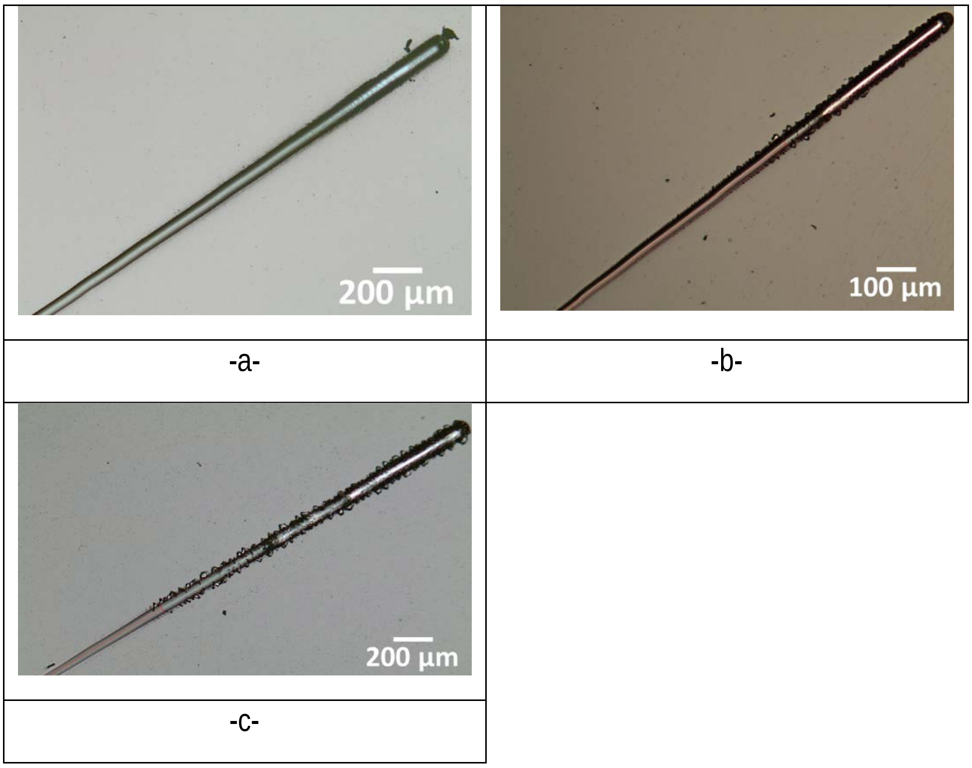

-a-

-b-

-c-

Figure 12: Scratch test for several DLC coatings (a) 0.2 µm (b) 1.5 µm (c) 2.5 µm

3.2.5 Residual stress characterization

3.2.5.1 Quantification of residual stress – Stoney's method

The residual stress was calculated based on the change in curvature prior and after film deposition (chapter 2). Table 3 shows stress values for the interlayer thickness of 0.8 µm.

DLC t_1 (µm)	0.2	1.5	2.5
σ_f (GPa)	-1.2	-1.7	-2.0

Table 3: Residual stress in the DLC for an interlayer thickness t_2=0.8µm

The characterized compressive stress is in the order of -1.2 GPa even for the thinnest DLC coating (0.2 µm). The residual stress increases with the thickness of the film up to -2.0 GPa for the thickest coating (2.5 µm).

Two measurements per coated sample were performed in order to characterize the residual stress. A number of 24 specimens (two for each thickness) was used. The size of the wafers was carefully chosen according to the limitations of Stoney's method to avoid errors in stress calculation. Standard deviation from the mean value of stress is found to be ±0.1GPa. A normal distribution is supposed to determine the error bars. The error is found to be independent from the film thickness as presented in chapter 2 (section 2.3.1).

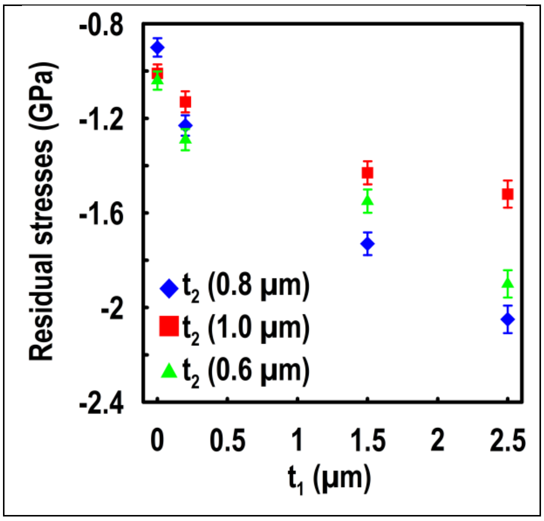

Figure 13: Residual stress measured by Stoney's method applied to coated wafers as function of the DLC coating thickness, for three different t_2 thicknesses of adhesion layers.

Figure 13 depicts the compressive residual stresses as function of the film thickness. For all combinations, the absolute value of the stress increases with the DLC coating thickness. The interlayer thickness seems to have no first order influence on the residual stress values.

3.2.5.2 Validation of calculated residual stress on FIB-milled micro-beams

Stoney's method requests measurements on Si coated wafers. To verify the stress distribution on M2-steel coated samples, micro-beams were prepared with a FIB facility (chapter 2). One side was built-in while the other was milled having free edge boundary condition (figure 14). Deflection was measured and compared to a finite element model (chapter 4) having as input the residual stresses calculated previously.

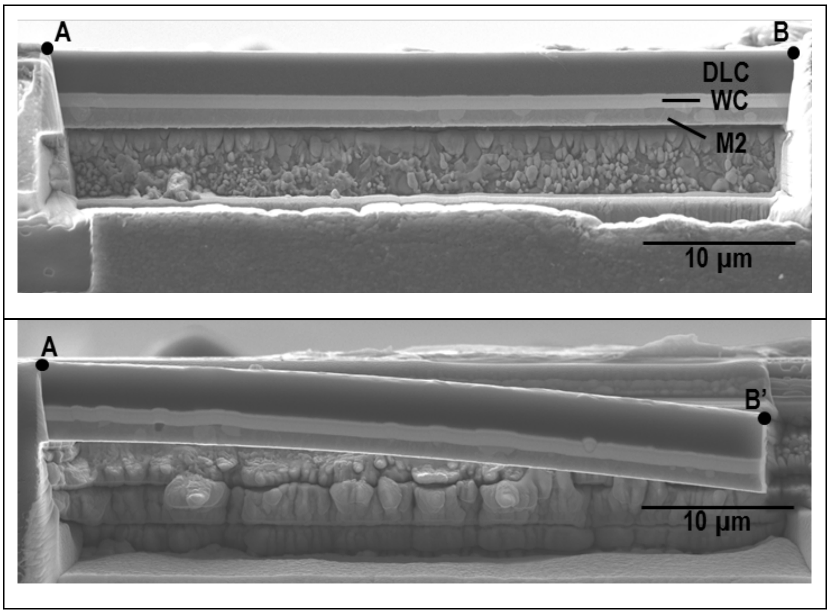

Figure 14: Typical FIB milled micro-beam for a DLC of 2.5µm (a) built-in on both sides, (b) with residual stress induced deflection.

Several thicknesses of the M2 steel were chosen varying from 1 µm to 5 µm. The DLC and the interlayer thicknesses were the same for all micro-beams (2.5 µm and 0.8 µm respectively). The deflection along the line AB as well as the maximal deflection at point B were determined experimentally. The maximal deflection depends linearly on the residual stresses in the interlayer and the DLC coating. The deflection along line AB can be represented by a parabola. From the simple beam model we can determine the deflection U_{max} for two different M2 steel thicknesses ($U^{(1)}_{max}$ and $U^{(2)}_{max}$). Thus, by solving the following system of equations we can estimate the value of residual stresses in the DLC and in the interlayer.

$$\begin{bmatrix} U^{(1)}_{max} \\ U^{(2)}_{max} \end{bmatrix} = \begin{bmatrix} a_{11} & a_{12} \\ a_{21} & a_{22} \end{bmatrix} \begin{bmatrix} \sigma_{DLC} \\ \sigma_{int\,erlayer} \end{bmatrix} + \begin{bmatrix} R_{(1)} \\ R_{(2)} \end{bmatrix} \tag{1}$$

$$\begin{bmatrix} \sigma_{DLC} \\ \sigma_{int\,erlayer} \end{bmatrix} = \begin{bmatrix} a_{11} & a_{12} \\ a_{21} & a_{22} \end{bmatrix}^{-1} \left\{ \begin{bmatrix} U^{(1)}_{max} \\ U^{(2)}_{max} \end{bmatrix} - \begin{bmatrix} R_{(1)} \\ R_{(2)} \end{bmatrix} \right\} \tag{2}$$

The stress values obtained by this inverse method are in close agreement with the Stoney method. However, the matrix A can sometimes be ill-conditioned giving numerically very huge or very small values leading to errors. Thus, by multiplying the measurements we can have accurate results. Note, each measurement implies a FIB-milled micro-beam.

In section 2, the coating's surface was characterized under a Scanning Electron Microscope, the interface was examined through FIB-milled cross-sections and typical adhesion control techniques (Rockwell indentation, scratch test) and the residual stresses were quantified. This procedure closes the qualification of the coatings after film deposition. The next step is to characterize the DLC coating material.

3.3 Mechanical properties of the DLC coating

DLC coatings are deposited on a surface to protect it and extend its life cycle. These coatings present high residual stresses. Thus, the film hardness controls to a large extend its future use.

3.3.1 DLC hardness and stress-strain curve

Young's modulus and hardness of DLC coating were measured using nanoindentation (Nanoindenter XP, Agilent) at loads smaller than 15 mN to avoid influence of the substrate. The Young's modulus is about 230 GPa (±10 GPa), a micro hardness of 26 GPa (±2 GPa) and a yield stress of 15 GPa (±1.5 GPa) (KER08, Mech Mat). Moreover, micro-pillars (~1.4 µm diameter and ~1.17 µm height) FIB milled in the 2.5µm DLC coating, were deformed in situ with an Alemnis SEM Nanoindenter (chapter 2).

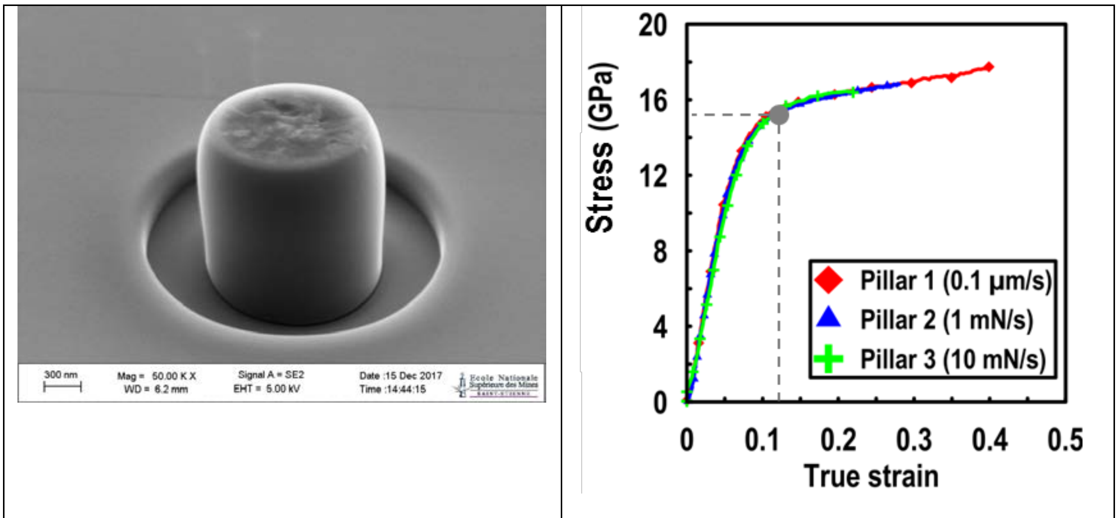

-a- -b-

Figure 15:DLC behavior: (a) compressed nano-pillar, (b) stress-strain curve and nanoindentation results

Figure 15 depicts the results of two load and one displacement controlled test. The values of the yield stress determined either by micro-pillar compression or by nanoindentation are very close. Note, that the DLC coating exhibits small strain hardening but significant yielding, up to more than 20% under uniaxial compression. The DLC coating is deformable under uniaxial compression. However, the critical strain at coating's failure under tension needs to be identified.

3.3.2 In-situ shear testing of Diamond-Like-Carbon

DLC coated M2-steel samples were loaded under uniaxial traction as presented in chapter 2. The geometry of the central area of the sample leads to pure shearing of the DLC coating (figure 16a).

Nevertheless, the samples unexpectedly failed (figure 16b) at a load of about 2400N and a displacement of 135 µm without prior evidence of DLC failure. The grey area in figure 16b is the central part of the sample. Theoretically, at failure, lines at 45° to the tensile direction should appear on the DLC surface. Probably, a robust steel as the M2-steel, after its heat treatment, is not deformable enough and cannot lead to a successful analysis of the failure strain of the DLC coating.

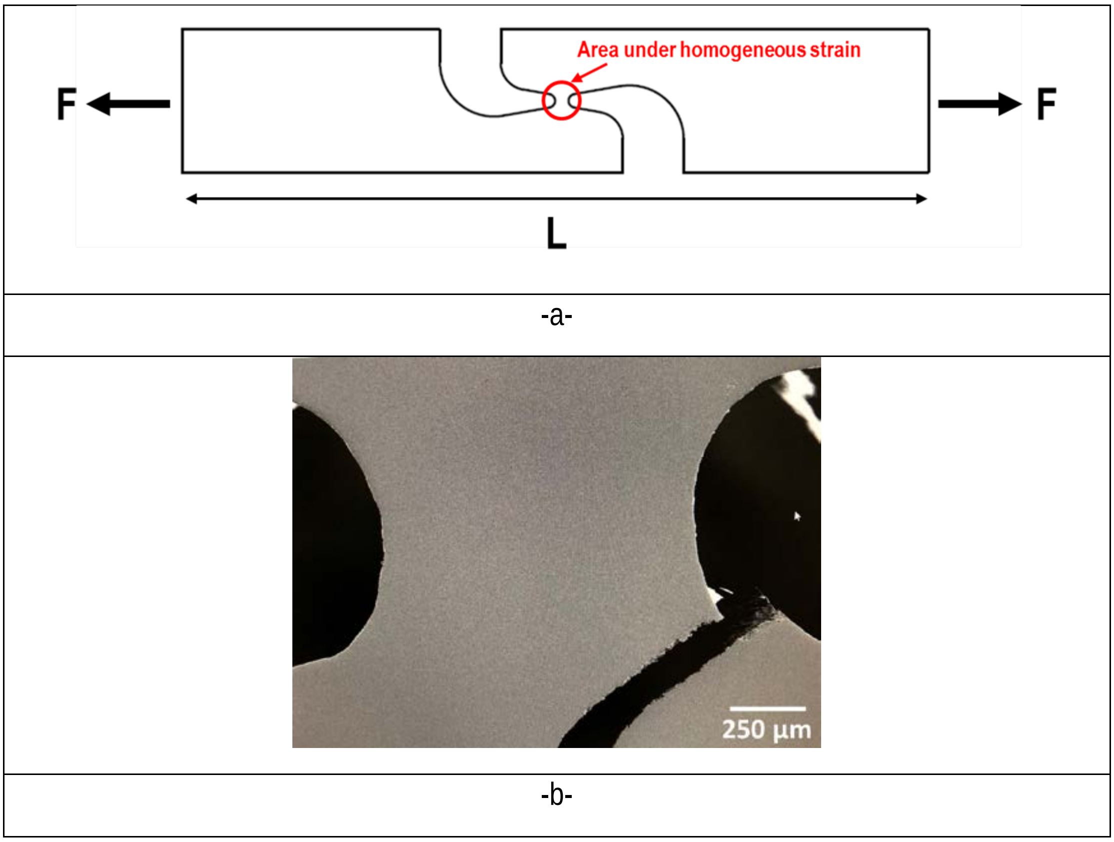

-a-

-b-

Figure 16: In-situ shear test representation (a) and unexpected failure of the sample (b)

3.4 Tribological testing of DLC coating findings

Coating's and interface quality as long as the residual stress due to film deposition were determined. The DLC's behavior was determined too. In this section, the in-service performance and behavior of the DLC coatings are presented. For simulating the in-service loadings, a 'ring- plane' experiment was used. All DLC coatings were submitted to severe loading conditions with the tribological setup discussed in chapter 2. The wear trace after the experiment (figure 17) was observed under a Scanning Electron Microscope.

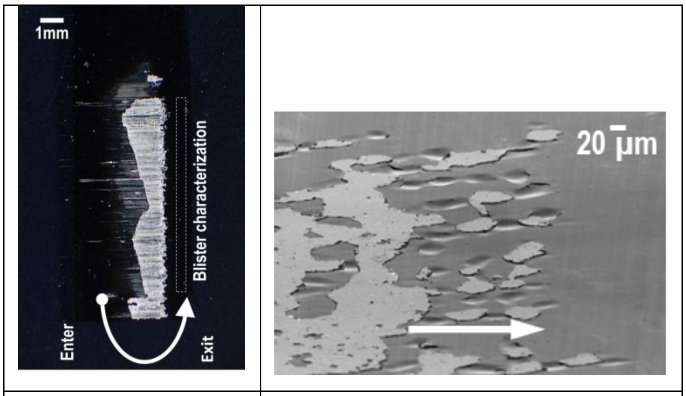

- a - - b -

Figure 17: Severe tribological test for accelerated wear. (a) Wear trace, (b) typical blister configuration at the exit of the wear trace.

The width of the wear trace is the same as the ring's width (8 mm) and its length is 2 mm due to the in-plane movement of the sample. The black region in figure 17a corresponds to the DLC coating, whereas the grey one to the interlayer. In figure 17b the dark region corresponds to the DLC and the light grey one to the interlayer or the steel substrate. The friction direction is indicated by the white arrow. At the ring exit complete coating delamination is observed in the form of elongated blisters aligned along the friction direction. Several blisters exhibit partially cracked boundaries. Moreover, regions corresponding to the blisters size are completely removed. In this view, blisters seem to have a rather homogeneous size and present a more or less regular order in the space (network).

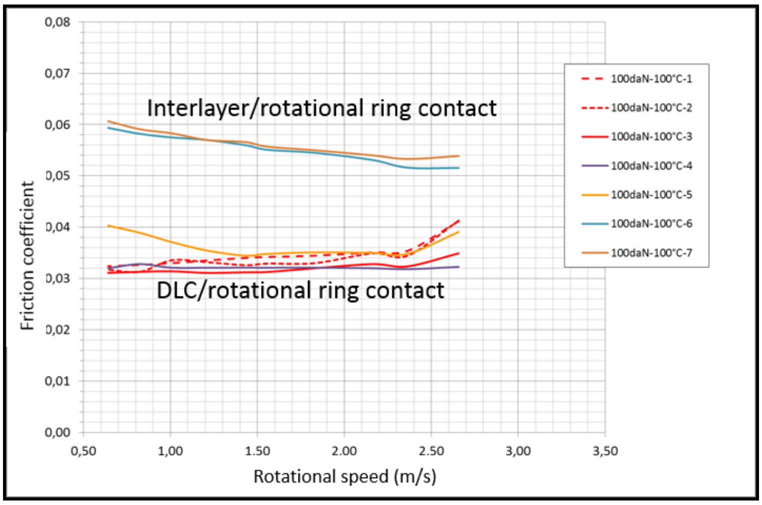

Figure 18: Friction coefficient during the tribological experiment

During the test, the friction coefficient was measured (figure 18). The tribological test starts with the highest rotational speed and ends with the lowest one. Successive test cycles of the experiment may be necessary. Each line in the graph represents the friction coefficient measured during a test cycle ('run'). An extremely low friction coefficient is noticed for the DLC coating-rotational steel ring contact. An increase in this coefficient means that the ring is no more in contact with the coating but with the interlayer, hence the wear level is advanced.

Typical blisters' dimensions:	Diameter: 30-40 µm , Height: 1-2 µm
Typical blisters' inter-distance:	5-30 µm
Contact zone of 'ring-flat plane' test:	~16 mm^2
Size of Rockwell imprint:	Diameter ~300 µm
Size of a Scratch test imprint:	Length ~1 mm

Table 4: Size comparison between operating scales and delaminated features

Blisters forming a network and exhibiting cracked borders are novel results compared to observations compared to scratch or a Rockwell indentation test results. These tests cannot reproduce the interaction between blisters simply because they operate at a very small scale. In order to simulate the friction of two moving components with a millimetric contact surface (as in real automotive components), a tribological experiment in the same scale should be performed.

Delaminated features (blisters) were noticed after tribological loading of the DLC coatings. A further analysis of the local delamination mechanisms will be presented in section 5.

3.5 Delamination and failure features analysis

3.5.1 SEM characterization of wear surfaces

Careful examination of the damaged surface next to the wear trace (ring's exit) leads to supplementary findings concerning blistering. Figure 19a presents blisters cracked at their boundaries (interlayer 0.8 µm – DLC 2.5 µm). Figure 19b shows two blisters exhibiting completely removed coating (interlayer 0.8 µm – DLC 1.5 µm). Closer observation of the blister boundaries (interlayer 0.8 µm – DLC 0.2 µm) reveals local decohesion and debonding of the film.

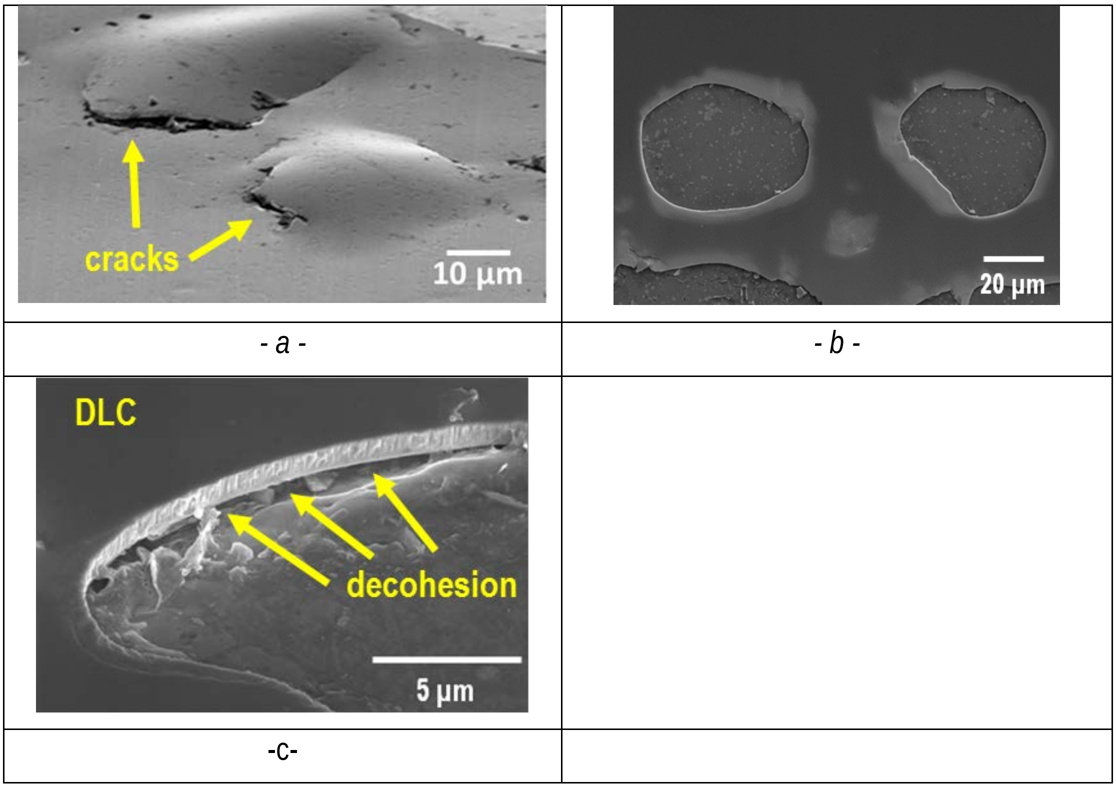

- a -

- b -

-c-

Figure 19: Blisters with cracked boundaries (a) Blister with removed coating, (b) and delaminated blister boundary (c)

In order to examine the interior of the blisters, EDX analyses were performed. An example of these analyses is given for an interlayer of 0.8 µm and a DLC of 2.5 µm (figure 20).

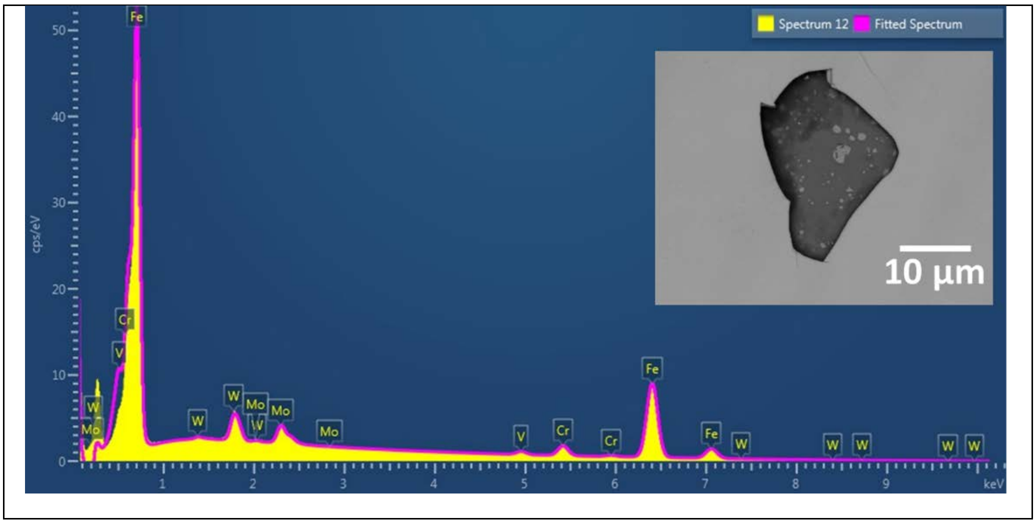

Figure 20: EDX spectrum of removed blister's analysis

The major element detected is iron (Fe), meaning that the film is completely removed in the center of the blister. Molybdenum, chromium and vanadium are also detected at quantities close to the nominal content in M2 steel. There is no evidence of remaining coating parts.

In the following section, blisters' dimensions are determined by AFM measurements. These dimensions (radius, height) are analyzed later in the mechanical analysis.

3.5.2 Atomic Force Microscopy characterized blisters

3.5.2.1 AFM measured blisters size

In order to better understand and analyze delamination, the blister geometry was measured. For this purpose, an AFM facility was used. Characterization was realized in terms of maximal deflection (δ) and blister's radius (R).

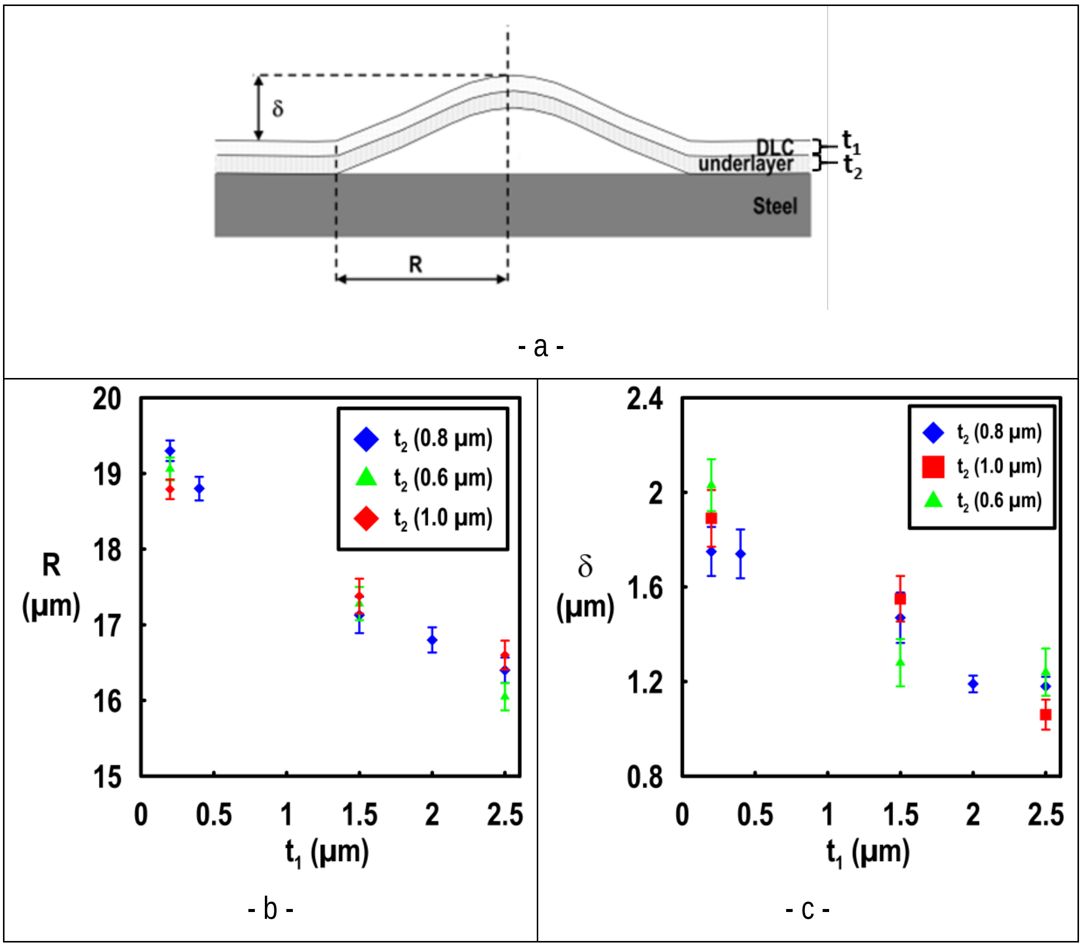

- a -

- b -

- c -

Figure 21: Blister geometry (AFM results): (a) schematic cross section of a blister, (b) mean blister radius R as function of the DLC thickness, (c) mean maximum deflection δ as function of the DLC thickness.

Due to the size limits of the AFM equipment (maximum scanning zone of 30 µm x 30 µm), four measurements per blister were performed in order to fully characterize its size. At least 12 blisters were characterized for each coating system leading to a complete statistical analysis.

Eleven different films were studied. Figure 21 depicts the buckling induced by tribological loading. Table 5 summarizes the corresponding results. These results should hence correspond to the post-buckling analysis of Hutchison et al. Figure 21 shows the mean values of the blister radius and blister height as a function of the DLC thickness. The blister radius R and the maximum deflection δ decrease if the DLC coating thickness is increased. Throughout this thesis, we will consider only the ***initial*** DLC coating thickness (measured by Calotest). During the tribological loading, the DLC thickness might decrease significantly due to wear. This aspect will be discussed shortly hereafter, but no systematic measure of the DLC-thickness at the onset of buckling was done.

The standard deviation (represented by the error bars) seems to be smaller for the radius measurements than the height. Thin coatings are found to present a larger deflection (1.8-2.0 µm) and radius (±19 µm) than the thicker ones. In general, blister dimensions decrease with the thickness of the DLC coating. This is the case for all interlayers tested.

t_1 (µm)	t_2 (µm)	δ (µm)	R (µm)
0.2	0.8	1.75±0.10	19.30±0.14
0.4		1.74±0.10	18.80±0.16
1.5		1.47±0.11	17.13±0.24
2.0		1.19±0.04	16.80±0.17
2.5		1.18±0.04	16.40±0.17
0.2	0.6	2.03±0.11	19.06±0.15
1.5		1.28±0.10	17.28±0.22
2.5		1.24±0.10	16.05±0.18
0.2	1.0	1.89±0.12	18.79±0.13
1.5		1.55±0.10	17.38±0.23
2.5		1.06±0.06	16.60±0.19

Table 5: AFM results : blister radius, height

3.5.2.2 Blisters and stresses in the coating

Hutchinson and al. [44] developed an equation to describe the buckling stress of thin films based on the film properties (Young's modulus, Poisson coefficient) and the geometrical characteristics of the film (thickness h , radius of blister R).

$$\sigma_c = 1.2235 \frac{E_1}{\left(1-\nu_1^2\right)} \left(\frac{h}{R}\right)^2 \tag{1}$$

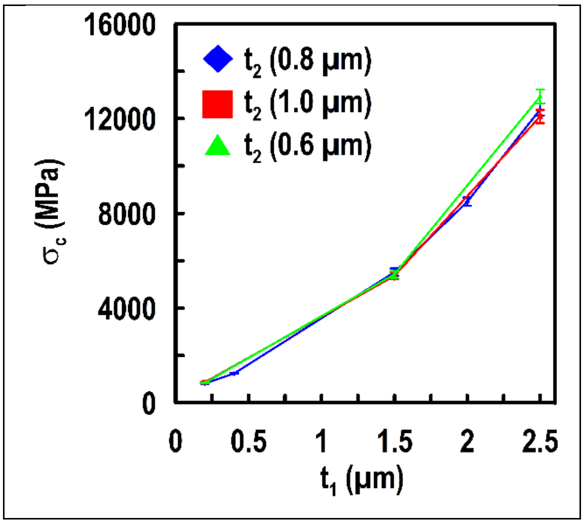

Figure 22: Buckling model predictions applied to the present coatings

Before, applying Hutchinson's model to present results, we would like to outline the major limitations. First, the blister radius at the very onset of buckling is not known. The informations available concern post-buckling behavior. Moreover, the effective film thickness at the onset of buckling (and hence during blistering) might be much smaller than the initial coating thickness due to the wear of the latter. Nevertheless, it seems useful to try a first estimate of the buckling stress predicted by Hutchinson's model. This model leads to an extremely high buckling stress (figure 22). Comparing these values to the residual stress calculated with the Stoney formula (figure 13) leads to the conclusion that critical buckling stress is almost 7 times higher than the measured residual stress determined previously. Hence, despite, all the limitations cited above, we suggest that :

1) the tribological loading induces extremely high local stresses

2) the wear of the coating prior to buckling seems a significant factor.

As described by Hutchinson and al., for stresses in excess of a critical value, the film buckles away from the substrate. The value (σ/σ_c) can be estimated by the AFM measurement results, i.e. the δ/h ratio. Thus, the post-buckling stress can be obtained by the AFM measurements.

$$\frac{\delta}{h} \cong \left[\frac{1}{c_1}\left(\frac{\sigma}{\sigma_c}-1\right)\right]^{1/2} \qquad (2)$$

$$c_1 = 0.2473(1+\nu_1) + 0.2231\left(1-\nu_1^2\right) \qquad (3)$$

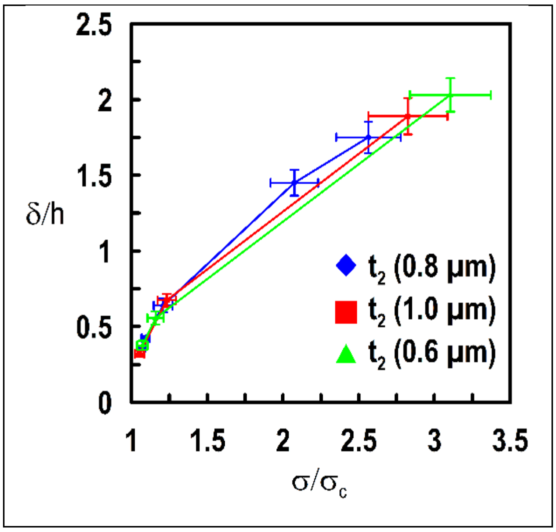

Figure 23: Buckling model predictions combined to AFM measurements

The critical buckling stress predicted by this model is enormous. The post-buckling stress is even much higher. Thus, deflection δ and radius R are underestimated by the theory of Hutchinson. This could be explained by the fact that the film is not homogeneous but consists of two components (interlayer and DLC) and that the boundary conditions considered by the model are restricted. In fact, Hutchinson and al. consider only blisters with built in boundary conditions. In the current work, cracked-border blisters are observed. This result seems to have an important influence on film's deflection.

At this point, we conclude that:

The model of "perfect" circular blisters does not match the experimentally observed shape and that the following observations indicate the most significant role played by the tribological loading:

1) blisters are arranged in a network determined by the friction direction
2) blister height and radius reveal an enormous local stress and thinned coatings
3) blisters exhibit cracked boundaries.

In the next section, damage initiation, interface crack propagation and blister interactions will be analyzed.

3.5.3 Damage characterization with FIB-milling

Figure 24 shows a SEM picture of a typical blister after FIB milling. Not only the DLC coating (2.5 µm) but also the interlayer (0.8 µm) can be observed. The friction direction is shown by the yellow arrow. The FIB-milled blister is about 30 µm away from the wear trace. The structure of the M2 steel substrate is revealed and its carbides are visible.

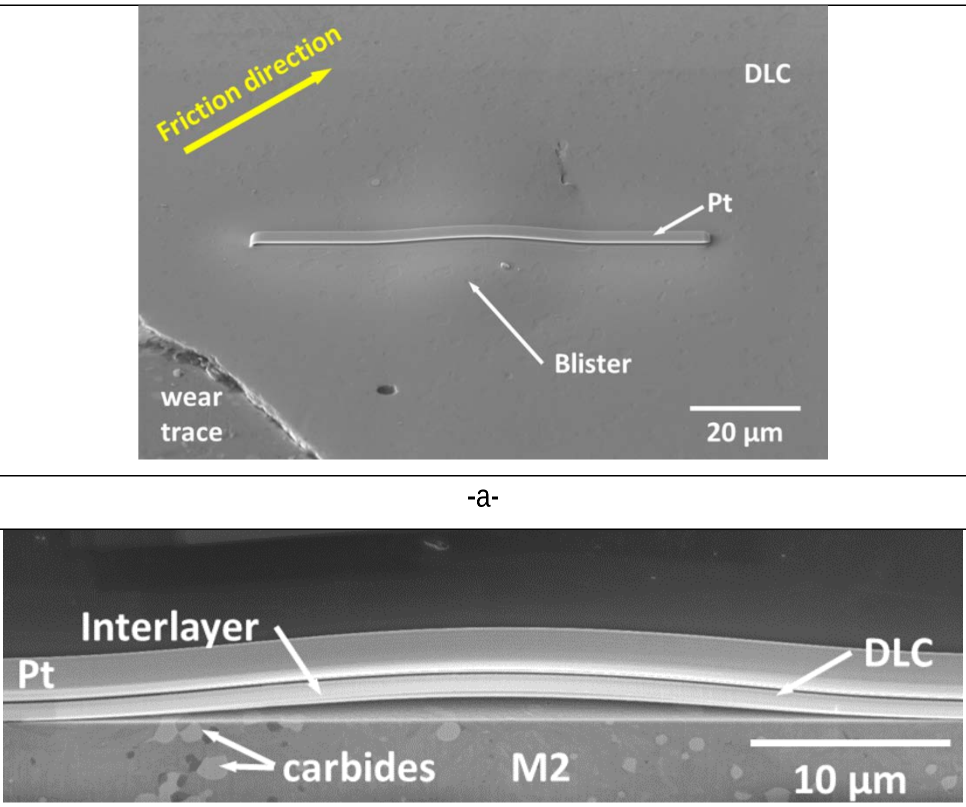

-a-

-b-

Figure 24: FEG-SEM observation of a typical un-cracked blister, after FIB milling.

3.5.3.1 Blister borders and boundary conditions for buckling analysis

The boundaries of this FIB-milled blister seem identical to those taken into consideration by Hutchinson et al. for describing circular blister delamination (tangent zero). However, this is not always the case. Figure 25 presents the cross-section of a 2.5 µm thick DLC coating. The cross-section was done parallel to the friction direction. The left border of this bister is already cracked (figure 25b) while failure is visible at the surface of the blister prior milling. Thus, the angle between the blister border and the substrate is not zero in this case. To the best of our knowledge, theoretical models consider only built-in borders corresponding to non-cracked films. This result is innovative comparing to existing theory.

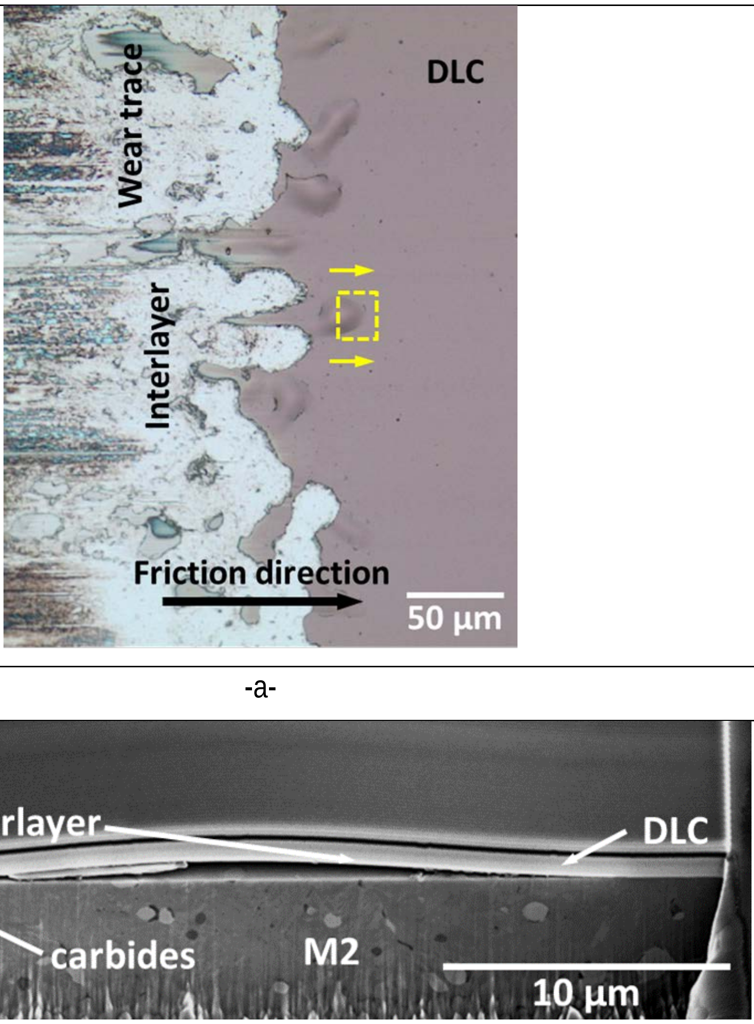

-a-

-b-

Figure 25: FEG-SEM observation of a typical cracked blister, after FIB milling

Going back to figure 24b analysis, the milling reveals the M2-steel microstructure with carbides, as well as the architecture of the coatings consisting in the superposition of the interlayer and the DLC films. It is interesting to observe that the blister consists of the entire multilayered film, which seems to be completely delaminated from the steel substrate. However, crack detection between the layers is not feasible due to the precision of the microscope. On the SEM picture, the blister borders seem to be tangent to the substrate.

Another case of different boundary conditions is presented in figure 26 for a thin DLC coating of 0.2 µm. Small cracks (fig. 26b, c) are observed perpendicular to the interface at both sides of the cross-section.

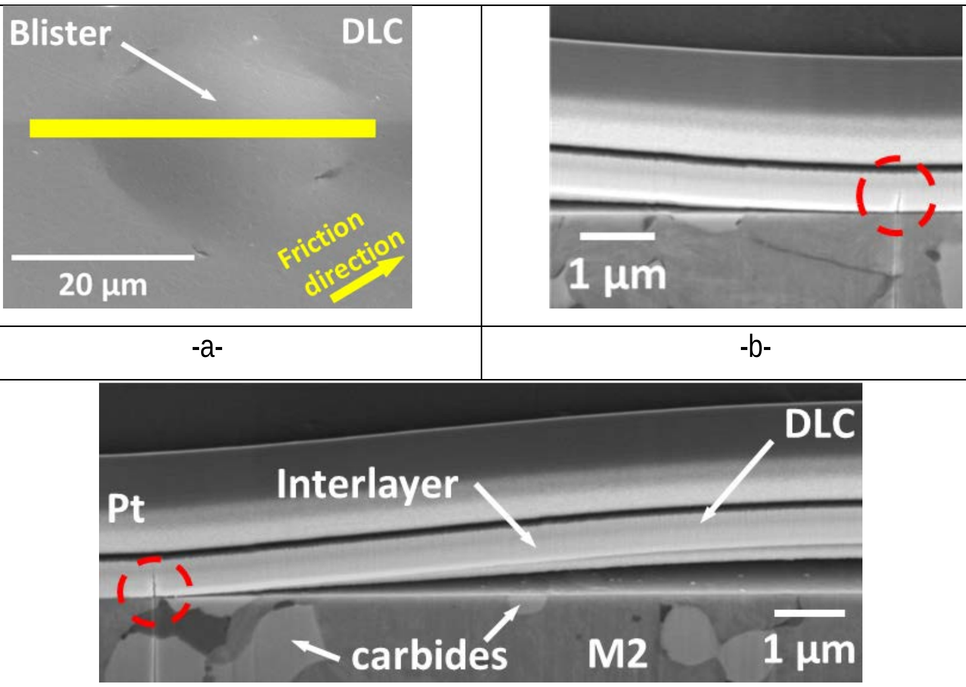

-a- -b-

-c-

Figure 26: FEG-SEM observation of a cracked-border blister (DLC 0.2 µm)

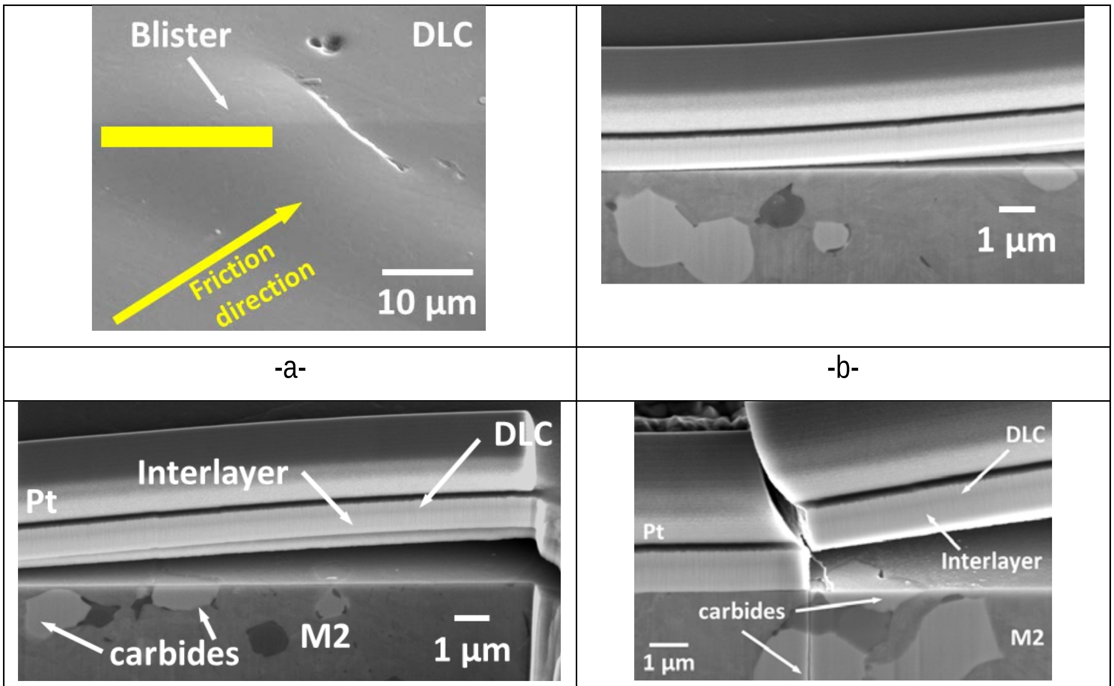

-a- -b-

-c- -d-

Figure 27: FEG-SEM observation of a cracked-border blister (DLC 1.5 µm)

Another case of possible boundaries is presented in figure 27 for an intermediate thickness of DLC coating (1.5 µm). The left side of the blister border has a zero angle with the substrate (figure 27b). However, the right side is completely cracked. An inverse view of the completely delaminated border is shown if figure 27d.

The previous observations may be summarized as follows. Cracked blister borders may be observed for all DLC coating thicknesses. A buckling analysis, taking into account partially cracked blisters, should be considered to model correctly DLC coatings blistering.

3.5.3.2 Delamination and damage nucleation

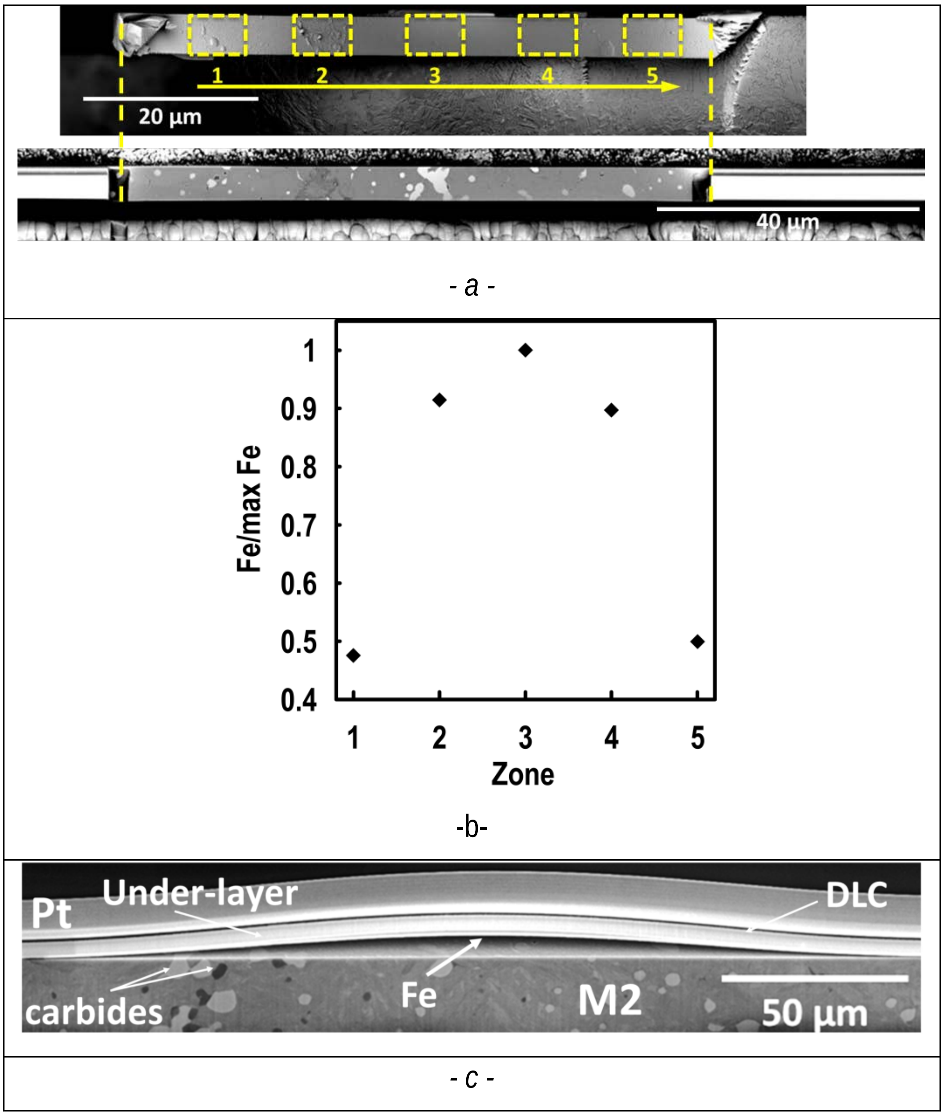

- a -

-b-

- c -

Figure 28: The 5 zones analyzed by EDX (a), Relative values of EDX-Fe intensity (the maximum was arbitrary fixed to 1.0 for zone 3 exhibiting the highest Fe intensity signal; (b), Position of the Fe-layer (c)

Under the interlayer, a very thin layer of material was detected. To analyze this thin layer, and more particularly the surface which has undertaken delamination from the M2-steel substrate, FIB milling was continued. A small strip of the film was FIB cut and returned by a micro manipulator inside the FIB. Figure 28a shows the initial and final orientation of the film. Moreover, figure 28a shows the film in its final position with identification of zones labelled 1 to 5. EDX measurements have been performed on these five zones. The operating current was 10kV and the film was tilted at 50 degrees. EDX revealed essentially the presence of iron, as shown in figure 28b. The maximum intensity is reached in the center (zone 3). Thus, for this coating, blister nucleation starts at some nm beneath the interlayer inside the M2-

steel. This result is new compared to the existing literature and should be further investigated. The influence of the surface preparation of the M2-steel prior film deposition may lead to removal and redeposition of tiny steel particles. In addition, the presence or not of zones without adhesion at the DLC/substrate interface prior to external loading should be checked. However, the latter is not simple and quick to validate due to the enormous number of observations needed. Blisters are nucleated in the M2-steel substrate. The next step consists in understanding how the blisters spread out, i.e. where crack propagation occurs.

3.5.3.3 Blister growth and interface crack propagation

During blister growth, the thin Fe layer decreases to zero. Hence, the crack propagates parallel to the M2-steel interlayer interface. But, as seen on figure 29, at some point, the interface crack deviates and propagates through the interlayer and coating. Crack initiation in the substrate material can be due to contact fatigue which leads to very local yielding and rupture of the M2 steel. Crack deviation and blister nucleation are addressed in the following paragraphs. Finite element modeling of the contact will explain this result and clarify the observed delamination phenomenon (chapter 4).

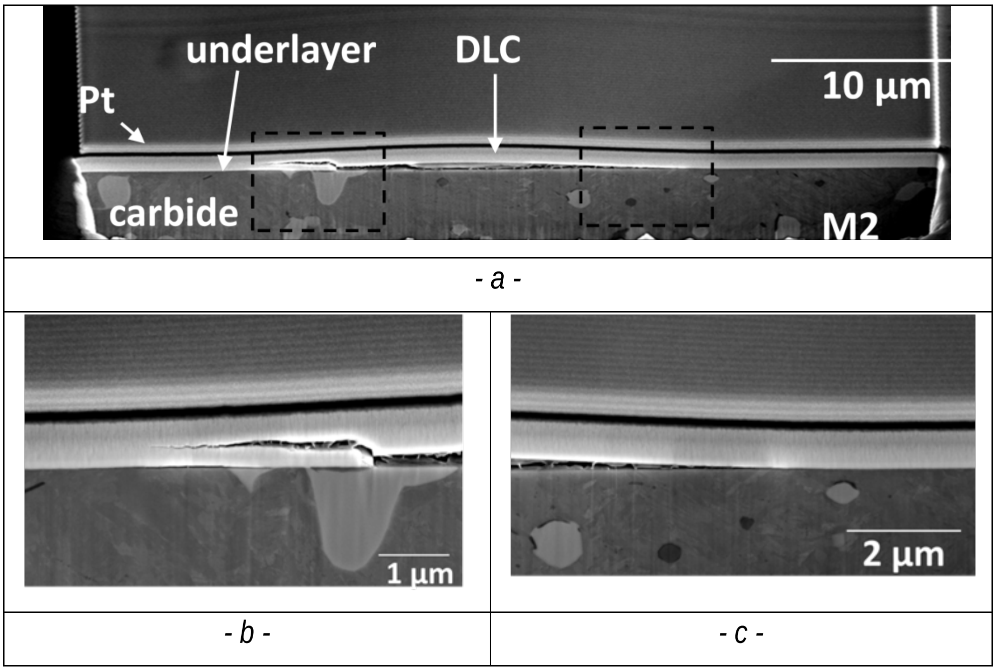

- a -

- b - *- c -*

Figure 29: Changes in the crack path due to the local substrate microstructure.

Buckling of 1.5 µm DLC coatings was also analyzed after FIB milling. Figure 29 displays a typical result. On the right side, the dashed-line area, magnified in figure. 29c, shows that the interface crack starts at very small depth inside the M2-steel and then propagates almost parallel to the interface. But, as shown in the left dashed-line area, magnified in figure 29b, if the crack path crosses a large carbide, crack deviation into the interlayer is observed. Crack deviation due to the presence of carbides was observed on all the cross sections. This corresponds to more than 10 observations for the DLC coating thickness of 2.5 µm and a similar number for a DLC thickness of 1.5 µm. Thus, the crack path is thoroughly controlled by the very local microstructure at the crack tip. The interface crack, governing blister growth, deviates from the substrate coating interface, depending on the heterogeneity of the substrate, as highlighted here by the effect of the carbides.

Carbides effect on delamination is a new and innovative result. Possible choice of a steel with smaller grains or with more grains could change the response of the interface after mechanical loading. This fact should be investigated in future works.

At this point, decohesion was shown to nucleate in the M2 substrate. Then the blisters spread out by crack propagation parallel to the M2-steel WC interface. Finally, crack deviation towards the outer surface, and hence possible complete coating removal occur at carbides.

The yet open questions are:

- the coating wear prior to decohesion, buckling and debonding
- the influence of the initial surface defects prior to tribological loading

Blister interaction is possible. Coating wear prior to decohesion will not be addressed in the PhD thesis. As mentioned previously, analyzing experimentally the influence of surface defects prior any tribological loading implies the observation and characterization of an enormous amount of samples. This is left for future work. But, a first attempt to model the influence of initial surface defects will be presented in the next chapter. In the following section, we try to analyze the influence of blister interdistance or otherwise blister interaction.

3.5.3.4 Blister interaction

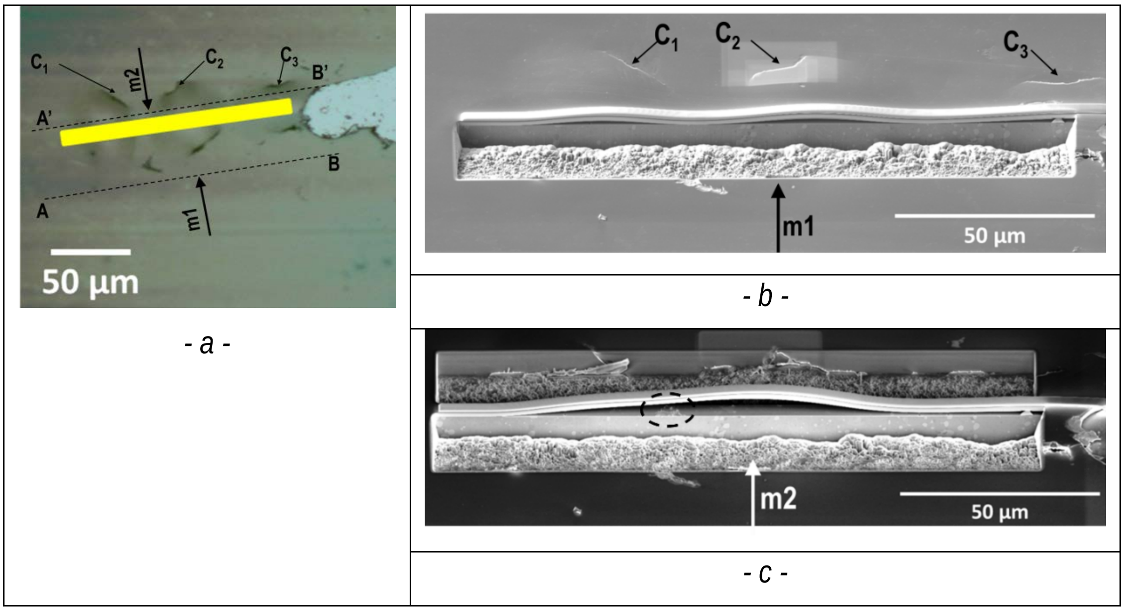

- a -

- b -

- c -

Figure 30: In situ observation of adjacent blisters. (a) Initial surface, (b) observation after one-sided FIB milling. (c) observation after two-sided FIB milling.

Figure 30 shows a FIB-milled cross-section of three neighboring blisters. The aim of this experiment is to study the blisters interaction due to their proximity. Surface cracks (C_1, C_2, C_3) were present prior to milling. FIB milling was first performed along direction m1. The result is highlighted in figure 30b. Three distinct blisters may still be observed. During the FIB milling, the surface cracks did not grow, nor the blisters. Then FIB milling was completed along a second direction m2. The outcome is shown in figure

30c. The blisters coalesced spontaneously to form one single large one. Hence, this effect suggests that large blisters may be created by coalescence of smaller ones also during tribological testing. Thus, any further loading during the friction process would lead to coalescence and formation of a larger blister. The last experiment leads to deeper understanding blister coalescence which may be induced by local debonding followed by buckling with concomitant interface crack propagation. However, local debonding may take place at the substrate-interlayer, the interlayer-DLC interface or correspond to a crack inside a particular material. In present experiment depicted in Fig. 30, the tribological induced crack is formed some nanometers inside the M2-steel and propagate to form three independent blisters (Fig. 30a, b).

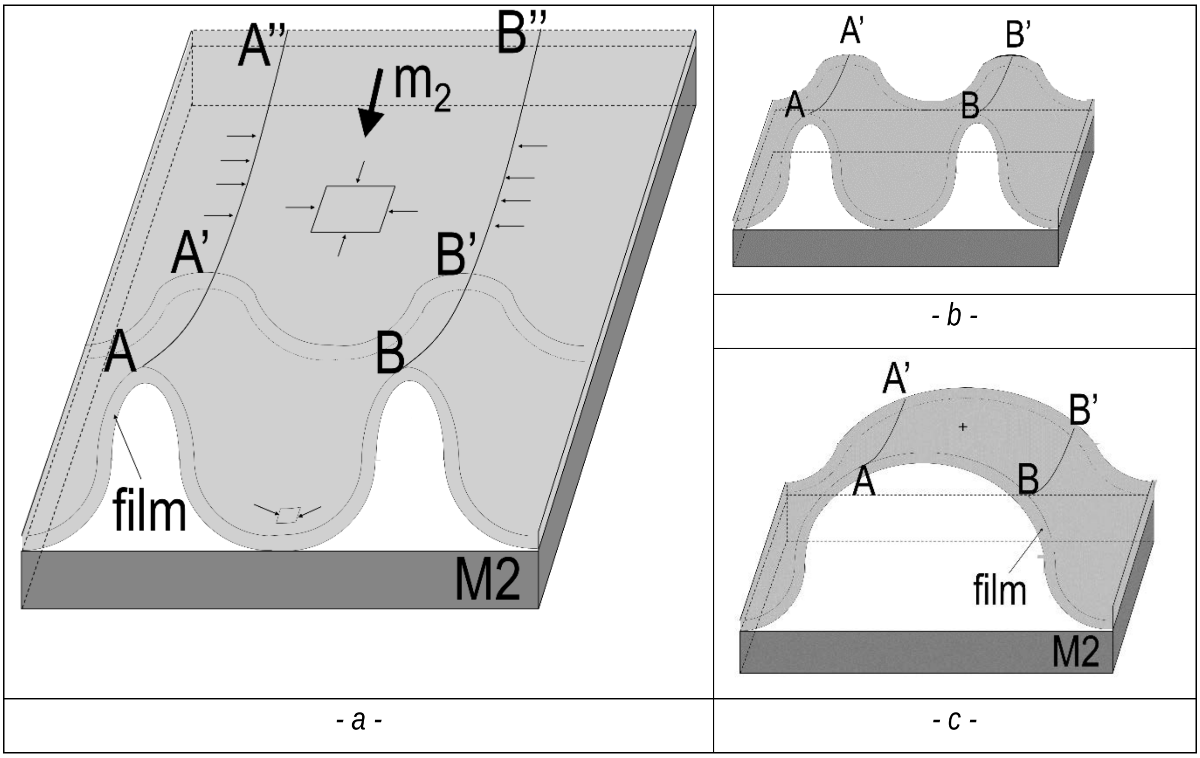

- a -

- b -

- c -

Figure 31: Schematic representation of two adjacent blisters. (a) prior to FIB milling along direction m_2, unstable (b) and (c) stable configurations after FIB milling along direction m_2

Prior to FIB milling along direction m2, the high compressive stresses combined with good adhesion in region A'A"B'B" (Fig. 31a) prevent buckling in region AA'BB'. After milling along direction m2 (Fig. 31b), these stresses do no more hold the strip AA'BB' and hence it buckles. Hence the previous blisters coalesce (Fig. 31c). If we observe the failure mode of the small residual layer of DLC localize within the dashed lines in figure 30c, we clearly observe that this failure mode distinguishes significantly from the wear-induced failure observed previously. Wear induced crack initiation might be due to contact fatigue in the M2-steel, whereas, blisters coalescence clearly corresponds to “ductile” rupture of the small M2-steel ligament left prior to the second FIB milling.

3.6 Conclusions

In this chapter, DLC coatings behavior deposited onto M2 steel substrate was investigated. The DLC coating/M2 steel substrate system characteristics were analyzed prior external loading. The stress-strain curve of the DLC film was obtained as well as its hardness by means of nanoindentation and micro-pillar compression. Young's modulus, hardness and yield stress were determined with high accuracy. Moreover, FIB cross-sections revealed the intact interface of the structure after film deposition. No SEM-visible decohesion was detected.

The samples were submitted to severe tribological loading to simulate their behavior and test the adherence of the interface. Blisters forming a network and being oriented in the friction direction were found after the experiment. This result cannot be reproduced by Rockwell indentation or scratch tests because they operate in a smaller order of magnitude. In addition, blisters presenting cracks in their borders were detected. To the best of our knowledge, this configuration is not considered in the existing models. Thus, in future works it should be analyzed to predict more accurately circular blisters deflection and behavior.

Residual stresses are found to vary between -0.8 GPa for the interlayer and -2.0 GPa for the thick DLC coating (2.5 µm). The absolute stress values increase linearly with film thickness. AFM measurements of blisters dimensions shows higher blister radii and deflections than predicted by the buckling of perfectly built-in coatings.

FIB observations of several blisters cross-sections revealed crack initiation in the substrate material. This was validated by local chemical EDX analysis which shows the presence of iron (Fe) in the layer of material attached beneath the interlayer. This completely new result opens a field of future developments. The influence of the substrate surface preparation should be analyzed. Fatigue induced local yielding may also plays a role. Preparation of thin specimens at the contact zone to be observed with by TEM requires new investigation.

Cracks are found to deviate at the carbides. Thus, the local M2 steel microstructure controls crack propagation. This novel finding could lead to the optimization of the coating/substrate couple. A systematic study is needed, correlating the size of carbides and their spatial distribution to crack deviation.

Neighboring blisters interact with each other. During FIB milling they often coalesce and form a larger delaminated area. This analysis is only possible with the present tribological experiment. Actually, this interaction can be observed by loading a minimum area of material. It could be interesting to make a statistical analysis of the surface defects prior external loading and their relationship to the regular spacing of the blisters after tribological loading.

Further knowledge about damage mechanisms and propagation will be achieved in chapter 4. The contact between the Diamond-Like-Carbon coating and the rotating ring is finite-element simulated. Furthermore, blister evolution is FE-modeled as well as blisters interaction and proximity in order to analyze more widely delamination and better understand buckling and blistering.

Chapter 4 Modeling of DLC blister driven delamination submitted to contact loading conditions

4.1 Introduction

Previous chapters highlighted the buckling and subsequent failure of Diamond-Like-Carbon coatings due to tribological loading conditions. In this chapter, blister driven delamination will be analyzed by mechanical models. Existing contact models and new finite element simulations should allow to answer partially the question of blister nucleation and propagation. For this purpose, stresses and displacements generated in the DLC coatings and the steel substrate will be estimated and comparisons of the results to the experimental observations will be made. The influence of blisters neighboring will also be examined. Finally, the interface failure will be analyzed. In the following section, we present a short reminder of Hertz' contact analysis and an application of the latter to DLC coatings.

4.2 Hertz based modeling of contact pressure in DLC coatings

4.2.1 Contact pressure distribution

Hertz was one of the first who analyzed the stress distribution between two bodies in contact. Johnson, based on the Hertz contact theory, developed the necessary equations to describe the sliding contact between a plane surface and a cylinder. This model was analyzed in chapter 1 (see 1.3.1).

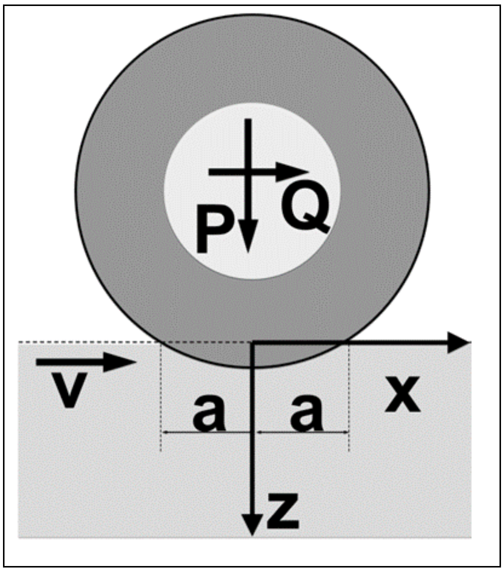

Figure 1: Scheme of a plane surface in contact with a cylinder.

In order to calculate the elastic stresses due to the tangential and normal tractions, the Hertz theory is applied. The two bodies can each be considered as elastic half-spaces in the proximity of the contact region. In chapter 1 the following expression for the contact with a and pressure distribution p(x) were given

$$a^2 = \frac{4PR^*}{\pi LE^*} \quad p(x) = \frac{2P}{\pi a^2}\sqrt{\left(a^2 - x^2\right)} \tag{4.1}$$

where P is the normal force, R^* the reduced radius (eq.1.75), E^* the reduced modulus (eq.1.76) and L is the length of the contact.

Based on this model, we will estimate the stresses generated during the tribological test presented in chapter 2 consisting of the contact of a DLC coating with a cylindrical steel ring. Note, for simplicity reasons, only the properties of the M2-steel substrate are considered in this analysis. The center of the contact area is shown in figure 1 by the axis x and z. The contact area, denoted 2a, is 0.31 mm wide for a load P=1000N and contact length L=8 mm. The radius of the cylinder is 17.5 mm and the elastic properties of the substrate material are v_1=0.3 and E_1=210 GPa.

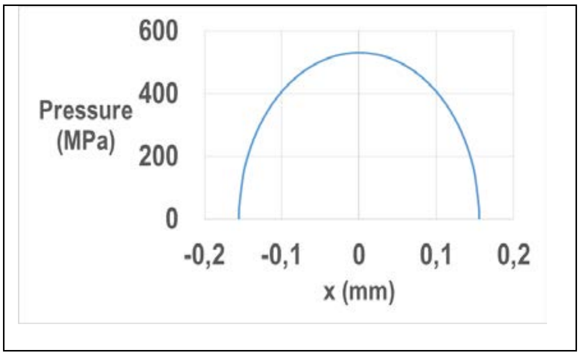

Figure 2: Pressure distribution during a plane surface / cylinder contact

The elliptical pressure distribution is depicted in figure 2. The maximal value, 530 MPa, occurs at the center of the contact at x=0. The contact pressure is zero outside of the contact area (-0.1554 , +0.1554). *The mesh refinement in the following finite element analyses will be based on the area determined by Hertz' theory of elastic contact.*

Another significant aspect of contact modelling prior to establishing numerical models is the local material behavior. A first estimation of the stress field based on Hertz' theory allows to locate zones with the potential risk of yielding (in the M2-steel) and of potential debonding (at the interface). These aspects are addressed in section 2.2.

4.2.2 Maximum shear stress in Hertz' model with friction

4.2.2.1 Volume submitted to high contact stresses under pure contact loading

From Hertz' solution, the stress field may be known in the presence of friction. The expressions of the stress tensor components are given in chapter 1 (1.81 to 1.91). In present analysis, we consider essentially the maximum shear stress distribution. The maximum shear stress, may either cause yielding of the M2-steel or decohesion of the interface. The maximal shear stress distribution due to the contact pressure without friction is plotted (figure 3) within a distance ±2a.

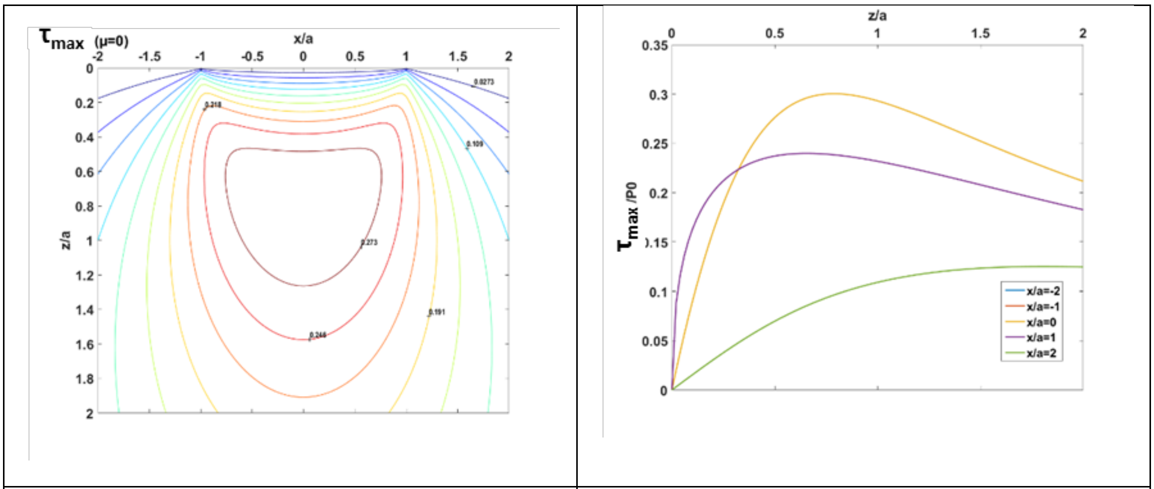

-a-

-b-

Figure 3: Maximal shear stress under the contact without friction (μ=0).

The highest value of shear stress occurs in the center of the contact and at a distance z=0.3a in the substrate material (figure 3b). Note, the stress field is symmetric in the absence of friction. Hence, without residual stress or shear loading, Hertz' elastic solution predicts a "volume "of 2a*0.3a under significant stress. In the following F.E. analyses this volume will be meshed with an element sized smaller than 0.3a/10.

4.2.2.2 Volume submitted to high stresses under contact, friction loading and residual stress

a. The effect of the residual stress

Linear elasticity allows superposing Hertz' solution with the residual stresses measured in the DLC coating to determine the stress field. The resultant shear load is shown in figure 4. Stresses are plotted along the line A-A'.

Only consideration of the elastic contact stress (figure 4b) shows low shear stress in the material. On the contrary, the superposition of the residual stress (-2 GPa for the thickest DLC film) leads to significant rise of the maximum shear stress (figure 4c). Without, taking into account friction, the stress distribution exhibits perfect symmetry. Hence, at this point we may conclude to a significant increase in the maximum shear stress due to the residual stress. On the other hand, the volume affected by high stresses does not change significantly.

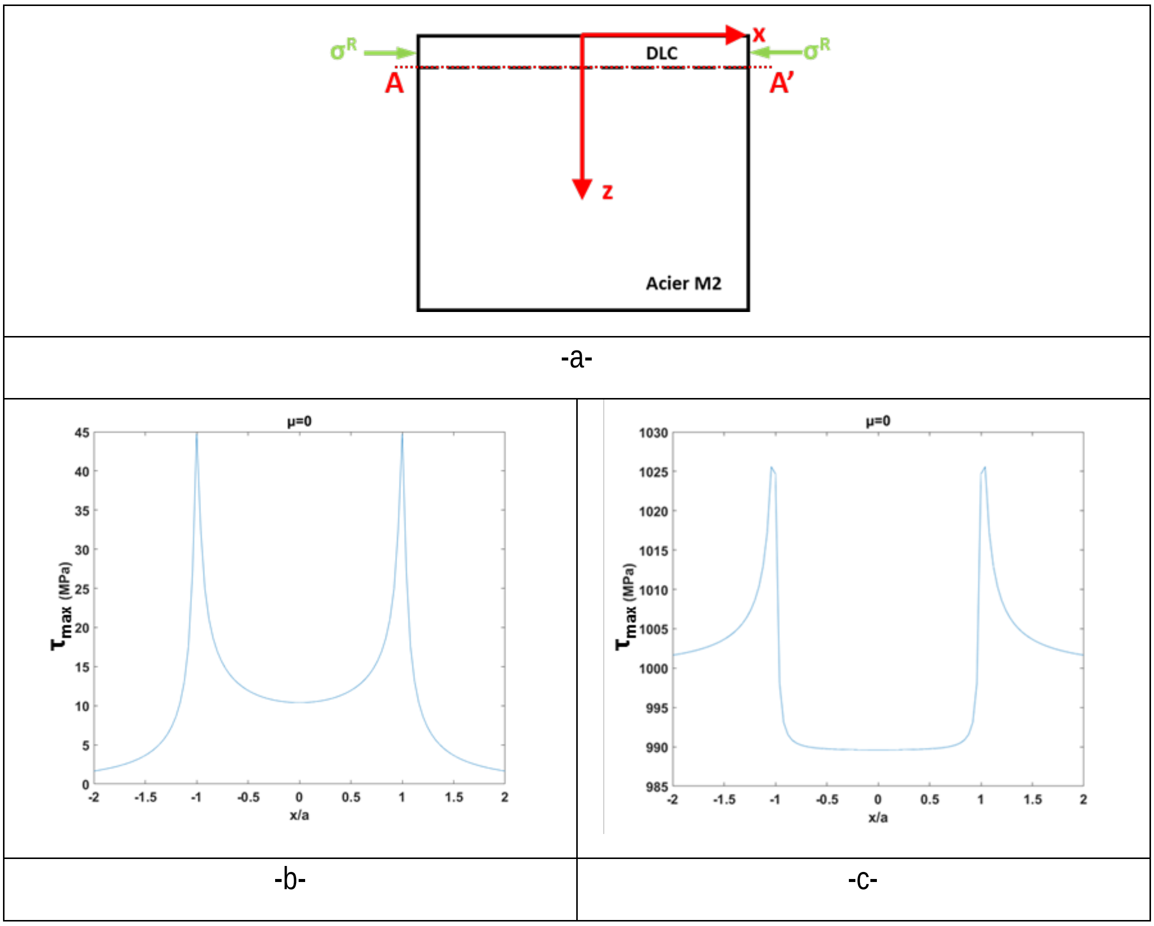

-a-

-b-

-c-

Figure 4: Superposition of the residual stress and the stress of Hertz elastic contact theory

b. The effect of friction

During the tribological experiment, the friction coefficient has been measured and recorded continuously. Very small friction coefficients are obtained with the DLC coating. In present analysis, we do not attempt to model friction. We will consider significantly higher values of the friction coefficient as those measured experimentally. This assumption corresponds to the fact, that at a very local scale the friction coefficient may of course vary significantly due to local wear of the coating. As long as the stress distribution given in chapter 1 for frictional contact summed with the residual stress leads to an elastic behavior the following analysis is correct. In the other case, the following analysis gives useful indications for the future finite element analysis. Figure 5 depicts the distribution of the maximum shear stress corresponding to a frictional contact with 2 friction coefficients of respectively 0.01 and 0.02. All the data are given for a unit contact pressure.

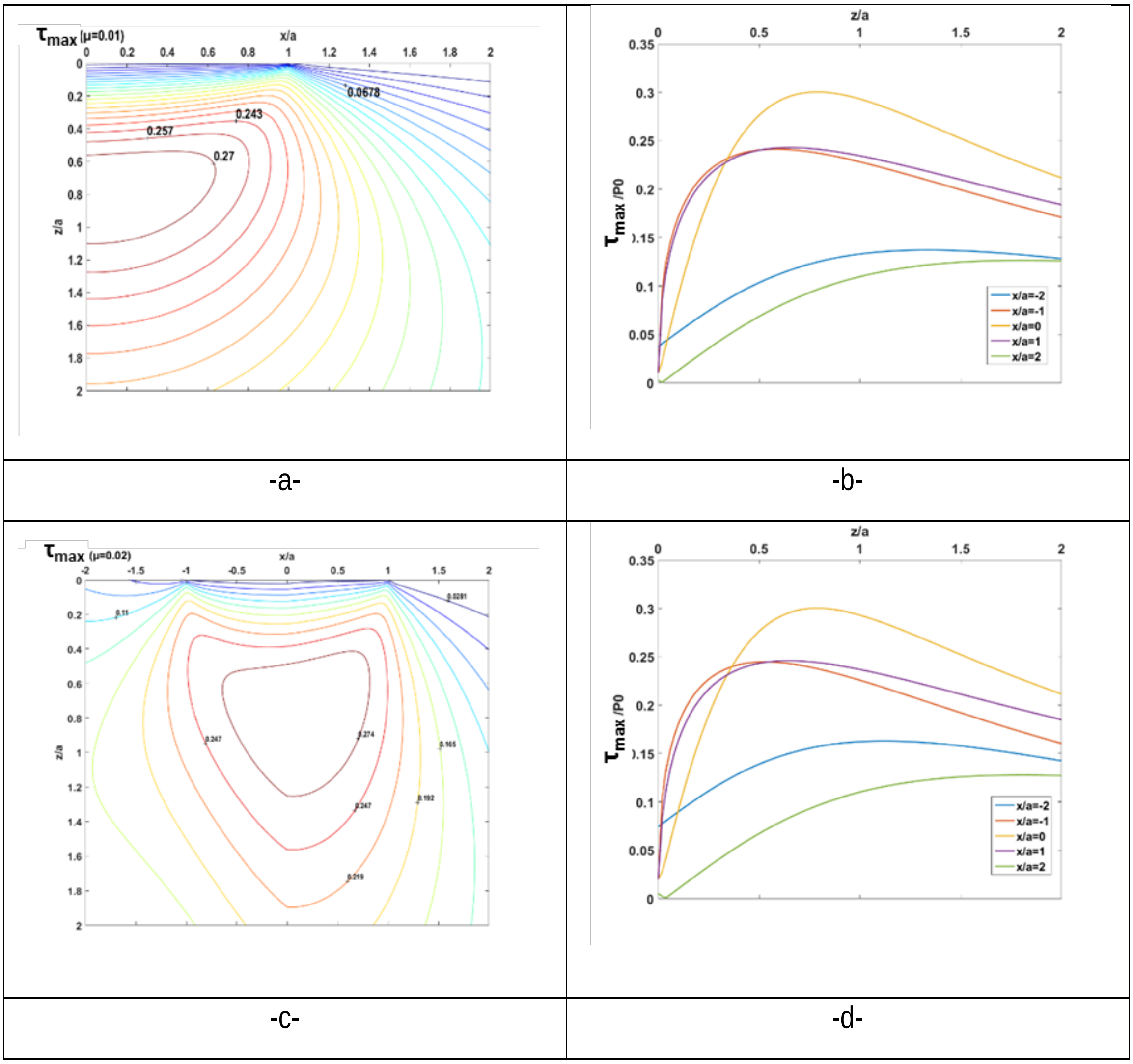

Figure 5: Stress field beneath the contact for a friction coefficient of 0.01 (a,b) and 0.02 (c,d).

Friction, even with “small” coefficients leads to

- a strong increase in the maximum shear stress,
- a strong dissymmetry in the stress distribution,
- the same volume affected by the stress increase beneath the contact.

As an illustration, figure 6 depicts the maximum shear stress distribution for friction coefficient of 0.1. This exceptional high value would correspond to a local disappearance of the coating.

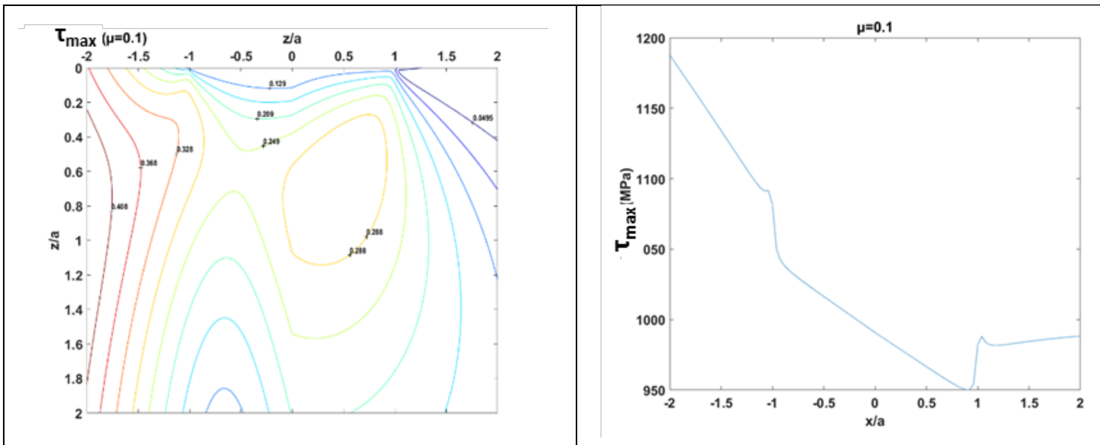

-a- -b-

Figure 6: Stress field with a friction coefficient of 0.1

Further rise in the friction coefficient influences significantly the stress field beneath the contact and thus the estimation of the stress state becomes more complicated and the validity of this extended model is limited. Very high stresses may be reached due to an increased friction coefficient. Of course, the assumption of an elastic material will fail. But, the volume affected by this increase is almost constant and limited to 4a*0.3a. This will be used to define the refined mesh in the following sections.

4.3 DLC coating with an initial unbonded zone

4.3.1 Description of the finite element model

Buckling driven delamination has been analyzed and modeled by many researchers. One of the most known works in the field is presented by Hutchinson. More details about this model are given in chapter 1. This model considers the buckling of a circular plate forming a blister of radius R with a maximal deflection δ once a critical stress (σ_c) is achieved. Inspired by this approach, a 3D finite element model was developed in ABAQUS in order to analyze the stress strain field around existing blisters. For this purpose, a representative volume element size of the structure was chosen (figure 7a).

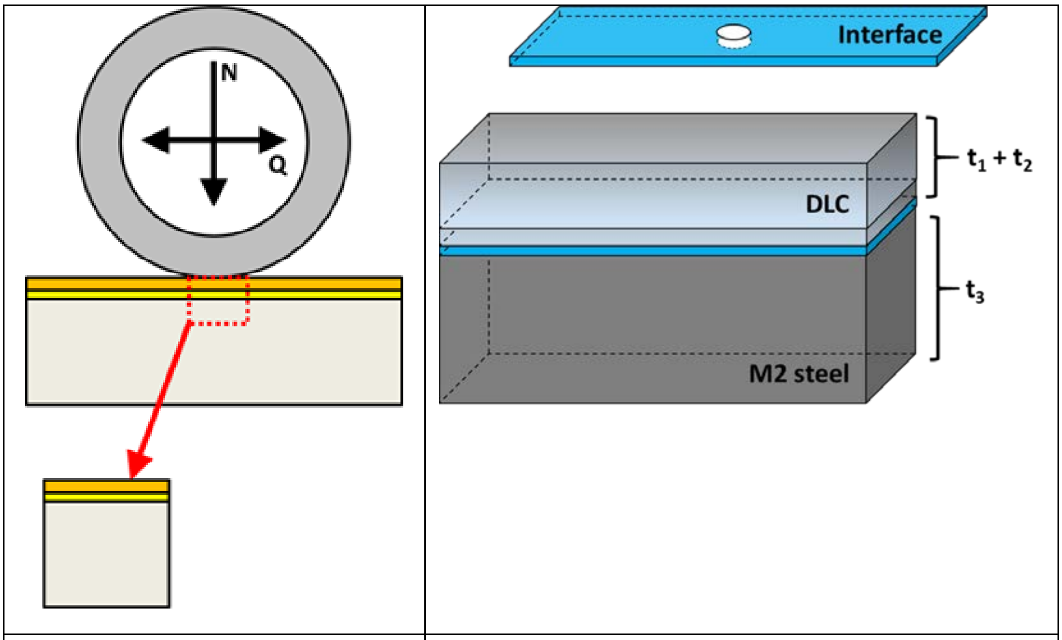

-a- -b-

Figure 7: Extraction of a RVE to study blister forming (a) and schematic illustration of the model (b).

The size of this volume corresponds to the contact area. A volume of 0.31 mm x 0.31 mm x 0.31 mm represents the substrate material. An elasto-plastic behavior is assumed for t the M2 steel (E=210 GPa, v=0.3, σ_y=2100 MPa). On the M2 steel an interface is placed. An initially debonded zone of size D=2R is considered in the center of the interface (figure 7b). The rest of the interface is modeled by a cohesive zone with an interface energy of 60 J/m^2. Finally, a DLC coating layer is considered on the interface. Note, the whole coating was modeled as one layer and the interlayer of WC-WCC presented in the previous chapters is not considered for simplicity purposes. The Young's modulus of the film is given as E=240 GPa and the Poisson's ratio as v=0.2. The coating is supposed elastic. The latter is not true in reality due to the cracks observed experimentally in the blisters borders.

Different DLC film thicknesses, a thin layer (0.2 µm), an intermediate (1.5 µm) and a thick one (2.5 µm) are considered. Furthermore, several values of the radius (R) corresponding to the zone with zero interfacial adhesion. Finally, several horizontal loads (Q) are taken into consideration, varying from 250N to 1000N. These loads are applied at the surface of DLC film, next to the debonded zone.

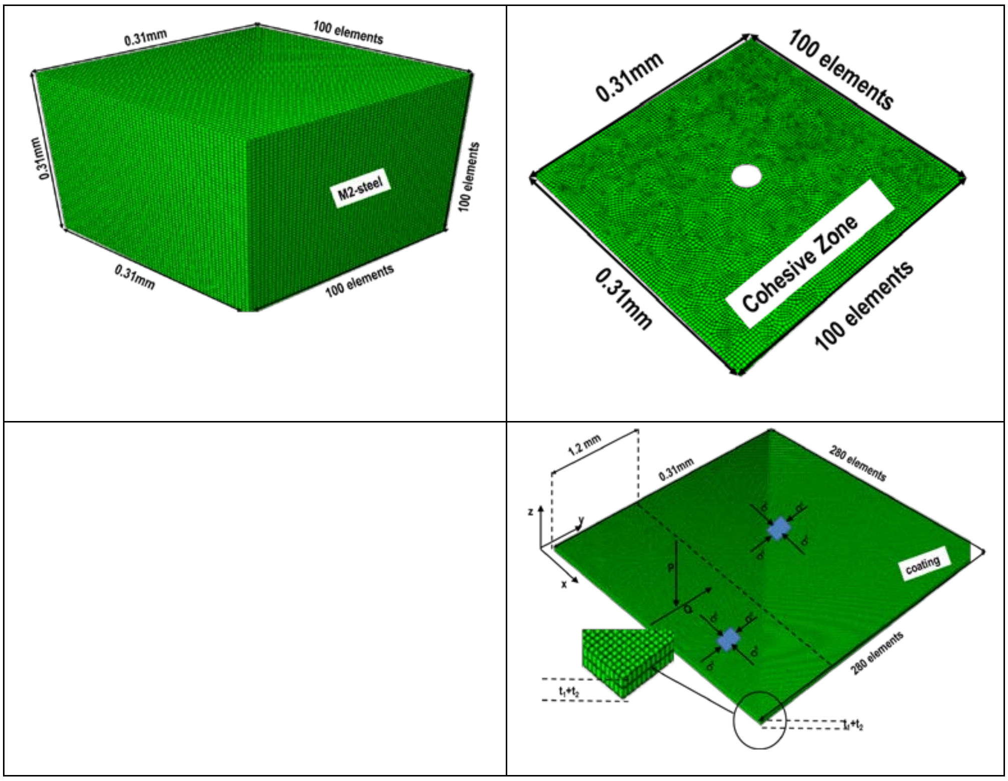

Figure 8: Mesh of the substructures of the model: M2 steel (a), interface (b) and DLC film (c)

4.3.2 Single blister deflection

The stress field and the maximal deflection of the delaminated zone were investigated for the three different thicknesses mentioned before. The stresses before and behind (yellow lines in figure 9) the delaminated zone are analyzed as well as the stress state of the formed blister.

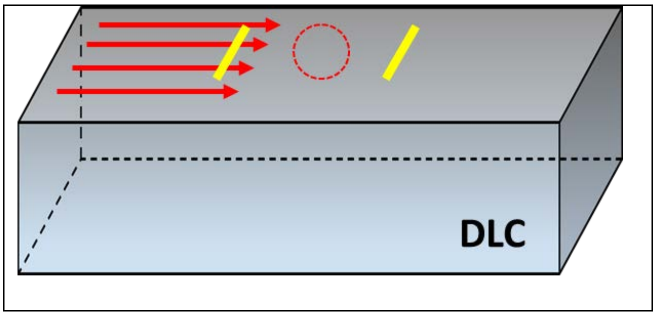

Figure 9: Sites of stress analysis next to the debonded area

4.3.2.1 The thick DLC film

In the case of the 2.5 μm DLC film, several initially delaminated zones are examined varying form D=30 μm to 50 μm. Different friction loads Q are applied as mentioned previously. The normal load is kept constant equal to 1kN.

2R=30 µm

The interest in a debonded zone of 30 µm is motivated by the AFM measured radius of blisters about 32-33 µm. Figure 10 shows the deflection predicted for D=30 µm for all applied tangential loading.

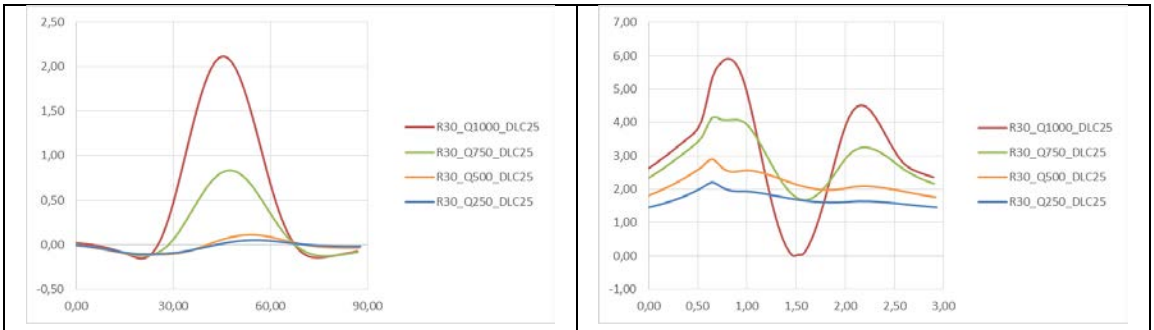

-a- -b-

Figure 10: Predicted deflection of a blister with an initial debonded zone of 30 µm (a) and the stress value parallel to the loading direction (b)

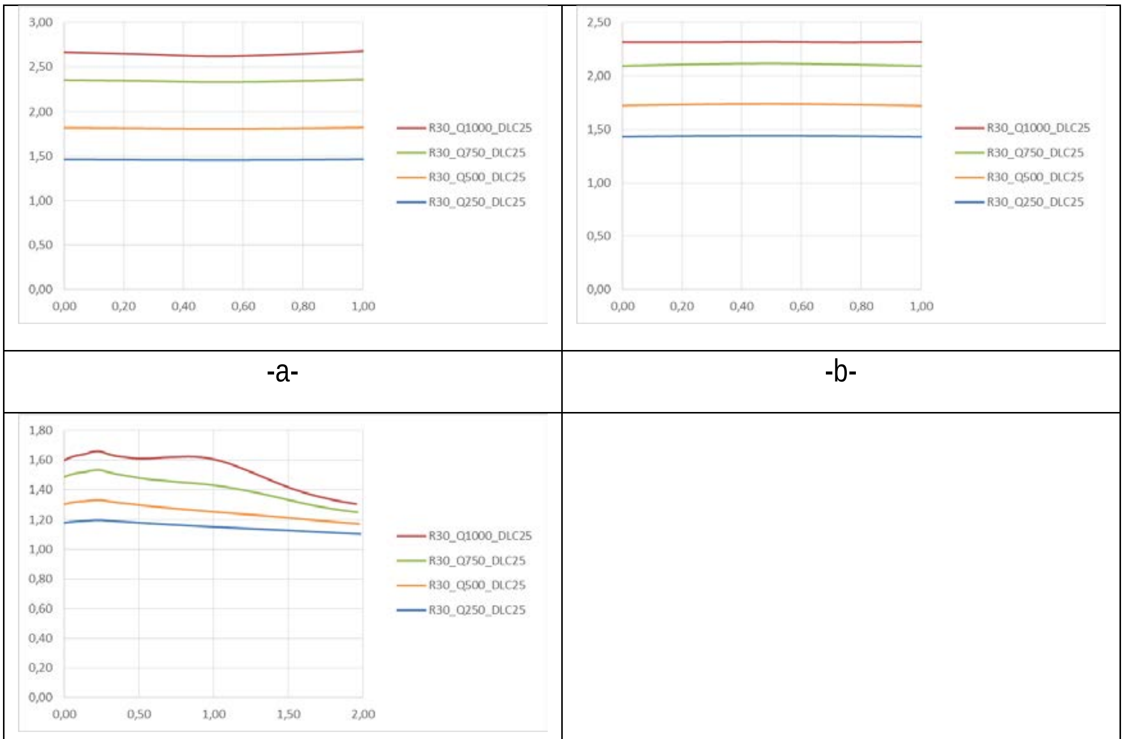

-a- -b-

-c-

Figure 11: Stress distribution before (a), behind (b) and above (c) the delaminated area (40 µm)

For the loads of 250 and 500 N almost no deflection of the film is observed. This results means that in the case that debonded areas are present between the coating and the substrate, they cannot be easily observed experimentally (SEM or AFM) due to their dimensions. The load of 750 N leads to a deflection of 0.8 µm while the highest load to one of 2 µm. Based on the AFM measurements, the first value is slightly low and thus the model underestimates the deflection by 20-30%. On the contrary, the value for the highest load is 40-50% larger than the AFM measured deflection.

Concerning the stress in the blister, it seems that it increases with the rise in the load Q. In the figure 10b, the stress normalized by the residual stress (2 GPa) and the distance is normalized by the blister radius. All stress values presented here are smaller than the critical stress value (12 GPa) for the buckling of a circular plate used in Hutchinson’s model.

Figure 11 depicts the stress before and behind the debonded zone. At a distance 2R from the blister the stress is homogeneous. The stress behind the blister is slightly lower than in the area submitted to friction. However, the stress above the blister, is 30-40% lower than in the other directions. This is a first step to explain blister elongation in the friction direction and closer blister spacing orthogonal to this direction observed experimentally in chapter 3 (SEM picture).

2R=40 µm

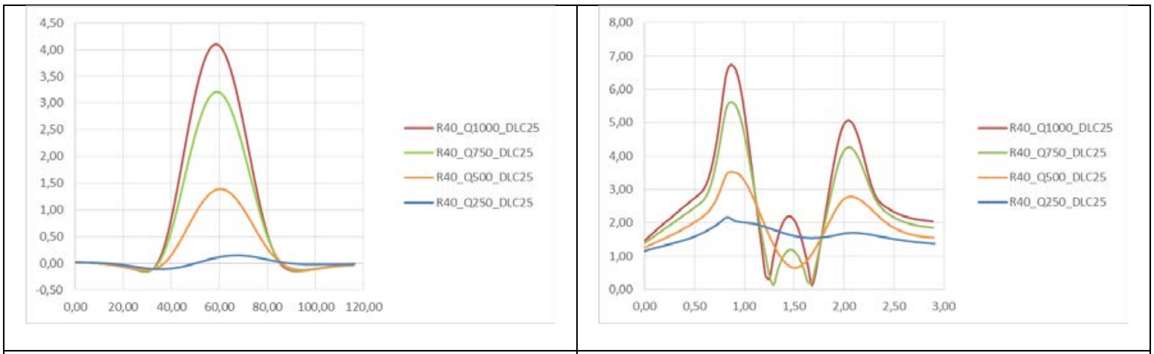

-a- -b-

Figure 12: Predicted deflection of a blister with an initial debonded zone of 40 µm (a) and the stress value parallel to the loading direction (b)

In the case of a larger initial delaminated zone (40 µm), the model overestimates deflection for the loading of 750 and 1000 N and thus these predictions are not realistic. However, for a load of 500 N the maximal deflection is found to be 1.3 µm which is in agreement with the value measured by AFM, even though the radius measured experimentally is slightly lower (32-33 µm). As previously, the 250 N case gives no significant deflection. The stress state is higher than with a 30 µm-blister (especially for the 750 and 1000 N loads) but due to the huge predicted deflection, this cases are considered not realistic.

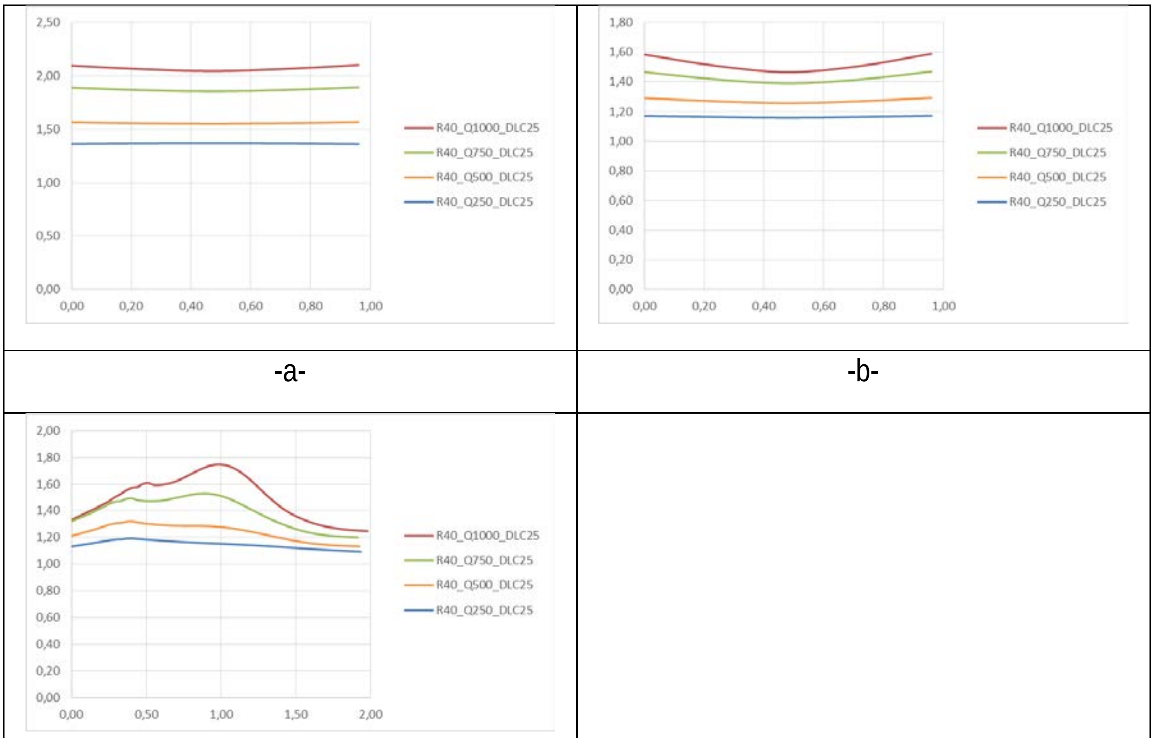

-a-

-b-

-c-

Figure 13: Stress distribution before (a), after (b) and above (c) the delaminated area (40 µm)

The stress field before and behind the “failed” zone is once again homogeneous. A slightly higher stress appears before the blister than behind it as in the case of D=30 µm. However, above the delaminated area (figure 13c), the stress is not that different than in the other sides (13ab). This is definitely a step further in explaining the observed network of blisters in the SEM pictures. Effectively, below a certain blister dimension, the stress distribution exhibits a dissymmetry. Stresses in the friction direction are much larger than in the orthogonal direction. Hence blister nucleation and growth in the friction direction are favored.

2R=50 µm

The last case analyzed for the thick DLC film is the one of a much larger initially delaminated zone.

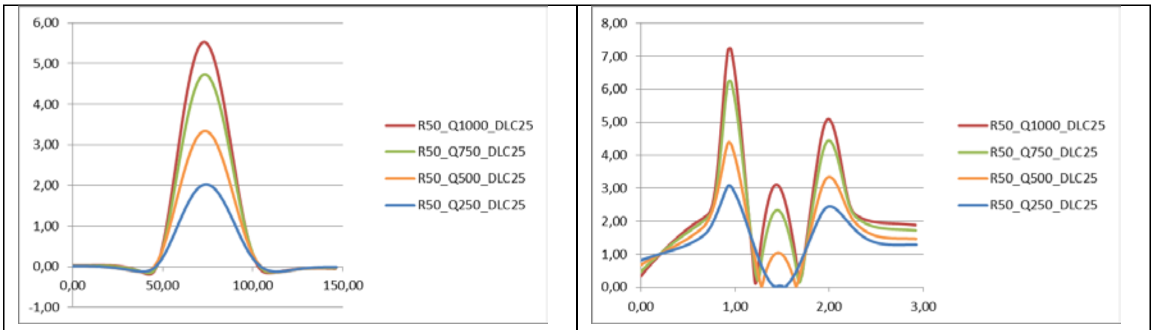

-a-

-b-

Figure 14: Predicted deflection of a blister with an initial debonded zone of 50 µm (a) and the stress value parallel to the loading direction (b)

As shown in figure 14, the loads between 500 and 1000 N cause a deflection higher than 3 µm which is more than 2 times bigger than the measured values. The load of 250 N overestimates too the height of the blister but is kind of more realistic compared to the other loadings. Looking at the stress state in the blister (figure 14b), significant stresses arise from the severe tangential loading Q (i.e. 750, 1000 N).

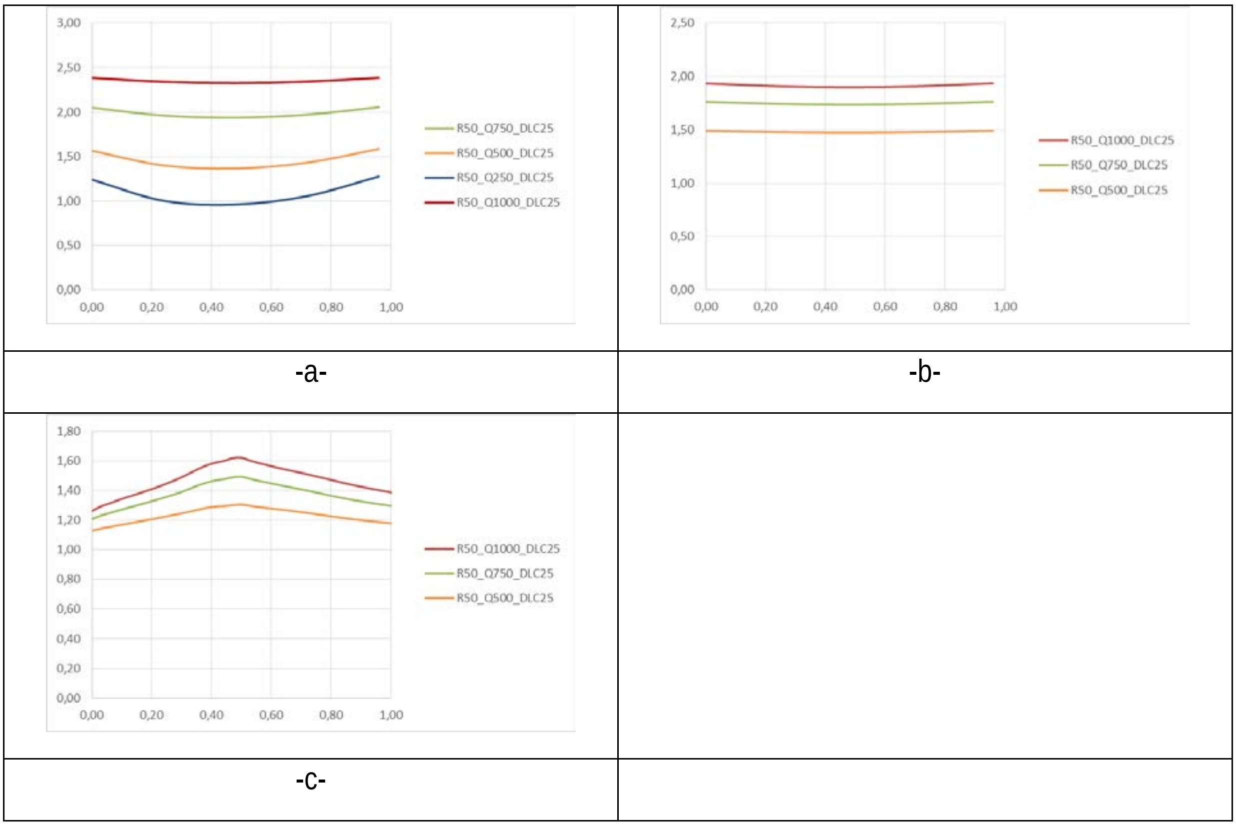

-a-

-b-

-c-

Figure 15: Stress distribution before (a), after (b) and above (c) the delaminated area (50 µm)

Observation of the stresses away from the delaminated area leads to the conclusion that propagation in the vertical direction is different to the horizontal one.

4.3.2.2 The intermediate DLC film

An intermediate thickness DLC film of 1.5 µm was used in this series of simulation. The tangential loads vary from 250 to 1000 N as previously. An initially debonded zone of 30 µm is considered.

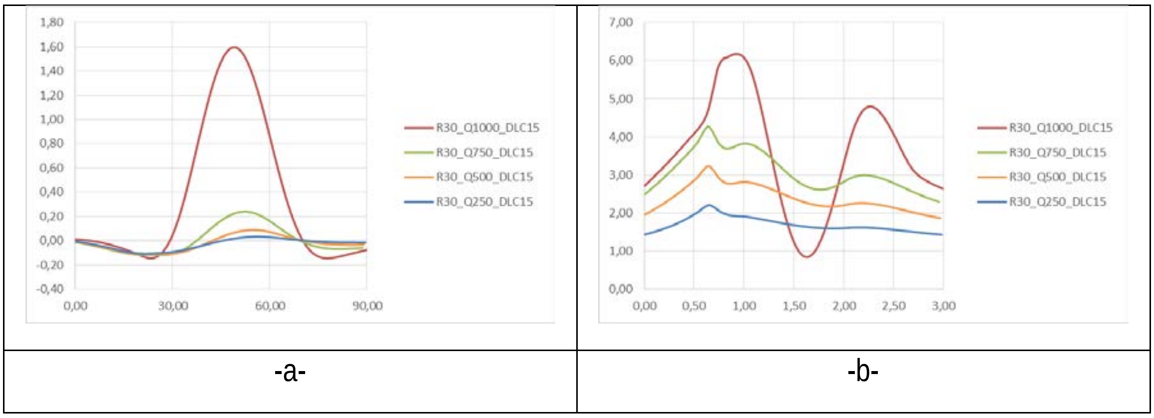

-a- -b-

Figure 16: Predicted deflection of a blister with an initial debonded zone of 30 µm (a) and the stress value parallel to the loading direction (b)

In this consideration, the load of 1000 N results in a maximal deflection of 1.6 µm which is in good agreement with the AFM measurements. However, such an important loading can only be acceptable in the case that, during the tribological/wear test described in chapter 2, the thickness of DLC is reduced and thus, locally, a higher amount of loading is applied to the film. The stress through the blister is more or less similar to the case of the thick DLC coating.

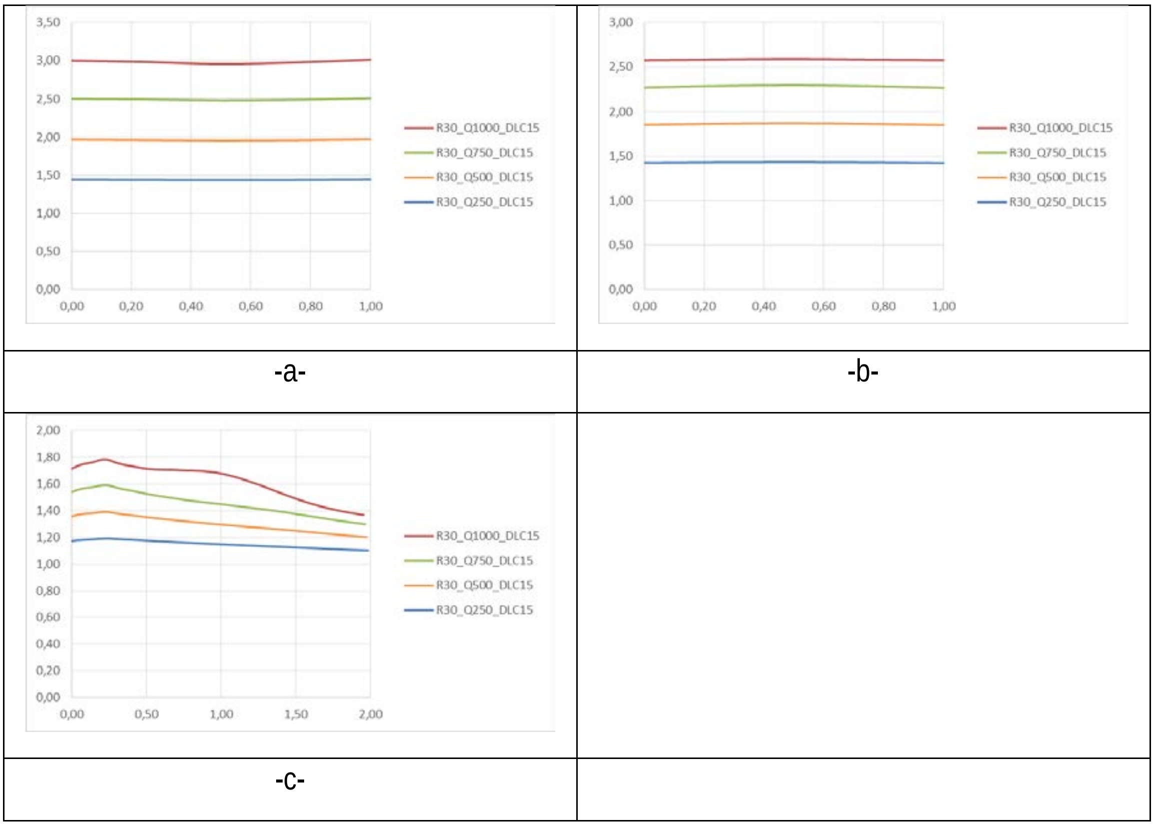

-a- -b-

-c-

Figure 17: Stress distribution before (a), after (b) and above (c) the delaminated area (30 µm)

Stress before the delaminated zone is found once again to be slightly higher than after this area. In addition, stress above this zone is much lower (especially for Q=750 and 1000 N) than in the other sides. The status of the interface should be observed to validate or not the blister propagation hypothesis.

4.3.2.3 The thin DLC film

In order to have a complete image of the DLC blistering phenomenon, a thin DLC layer of 0.2 µm was chosen. The same initial debonded area as previously is considered (30 µm) as well as identical loading cases (Q).

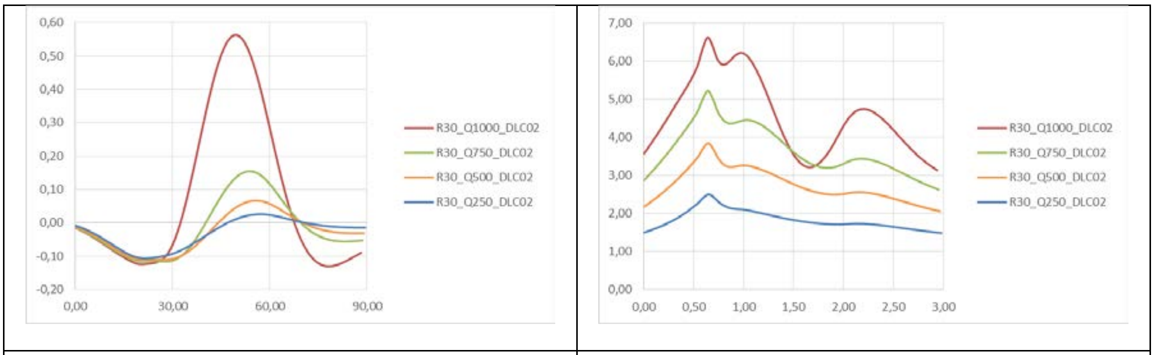

-a- -b-

Figure 18: Predicted deflection of a blister with an initial debonded zone of 30 µm (a) and the stress value parallel to the loading direction (b)

In the case of the thin DLC layer, predictions differ much from the AFM measurements (δ_{mes}=1.7-1.9 µm). Even for the loading case of 1000 N the predicted value is three times lower than the experimental one. Stress through the blister does not vary significantly as in the other thicknesses of DLC. This can be explained by the fact that the deflection is not important to cause an important change in the stress state.

4.3.3 Single blister: debonding

After having analyzed the deflections of the film and the consequent stresses, interface delamination is studied.

4.3.3.1 Interface of the thick DLC coating

2R=30 µm

Figure 19 shows the evolution of the debonding in the interface of a thick DLC coating for a tangential load of 1000 N. The initial interface (figure 19a) is intact and only a circular area in the center presents decohesion as described at the beginning of this section. A small area in front of the blister starts to debond probably due to stress concentration. This zone propagates orthogonal to the applied load Q and through the width of the sample. A small debonded region starts to coalesce with the blister (figure 19def) and finally, behind the blister at approximately a distance of R, a part of the interface loses cohesion (figure 19gh). Ones more, the decohesion behind the blister corresponds to the SEM observations of blisters aligned along the friction direction. Blister growth occurs due to small decohesion in front of the initial debonded region. Secondary blister nucleation corresponds to the debonding behind the existing blister at a certain distance from the latter. Figure 20 presents the interface behavior for a 750 N load.

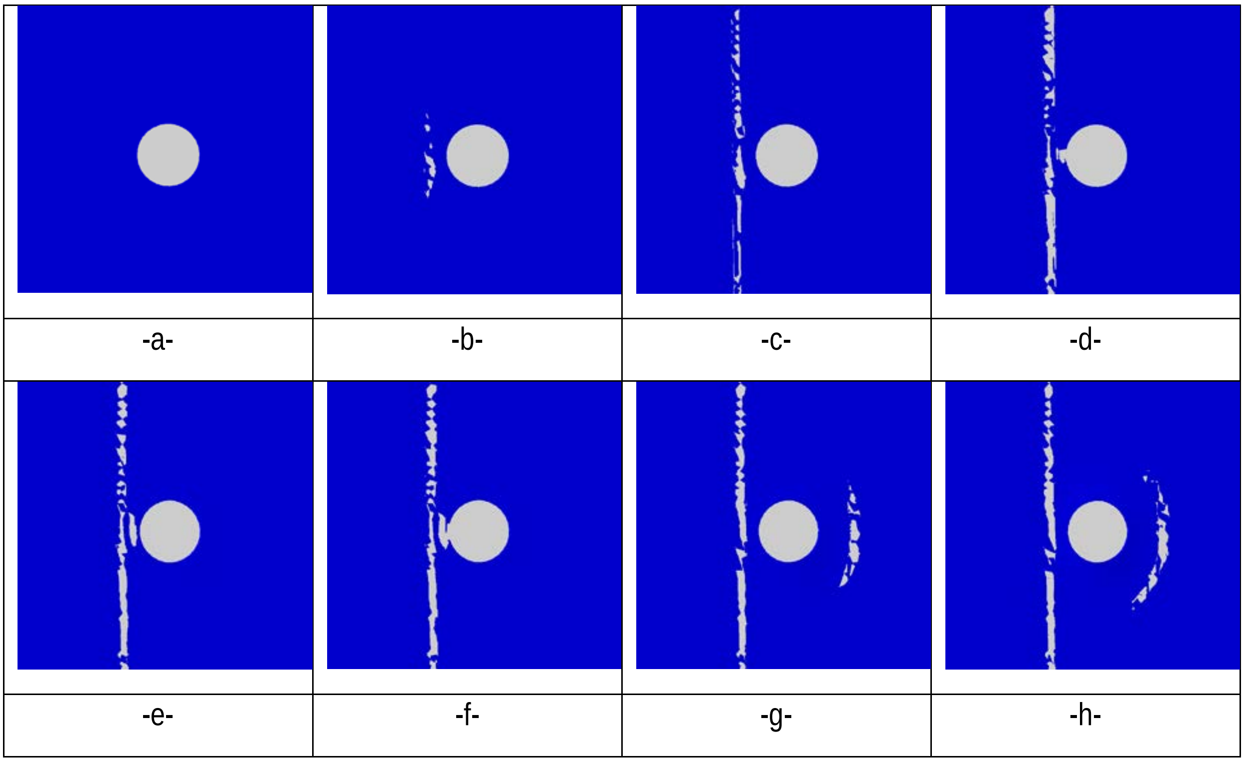
-a- -b- -c- -d-
-e- -f- -g- -h-

Figure 19: Evolution of interface failure in function of the remote loading (DLC 2.5 µm , Q=1000 N). The white area corresponds to complete failure of the corresponding cohesive zone elements.

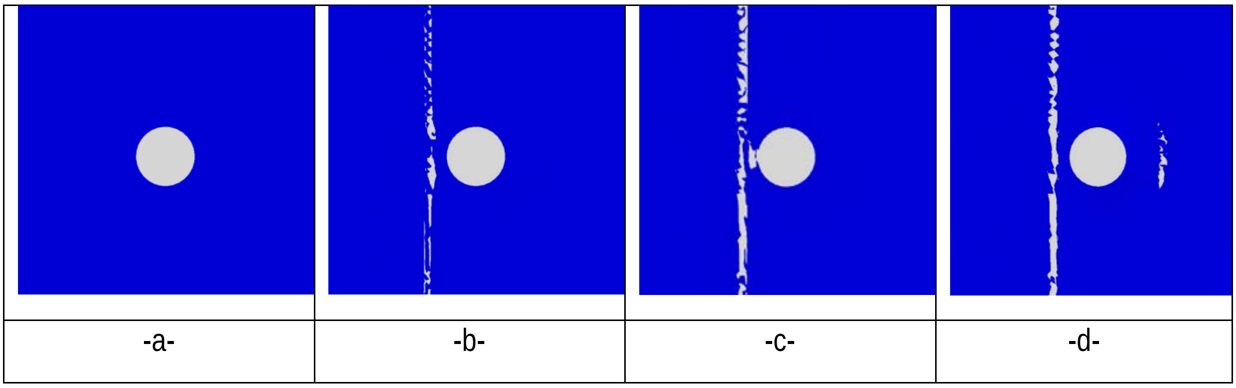
-a- -b- -c- -d-

Figure 20: Evolution of interface failure in function of the remote loading (DLC 2.5 µm , Q=750 N). The white area corresponds to complete failure of the corresponding cohesive zone elements.

A similar behavior to the previous case is observed. However, the delamination behind the blister is more limited, probably due to the lower loading conditions. The loading cases of 250 and 500 N (figure 21) do not cause local decohesion in front of the blister border corresponding to blister growth, neither debonding behind the blister corresponding to blister nucleation. For both loads, a zone is delaminated prior to the blister. On the contrary, there is no delamination behind this feature as found for the more intense loads.

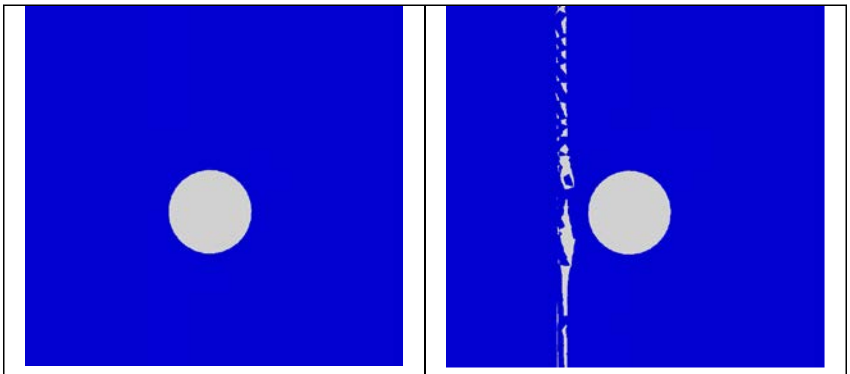

-a- -b-

Figure 21: Interface failure for a loading of 250 N or 500 N

At this stage of the modelling, we could like to draw a partial conclusion. The SEM observations shown in chapter 3 show the existence of a network of blisters (of about 30µm) aligned in the friction direction. The different frictional loads analyzed here show that during low friction, no blister extension neither growth of existing blisters should be observed. The SEM observations also highlight blister formation some tens of µm outside the wear trace. The most probable scenario for blister generation seems to be :

- the existence of zones exhibiting very low surface energy, if not unbonded
- nucleation and blister growth in those zones in front of the wear trace.

In the following sections, we push further the analysis of blister interaction. But, previously, the size effect of the initially debonded zone is analyzed.

2R=40 µm

Lets move to the initial debonded area of 40 µm.

The behavior of the interface in the case of Q=1000 N is illustrated in figure 22. The failure mechanism is identical to the one of 2R=30 µm. But, a much larger area behind the blister is delaminated. The results for the smaller loadings are depicted in figure 23. The load of 750 N results in a similar debonding as the 1000 N one. The load of 500 N leads to a smaller failed are behind the blister while there is no decohesion observed at the right side of the blister in the case of Q=250N.

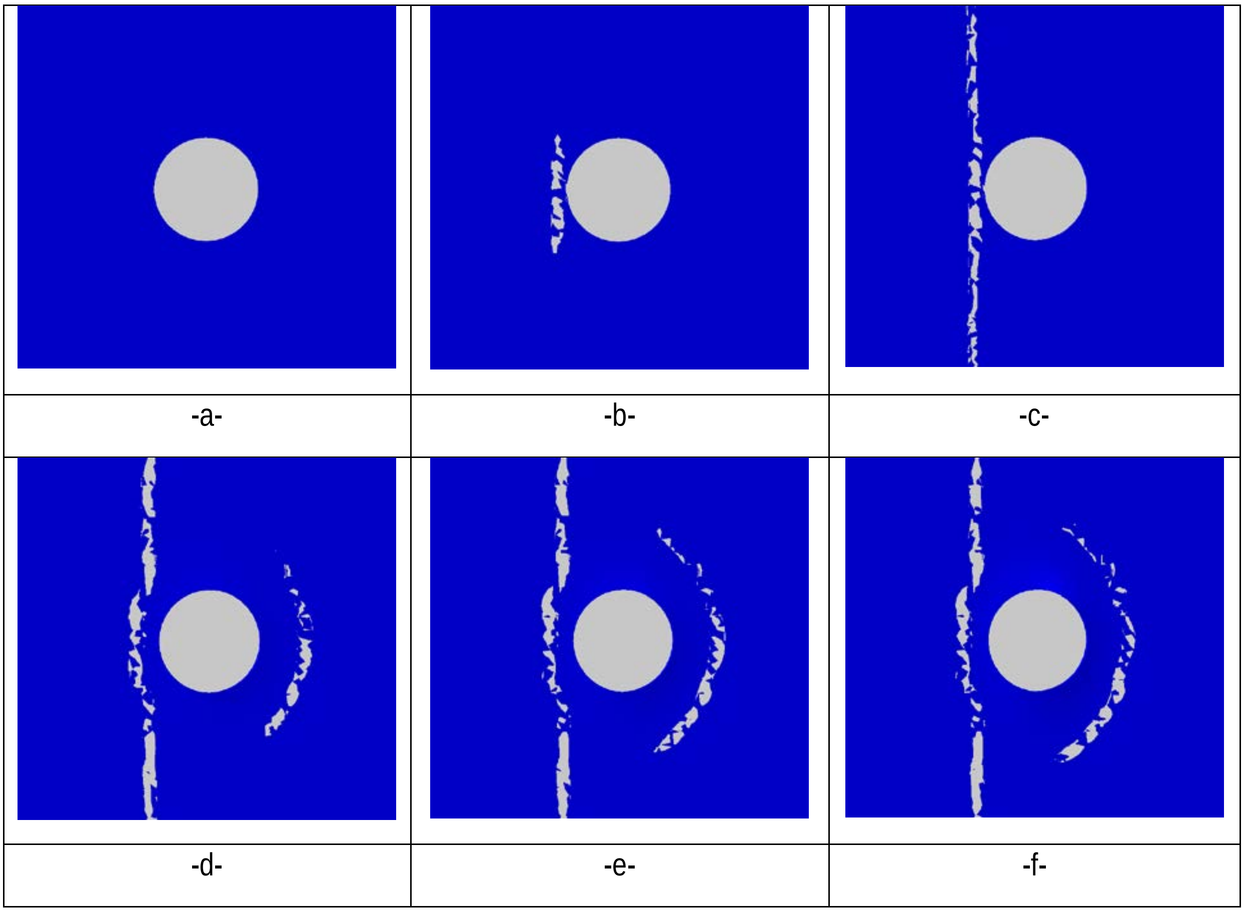
-a- -b- -c-

-d- -e- -f-

Figure 22: Evolution of interface failure in function of the remote loading (DLC 2.5 µm ,2R=40µm, Q=1000 N). The white area corresponds to complete failure of the corresponding cohesive zone elements.

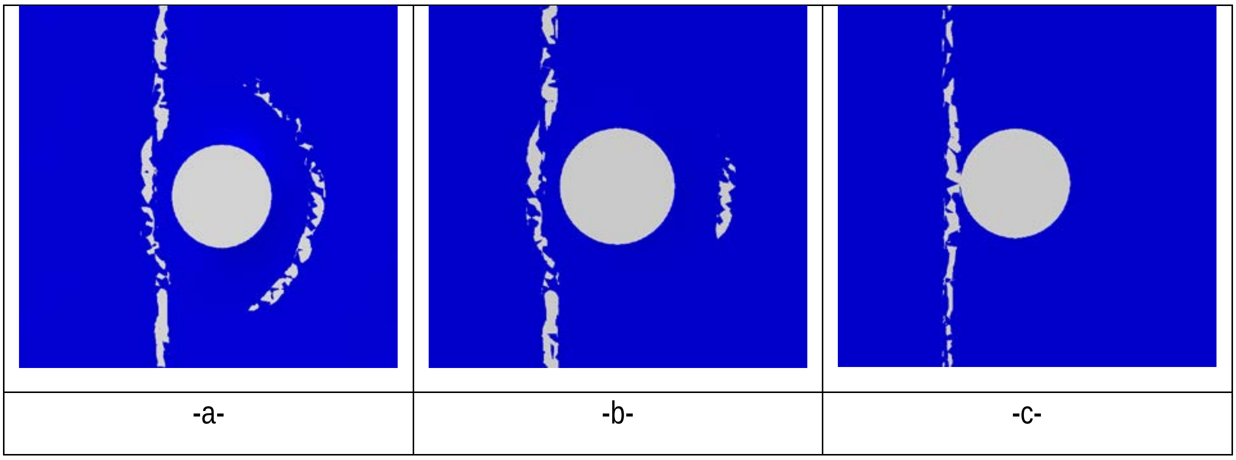
-a- -b- -c-

Figure 23: Failed interface for DLC 2.5 µm , 2R=40µm, Q=750 N (a) , 500 N (b) , 250 N (c) The white area corresponds to complete failure of the corresponding cohesive zone elements.

2R=50 µm

In the case of the larger initial debond, the failure behavior is similar for all loadings. The only difference is the decrease in the failed area behind the blister, with the reduction of the load Q (figure 24a-d).

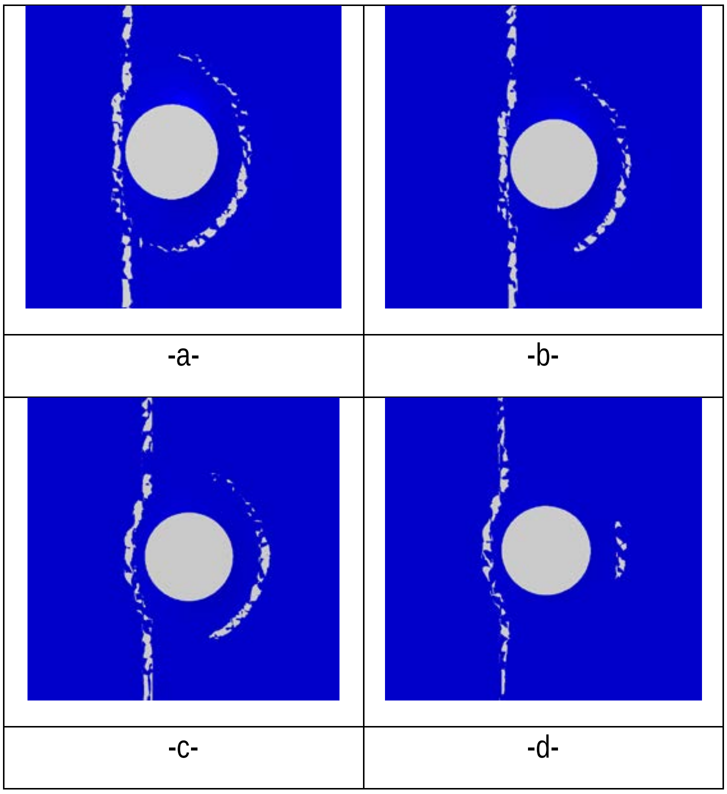

-a- -b-

-c- -d-

Figure 24: Failed interface for DLC 2.5 µm, 2R=40µm, Q=1000 N (a) , 750 N (b) , 500 N (c) , 250 N (d). The white area corresponds to complete failure of the corresponding cohesive zone elements.

4.3.3.2 Interface of the intermediate thickness DLC coating

For the DLC film of 1.5 µm the failure of the interface seems like the case of the thick DLC coating. In this case only 2R=30 µm is considered.

Higher load Q leads to larger debonded zone. The lower loading conditions (Q=250and 500 N) do not result in failure behind the blister (figure 25c,d).

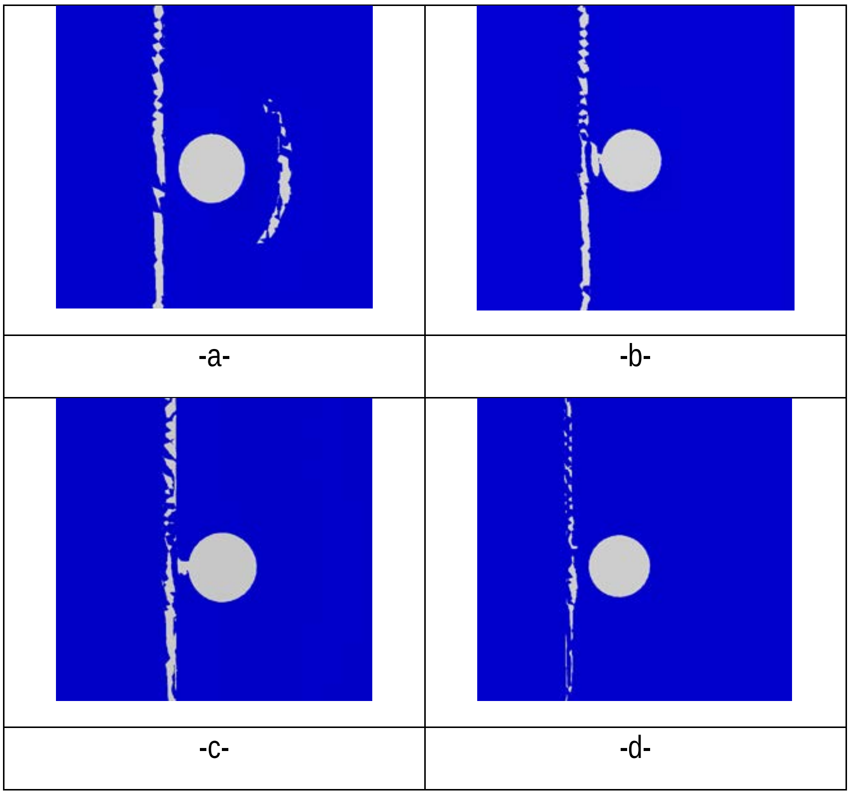

-a- -b-

-c- -d-

Figure 25: Failed interface (in white) for DLC 1.5 µm, 2R=30µm, Q=1000 N (a) , 750 N (b) , 500 N (c) , 250 N (d).

4.3.3.3 Interface of the thin DLC coating

The thin DLC layer of 0.2 µm presents mainly decohesion ahead of the circular debonded area for all loads Q. Once again, only the 2R=30 µm case is taken into consideration.

In all cases a limited interface failure is present at the border of the blister, except for the load of 250 N which is not sufficient to make the blister propagate (figure 26d).

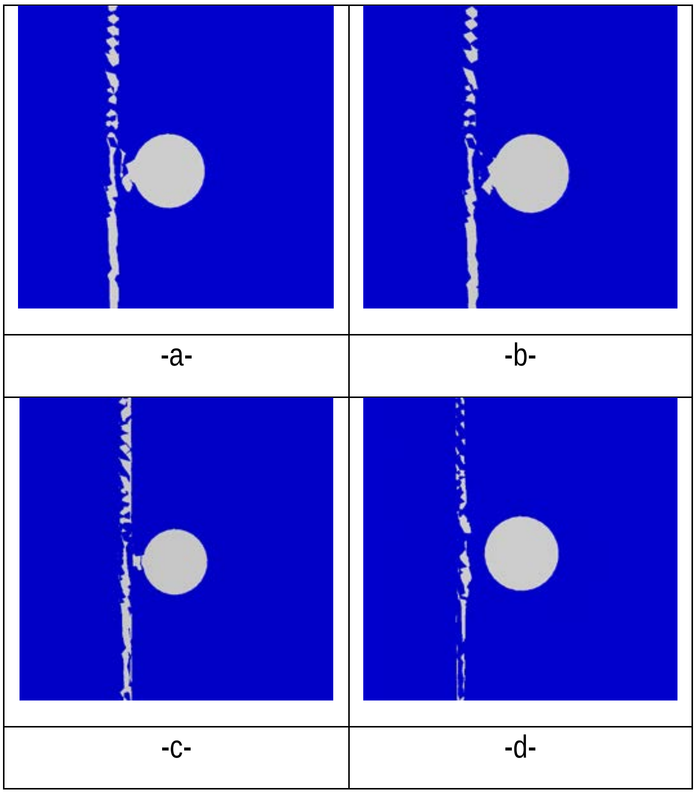
-a- -b- -c- -d-

Figure 26: Failed interface (in white) for DLC 0.2 µm, 2R=30µm, Q=1000 N (a), 750 N (b), 500 N (c), 250 N (d)

Let us summarize the previous analyses. At this stage, the contact area and the consequences of an existing debonded area on the close stress field, the blister height as well as potential debonding of the neighborhood material have been analyzed. The main conclusions from these models are :

- Hertz' elastic contact model :

  No matter what the frictional load, the contact area is mainly controlled by the applied contact pressure. For our configuration, the area affected is about $2*0.3*0.3mm^2$.These results were used to build a finite element model with an initially debonded region.

- The Finite Element simulation with single initially debonded region lead to the following conclusions concerning
  - the stress distribution
    - The stress field at a distance 2R from the debonded region is almost homogeneous
    - The stress ahead of the debonded region is larger than the behind the debonded region
    - The stress on a section parallel to the friction direction is smaller than on an orthogonal section.

The stress distribution clearly favors blister extension in the friction direction.

- ■ blister deflection and radius
  - To reach blister deflections determined by AFM, very high local values of the friction load have to be considered.
  - Blister radii in the same order of magnitude as determined by AFM are obtained.

The high frictional load needed to reproduce AMF-measured blister deflection seems to confirm significant wear, and, hence a locally increased friction coefficient, prior to debonding. This would correspond to blistering observed outside the wear trace.

- ■ debonding observed around a single blister
  - debonding behind the blister in the friction direction is favored.

Hence, once more the tendency to form arrangements aligned in the friction direction is highlighted.

4.3.4 Blister interaction

Modeling the single blister response and deflection reveals basic information about blistering driven delamination. However, in reality, the mechanical problem is much more complex. As explained in chapter 2, the blisters appear in networks (figure 27).

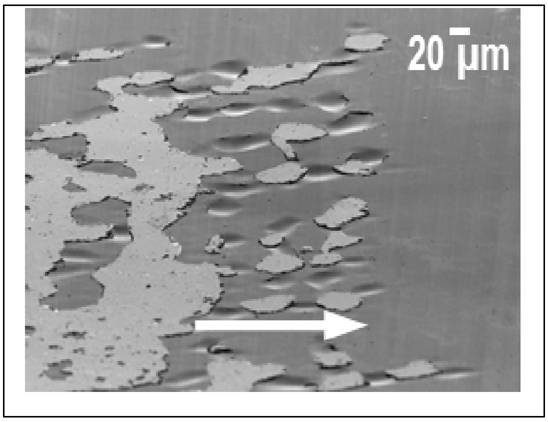

Figure 27: A network of blister next to the wear trace

The white arrow in figure 27 indicates the friction direction. It is consequently probable that these buckled features, in close proximity to each other, interact and thus the delamination problem is somehow more complex. For that reason, the previously presented model was used to describe the behavior of this kind of networks. The only adjustment to the model was the modification of the interface with the initial decohesion.

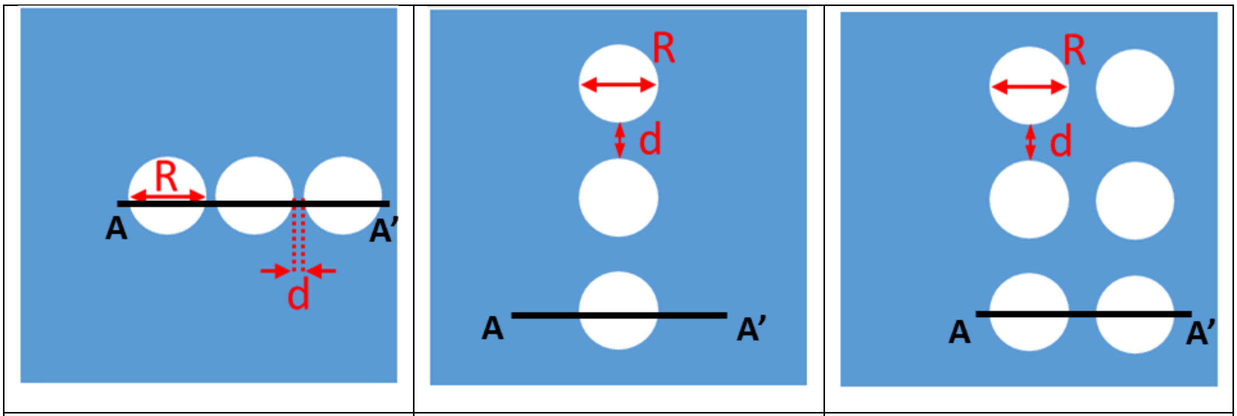

-a- -b- -c-

Figure 28: Series of blister parallel to load Q (a), perpendicular to it (b) and network of blisters (c).

In the current analysis we consider the thickest DLC coating (2.5 µm). Several delaminated zones are tested and a variety of inter-distances (d).Three main cases are investigated. The first one concerns a series of 3 blisters parallel to the friction load Q (figure 28a). The second one considers a series of 3 blisters perpendicular to the load Q (28b). The last one treats the case of a network of 6 blisters aligned in 3 horizontal lines and 2 vertical ones (28c).The black lines A-A' denote the region where the values were examined.

4.3.4.1 Series of blisters aligned horizontally

An initial debonded zone of 2R=40 µm is considered and two different inter-distances (d=1 and 10 µm) were tested. A load Q=1000 N is considered for all simulations.

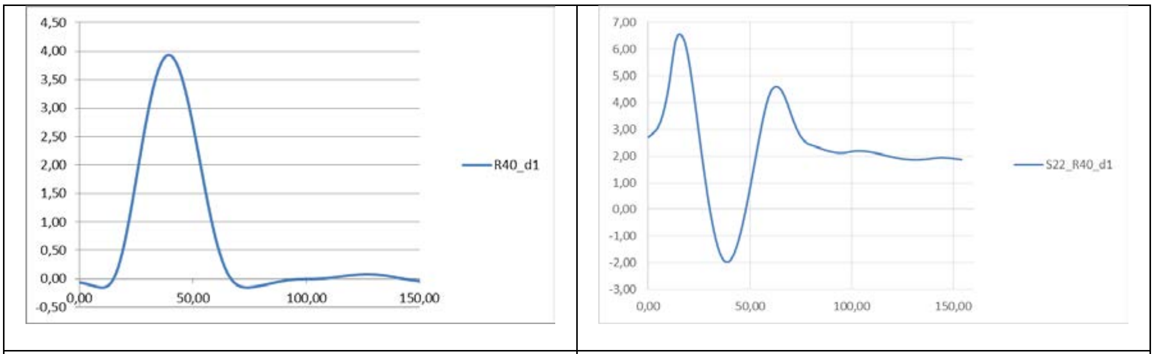

-a- -b-

Figure 29: Displacement of the coating (a) and its stress state (b) for d=1 µm

Figure 29 shows the coating deflection and stress distribution. A plot through the center of the delaminated zone (line AA') shows that only the first blister is clearly formed. On the contrary, no major deflection is accounted for the rest of the zones. In addition, stress in the first blister presents an important increase while only slightly higher than the residual stress elsewhere. Thus very close blisters induce a screening effect on those behind them in the friction direction. Let move on to the case of an inter-distance d=10 µm, in order to analyze its influence on blisters' buckling.

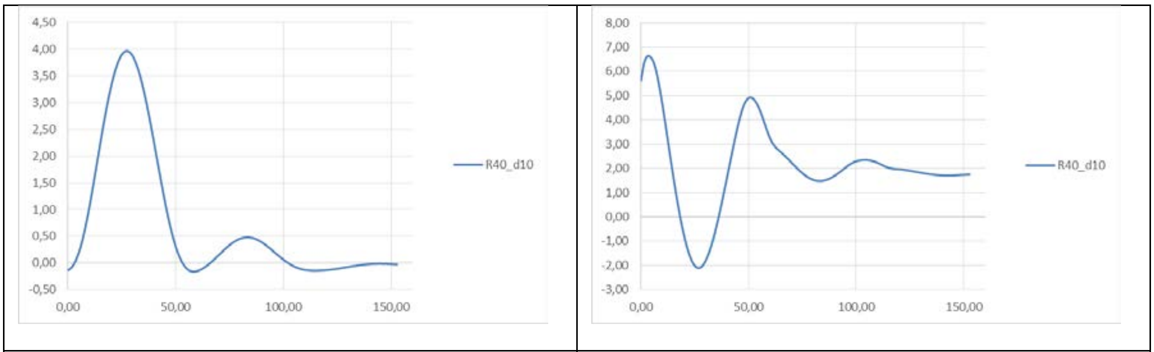

-a- -b-

Figure 30: Displacement of the coating (a) and its stress state (b) for d=10 µm

The first blister presents a deflection of 4 µm as in the previous case. On the contrary, in the case of d=10 µm the second zone seems to buckle slightly. The screening around a blister is limited to a range much smaller than the blister radius. Nevertheless, the value of its deflection is not important.

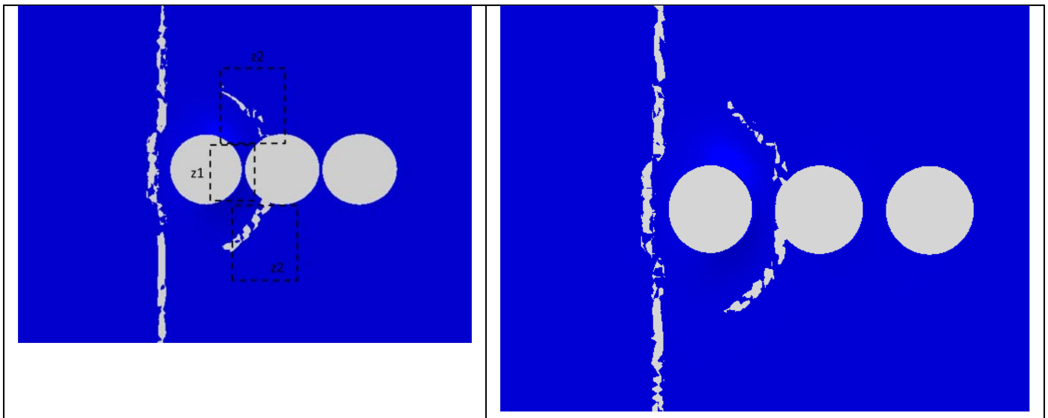

-a- -b-

Figure 31: Interface failure for d=1 µm (a) and d=10 µm (b)

Observing the two failed interfaces, one can note that delamination takes place at the same place for both cases. Thus, an influence of the inter-distance is not found. But a huge difference with a single blister is shown. A single blister leads to delamination ahead and behind it. Here, the delamination starts at the second blister. Clearly, the first blister leads to screening inside zone 1. On the other hand, the stress increase (modelled previously) caused by the front blister leads to a higher "remote" stress applied to the second blister and hence possible debonding in zones 2. As for the 3rd blister, the debonded zones of the two other blisters lead to severe screening and a much smaller "remote" stress.

4.3.4.2 Series of blisters aligned orthogonal to the friction direction

In this part of modeling, a series of 3 debonded zones is aligned on a line orthogonal to the friction direction. Several inter-distances varying from 1 to 20µm are considered. A size of 2R=50 µm is chosen as well as a load Q=1000 N for all simulations.

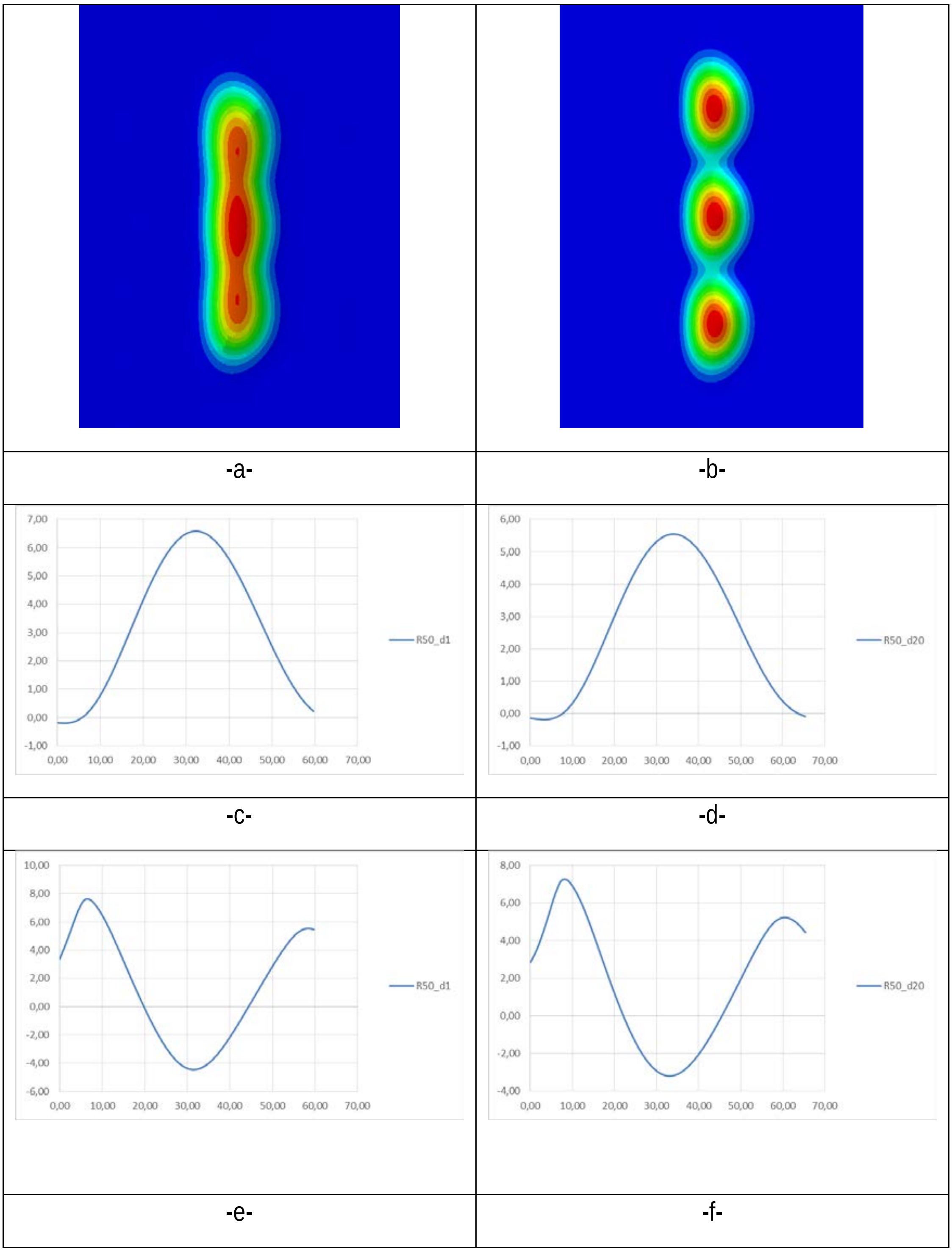

-a- -b-

-c- -d-

-e- -f-

Figure 32: Displacement and stresses in the blister for an inter-distance of 1 µm (a, c, e) and 20 µm (b, d, f).

Prior of analyzing the results, it seems even from the graphical representation (figure 32a,b) that blister proximity in this case plays a role on the behavior of the film. An inter-distance of 1 µm makes the film buckle more and presents a maximal deflection of 7 µm while the larger interdistance (20 µm) leads to a deflection of 6 µm. Note, for all three blister of each case, the maximal deflection is the same. Both cases, present similar stress states and distribution. Perhaps, the smaller inter-distance zone is slightly more loaded but the difference is not significant.

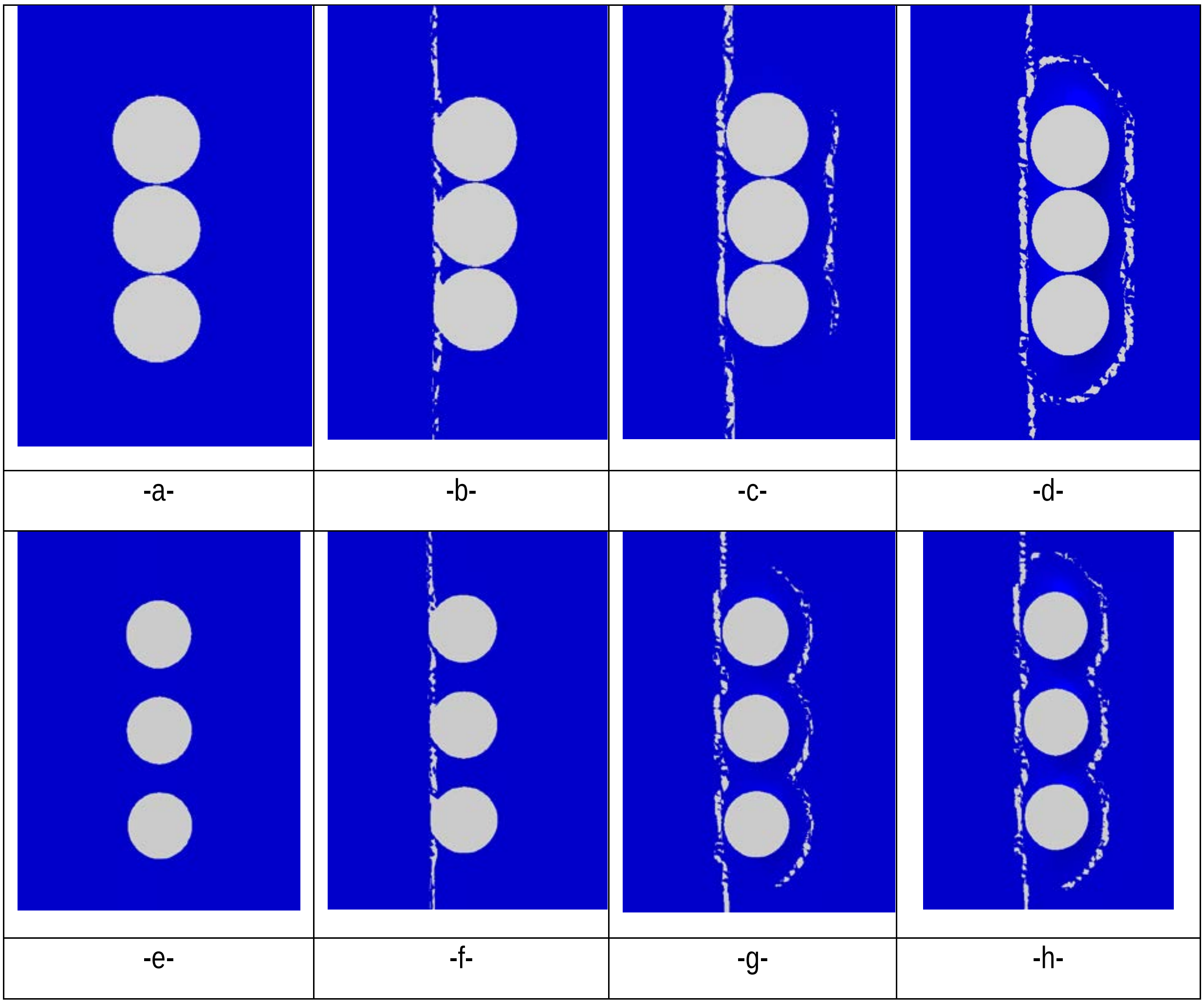
-a- -b- -c- -d-

-e- -f- -g- -h-

Figure 33: Evolution of interface failure (in white) for a blister inter-distance of 1 µm (a-d) and 20 µm (e-h) as a function of the remote loading.

The damage initiation is the same for both cases. It starts in front of the blister and propagates perpendicular to the loading direction. However, failure tends to penetrate between the blisters for the higher inter-distance (figure 33g,h).

4.3.4.3 Network of blisters

For better understanding the influence of neighboring, a network of 6 blisters is modeled. All of them have an initial delaminated zone of 2R=50 µm and an inter-distance of 20 µm in both directions. A tangential load Q=1000N is applied.

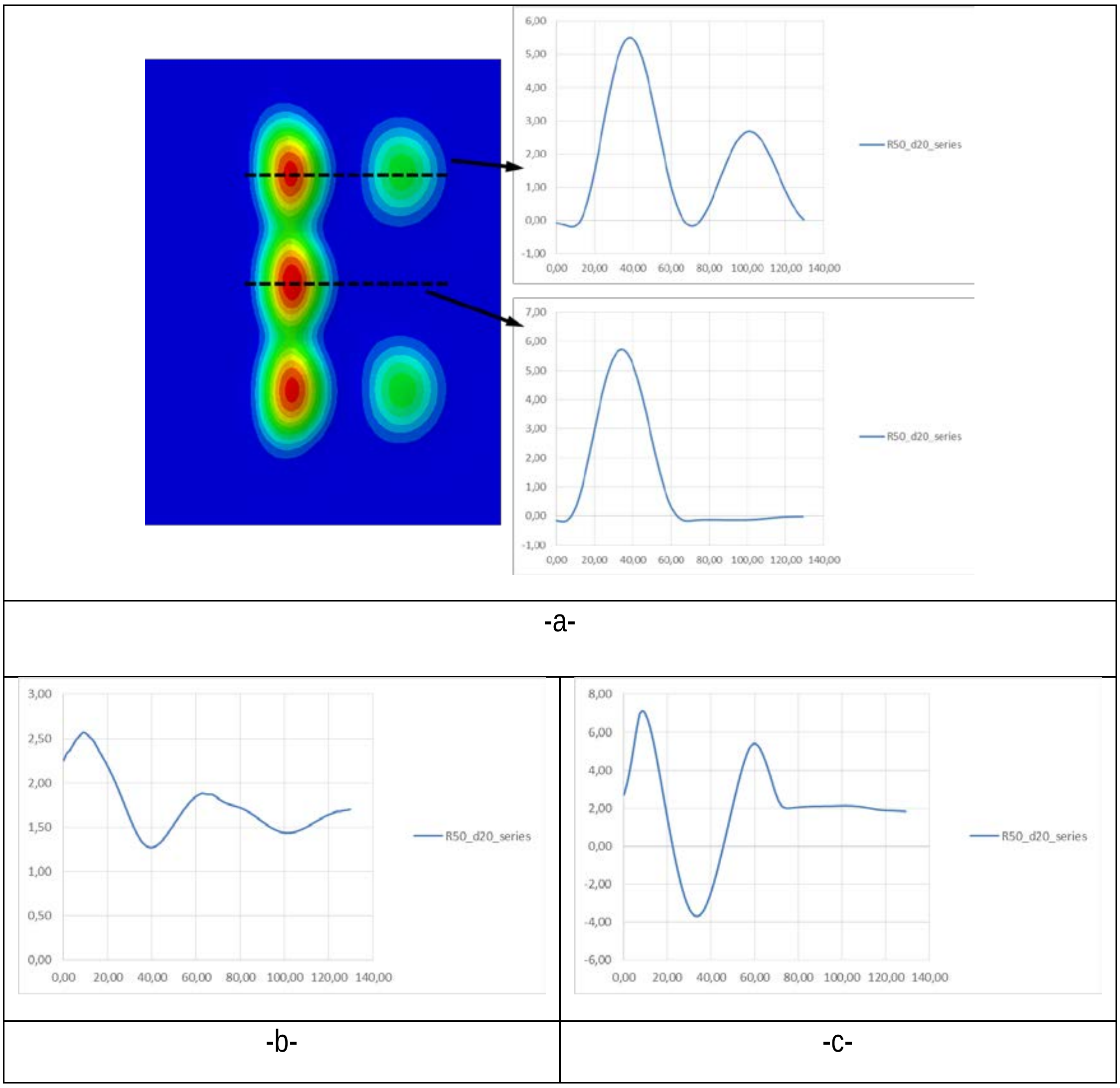

-a-

-b-

-c-

Figure 34: Displacement (a) and stresses (b,c) in a network of blisters

The upper series of two blisters presents a deflection of 5.5 µm for the first one and 2.7 µm for the other. The median series of blisters, however, does not deflect in the same way. Only the first blister buckles away from the substrate while the second one remains plane. Thus, a screening effect is observed.

4.4 Blister nucleation

Experimental observations (chapter 3), revealed crack in the M2 steel substrate. Effectively, a thin layer of iron-rich material (200-300 nm) was attached to the DLC coating after delamination as revealed by FIB milling (figure 35).

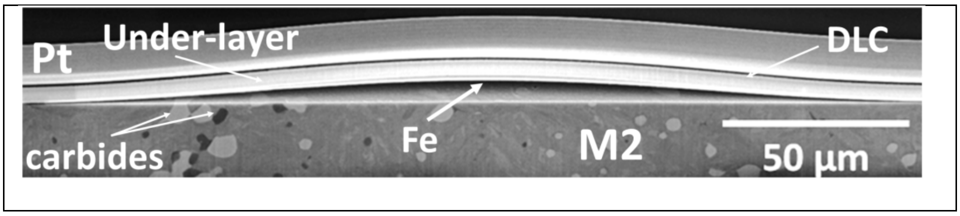

Figure 35: FIB milled cross-section revealing damage initiation in the M2 steel

Delamination inside the M2-steel is now addressed. The finite element model is similar to the ones developed earlier. But, a cohesive zone some nm inside the M2-steel is considered.

4.4.1 Finite element model characteristics

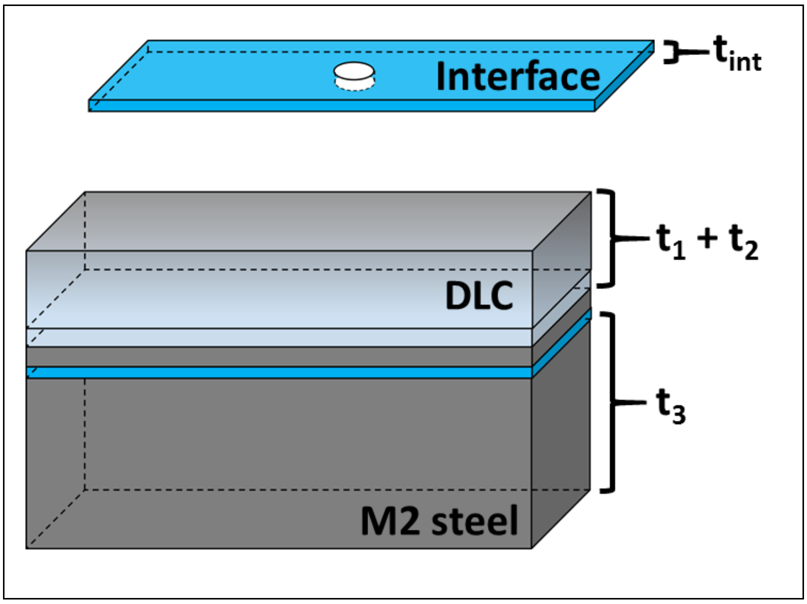

Figure 36: Schematic illustration of the model

As for the previous model, the size of the M2 steel part is 0.31 mm x 0.31 mm x 0.31 mm. This part is assumed as elasto-plastic with a Young's modulus E=210 GPa, a Poisson's coefficient v=0.3 and a yield stress σ_y= 2100 MPa. Only very small strain hardening is assumed to stabilize the numerical schemes. Above the M2 steel part a cohesive zone with properties similar to the previous CZ is placed. Above the interface, a 300 nm thick layer of M2 steel (0.31 mm x 0.31 mm) is assumed. Finally, a coating is put on this thin layer of steel. Two extreme values of DLC thickness (0.2 µm and 2.5 µm) were studies as well as one intermediate (1.5 µm). The coating is modeled as elastic with Young's modulus E=240 GPa and Poisson's ratio v=0.3. The coating is considered homogeneous, with the interlayer having the same mechanical properties as the DLC. Of course, the residual stress quantified experimentally (chapter 3), is applied to the DLC layer. Identical mesh size is in the previous model is used. But, the thin layer of M2 steel is meshed with C3D8 elements of 15 nm. Different tangential loads Q varying from 250 to 1000 N were used as in the previous model. Only an initial bedonded zone of 2R=30 µm is considered for all DLC thicknesses.

4.4.2 Deflection and stress state at the single blister region

4.4.2.1 The thick DLC coating

Comparison with previous models

A 2.5 µm DLC layer submitted to several loads (Q) is considered. Stresses and displacement in the blister and at some distance away (2R) ahead and behind the blister will be examined.

Figure 37a shows the film deflection for a normal load of 1kN and several frictional loads. The film deflection predicted for the case of Q=1000 N is slightly overestimated in comparison to the AFM measured value (1.3 µm). However, “debonding” inside the steel substrate leads to values much closer to the AFM measurements than the previous model (Figure 37b). Note, the final radius of the blister does not change notably between both assumptions.

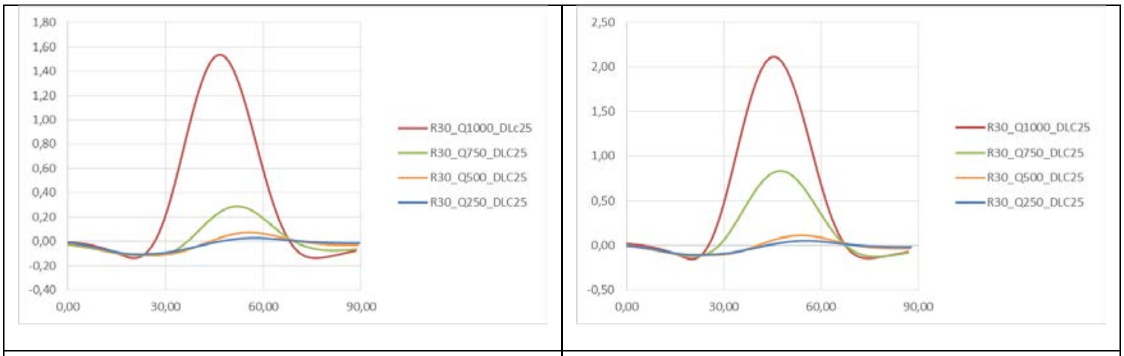

-a- - b-

Figure 37: Predicted deflection of a blister with an initial debonded zone of 30 µm (a) deflection 300nm inside the M2-steel, (b) previous model with deflection at the DLC interface.

Figure 38 shows the stress distribution in the DLC through the blistered region. Figure 38a corresponds to present model, while figure 38b reminds the predictions of previous model. Clearly, assuming “debonding” some nm inside the M2-steel leads to a significant decrease of the maximum stress in the DLC. But the area affected by the overstress is the same in both models. Thus, blister nucleation inside the M2-steel should lead to a slightly smoother stress distribution without affecting the “remote” values at a distance 2R from the blister border. This will be analyzed in the following figure.

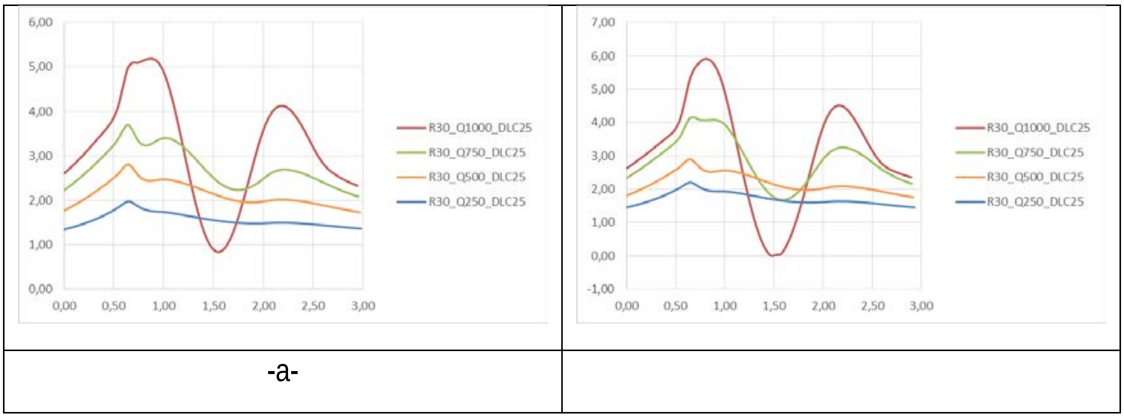

-a-

Figure 38: stress value parallel to the loading direction (a) for “debonding” inside the M2 steel and (b) corresponding to previous model with debonding at the DLC interface.

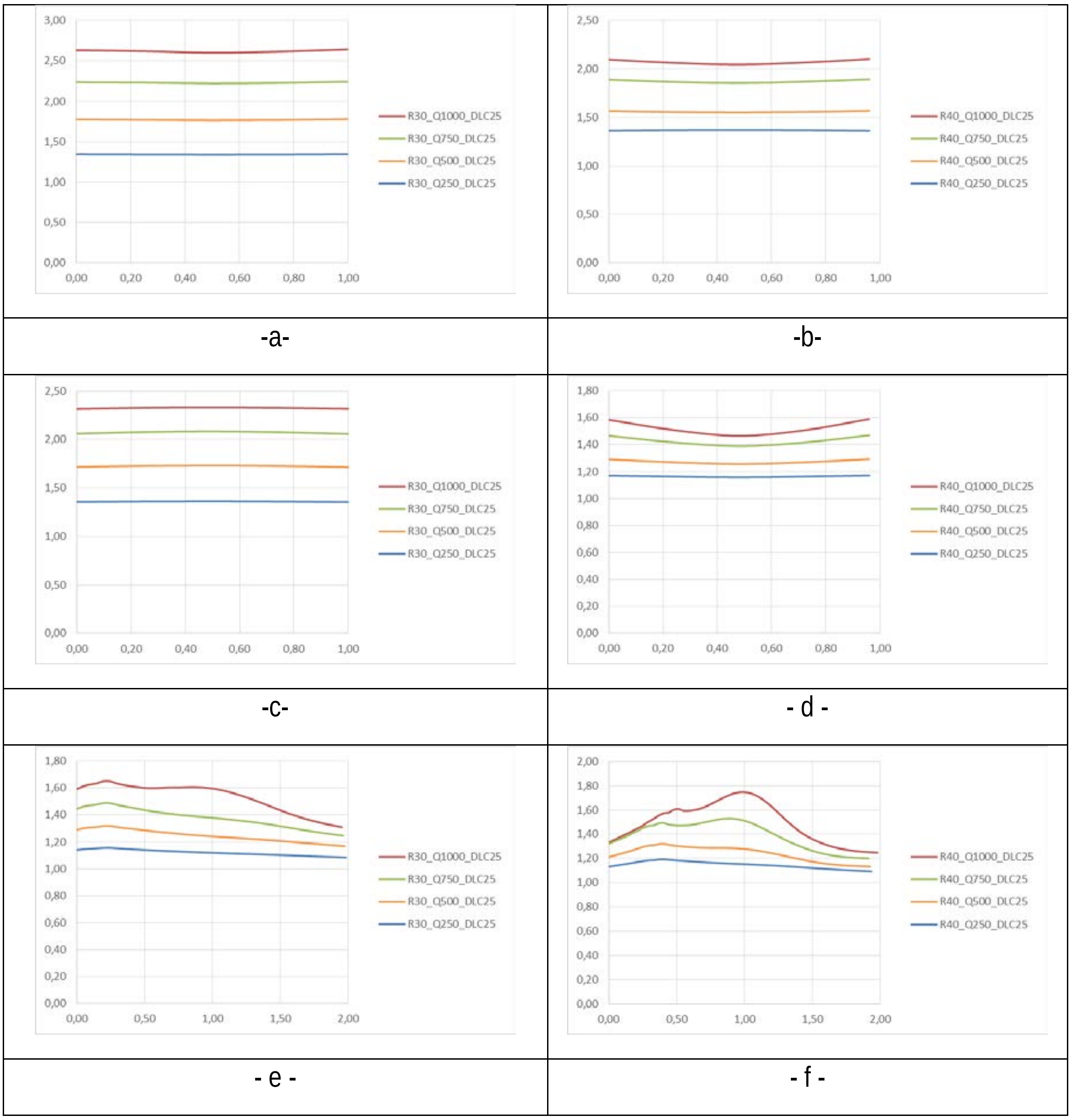

-a- -b-

-c- - d -

- e - - f -

Figure 39: Stress distribution ahead (a), behind (b) and above (c) the delaminated area (30 µm).

Figure 39 shows the stress distribution in the DLC at a distance 2R from the delaminated area. As expected the stresses are homogeneous and in the same range as for the previous model. But, the higher symmetry between the stress ahead and behind the debonded region is noteworthy. Even more significant is the decrease of the stress on a horizontal cut. Thus, even more than with previous model, blister extension in the friction direction seems favored. At this point, blister nucleation inside the M2 steel seems to account for the observed experimental mechanisms. To push the model further, we analyze the strain distribution in the small M2 steel layer.

Strain distribution in the M2-steel

Figure 40 shows the stack-up used in present model. The combination of the applied loading and the presence of an unbonded region in the M2-steel layer leads to severe plastic deformation in the steel.

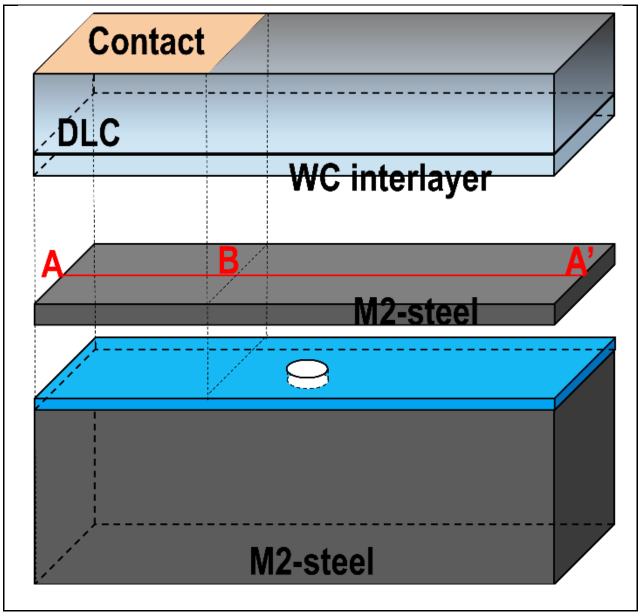

Figure 40: stack-up with location of strain analysis line AA'.

The following figures depict the equivalent strain along line AA'. For every applied load, severe yielding of the steel may be observed in the contact zone. All shear loads lead to yielding in the zone submitted to the contact load (marked AB) on the figures. The absolute value of the equivalent strain may be questioned due to the very small strain hardening coefficient (0.001) considered in present model. Nevertheless, the presence of a “debonded” zone leads to significant yielding in the M2-steel while in the previous model, the M2-steel was completely elastic. The higher loads lead to significant yielding in the area above the debonded zone.

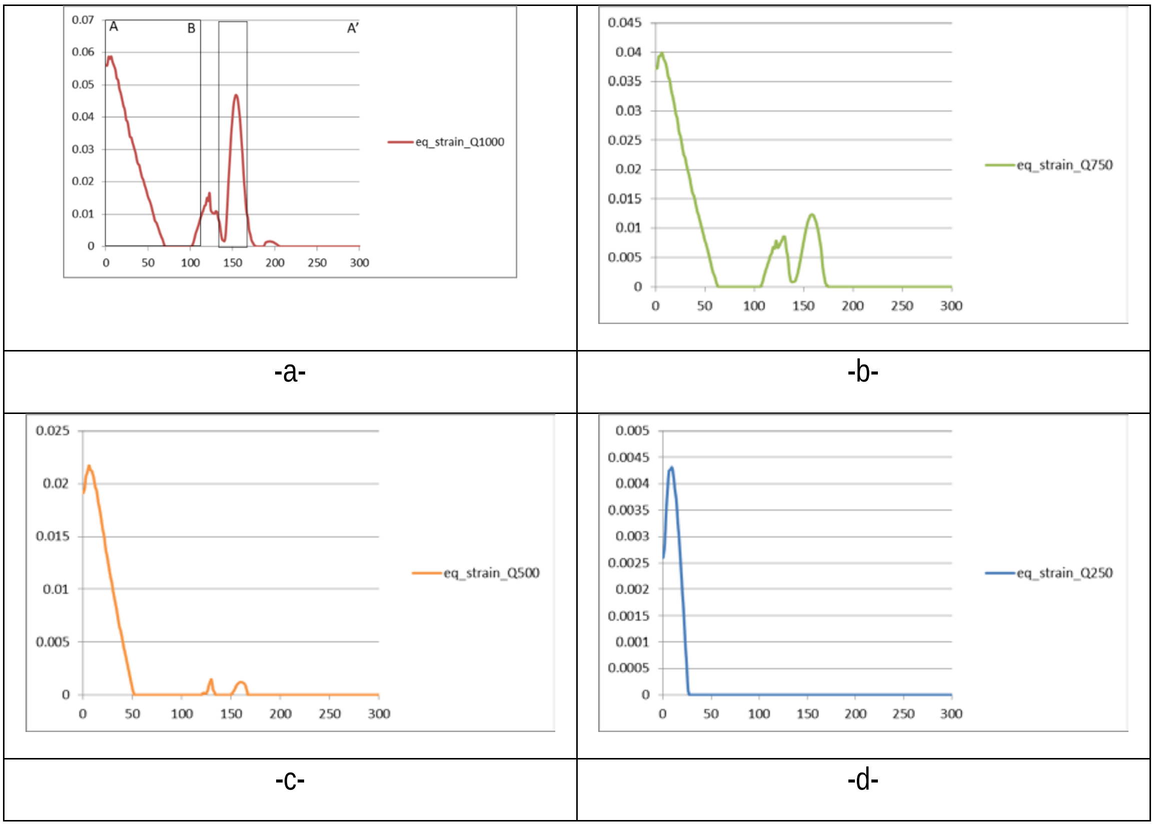

Figure 41: Plastic equivalent strain in the thin M2 layer for DLC 2.5 µm and several loads Q

Figure 41 presents the equivalent plastic strain calculated by the model for a tangential load Q between 250 and 1000 N. In all load cases, the influence of the boundary conditions of the part is apparent at the first part of the plot (0-50 µm). For the highest load (41a), plastic strain up to 4.7% is noted at the delaminated zone (135-165 µm). This strain is more important than the failure strain of the material. Ahead of this zone, the thin layer of M2 steel yields up to 1.7%. Similarly, the second loading case shows plastic strain up to 1.25% ahead and through the failed zone. On the contrary, the lower loading cases present limited (0.15% -figure 41c) or no yielding (41d).

4.4.2.2 The intermediate DLC coating

Coating : deflection and stress distribution

The same analysis was done on DLC coating with intermediate thickness. Several loads Q were applied and an initially debonded zone of 2R=30 µm was supposed. In the cases of Q=750 and 1000N the model overestimates the maximal deflection and does not give realistic values. On the contrary, the prediction for the load of 500N is close to the experimentally measured value (1.4 µm). The lowest loading case does not predict important film deflection.

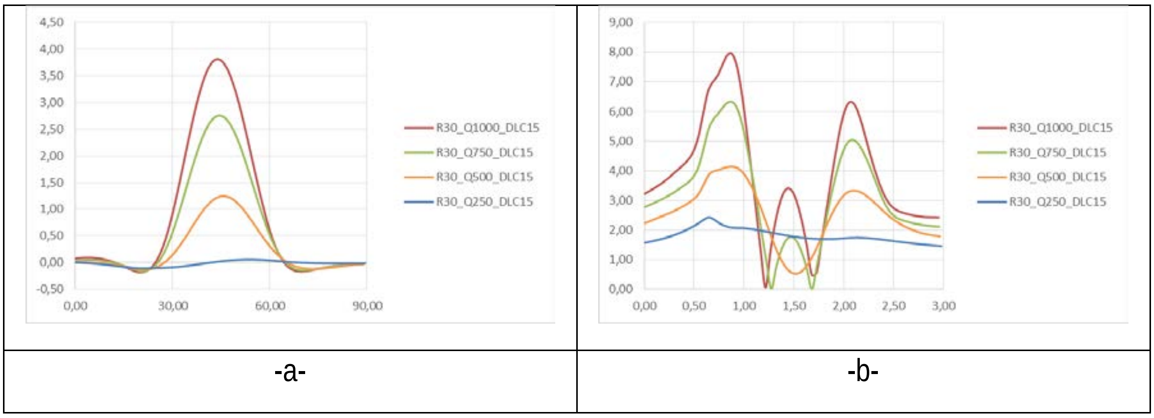

-a- -b-

Figure 42: Predicted deflection of a blister with an initial debonded zone of 30 µm (a) and the stress value parallel to the loading direction (b)

Figure 43 shows the stress predicted. The two highest shear loads predict stress beyond the material limits. Meaning. Hence, these values are only a rough indication, considering the DLC already damaged. Note, in this model, the coating was modeled as elastic film without accounting for possible failure.

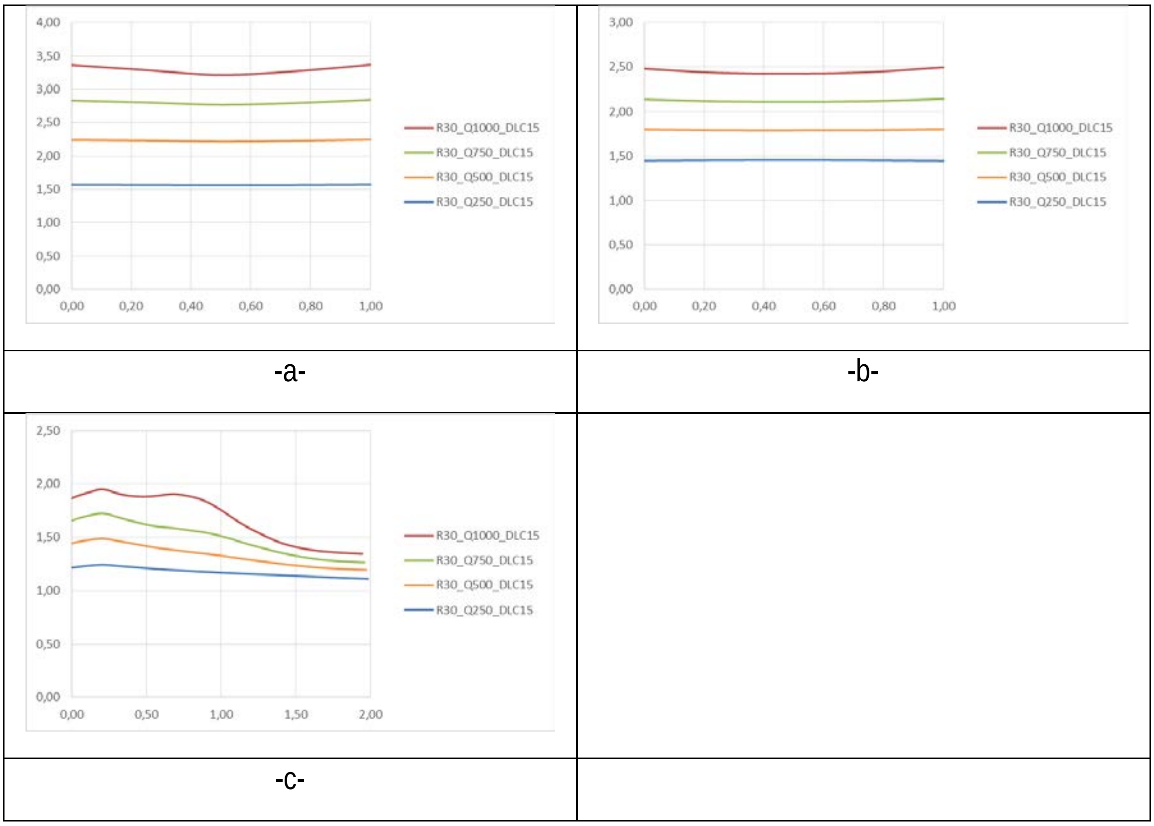

-a- -b-

-c-

Figure 43: Stress distribution ahead (a), behind (b) and above (c) the delaminated area (30 µm).

The stress value ahead of the blister (43a) for Q=1000 N is larger than the value predicted for the thick coating. A slight decrease is observed behind the blister for all loading cases. Once again, the stress above the blister is lower than the other sides.

M2-steel : yielding

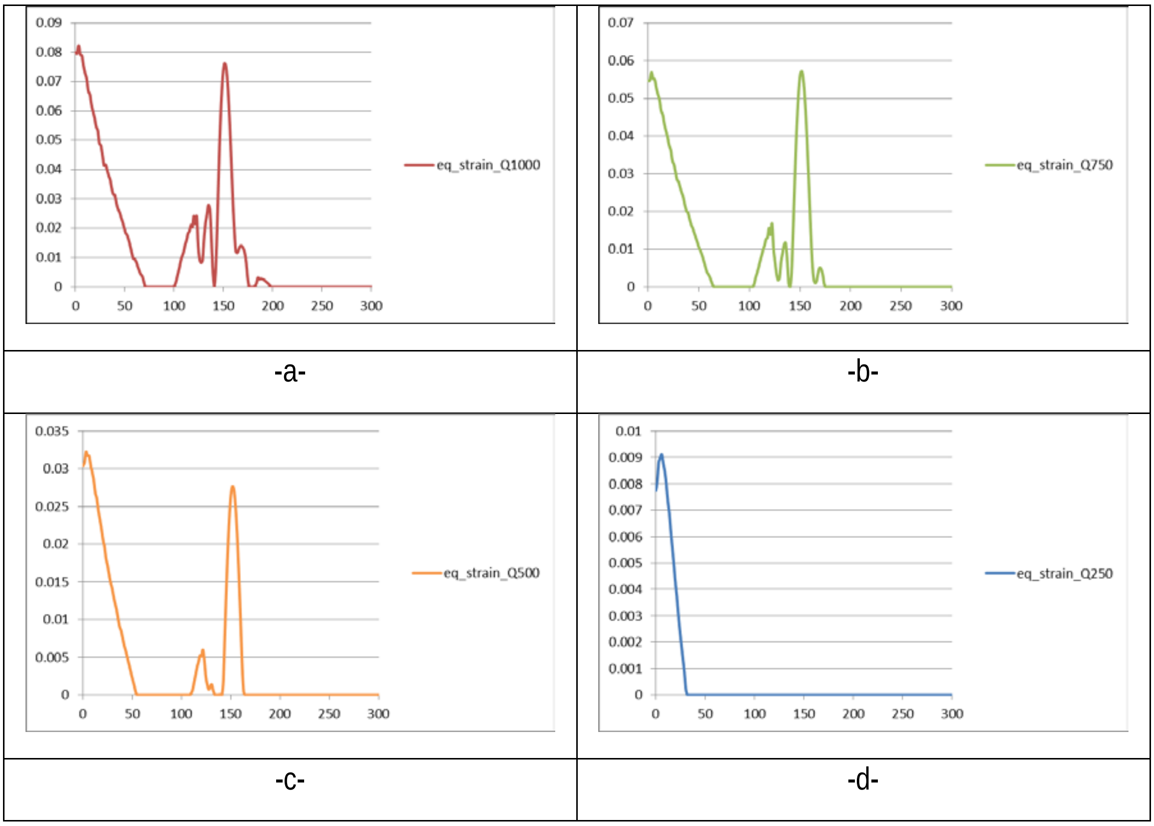

-a- -b-

-c- -d-

Figure 44: Plastic equivalent strain in the thin M2 layer for DLC 1.5 µm and several loads Q

Figure 44 shows the equivalent strain in the thin M2 steel. The influence of the boundary is evident at the beginning of the graph (0-60 µm) as for the thickest coating. At the region of the blister, the plastic strain reaches an unrealistic value of 7.7%. This extremely high plastic strain is due partly to the limited strain hardening and perfect isotropy considered in present model. Nevertheless, very high local plastic strains and moreover a width of more than 100µm affected by significant yielding tend to show the severe local deformation experienced by the steel close to existing “debondings”. Even ahead of the blister severe plastic strain (2.4%) are predicted. A similar behavior is noticed for the loads of 750 and 500 N. The lowest loading (250 N) seems not to cause plastic yielding at the steel (44d).

4.4.2.3 The thin DLC coating

The thinnest DLC coating was modeled as the previous ones and several loads were applied. The initially delaminated zone of 2R=30 µm shown the following results.

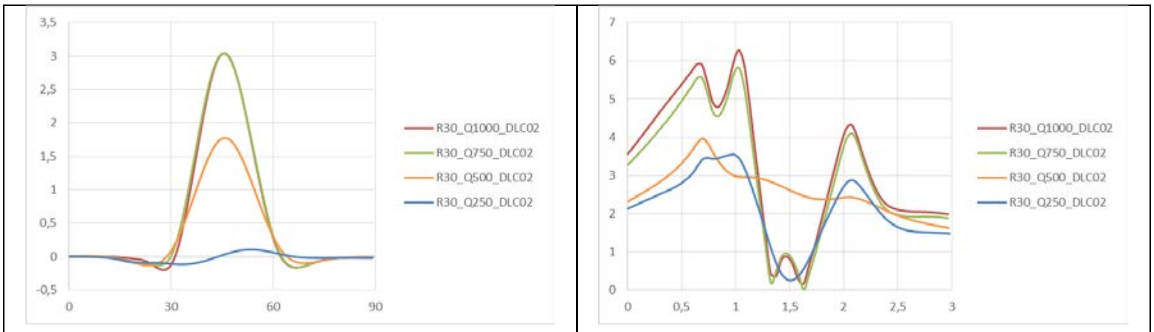

-a- -b-

Figure 45: Predicted deflection of a blister with an initial debonded zone of 30 μm (a) and the stress value parallel to the loading direction (b)

The two highest loads overestimate largely the resulting deflection (almost 40%). However, the load case of 500 N. is in total agreement with the AFM measurements giving a deflection of 1.7 μm. The last load does not lead to important deflection of the film. Similarly to the thickest coating, the high loads (750 and 1000 N) result in stresses on the blister which cross the materials limits. Thus, failure is supposed to be present.

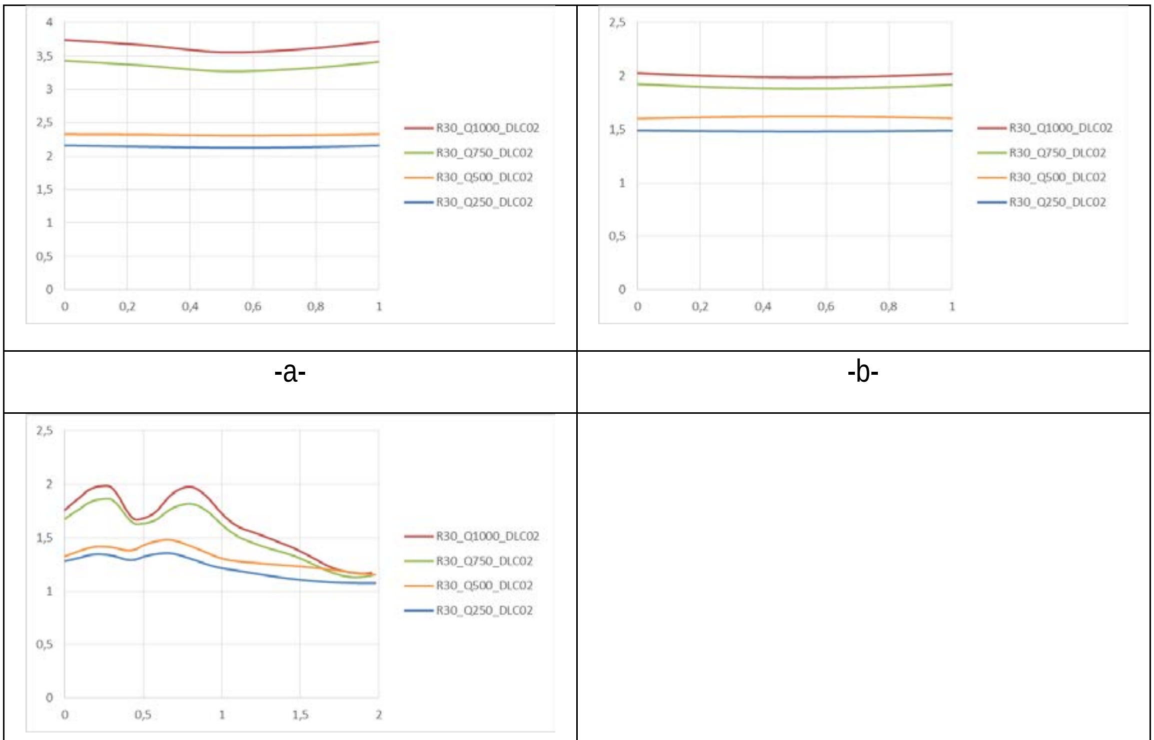

-a- -b-

-c-

Figure 46: Stress distribution prior (a), behind (b) and above (c) the delaminated area (30 μm).

Stresses prior to the buckled blister seem to be higher than the other two thicker coatings (44a). However, they decrease behind the blister. For the highest loads, the stress field above the blister is no longer homogeneous (44d).

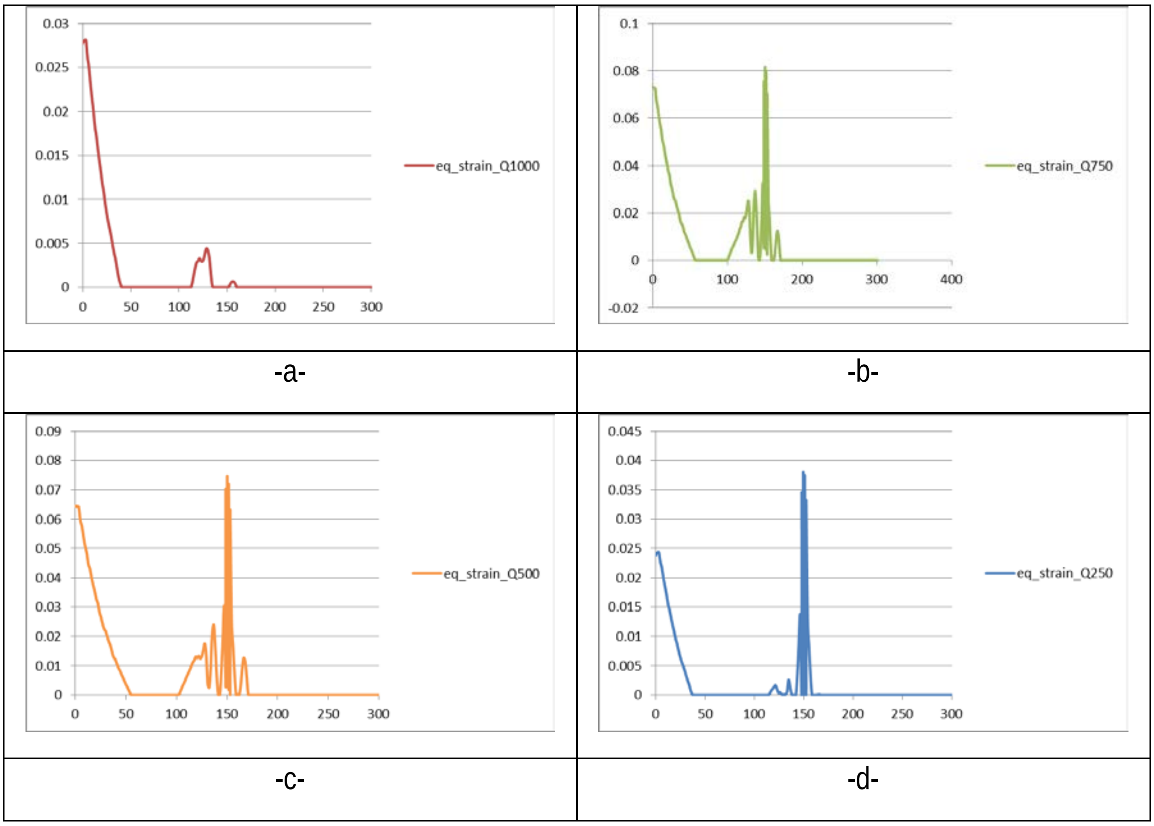

-a-

-b-

-c-

-d-

Figure 47: Plastic equivalent strain in the thin M2 layer for DLC 0.2 μm and several loads Q

Observing the equivalent plastic strain we notice a plastic strain varying between 3.7 and 8.1%. On the contrary, the model predicts a plastic strain of 0.4% for the highest load (47a). Considering the more severe loading of this case, this result is treated as not realistic.

4.4.3 Interface behavior of the DLC/M2 steel system

4.4.3.1 The thick DLC coating interface behavior

The evolution of failure in the interface of the 2.5 μm DLC coating for a load Q=1000 N is presented in figure 48. The mechanism seems to be identical to the one of model 1.

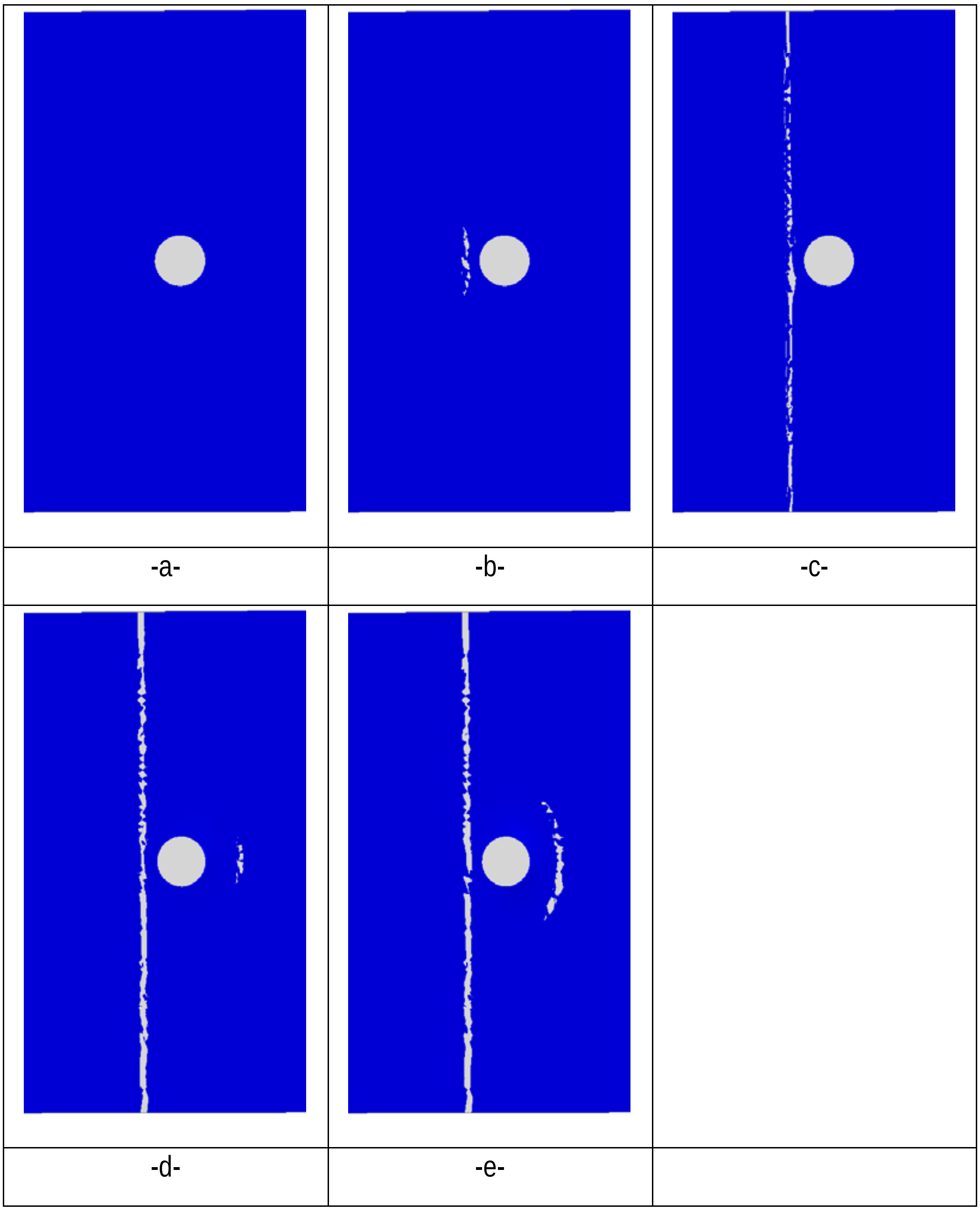
-a- -b- -c-

-d- -e-

Figure 48: Evolution of interface failure of the DLC 2.5 μm for Q=1000 N

Failure starts in front of the blistered zone and propagates perpendicular to the applied load (figure 48). Then damage of the interface takes place behind of the blister and starts to growth (48e).

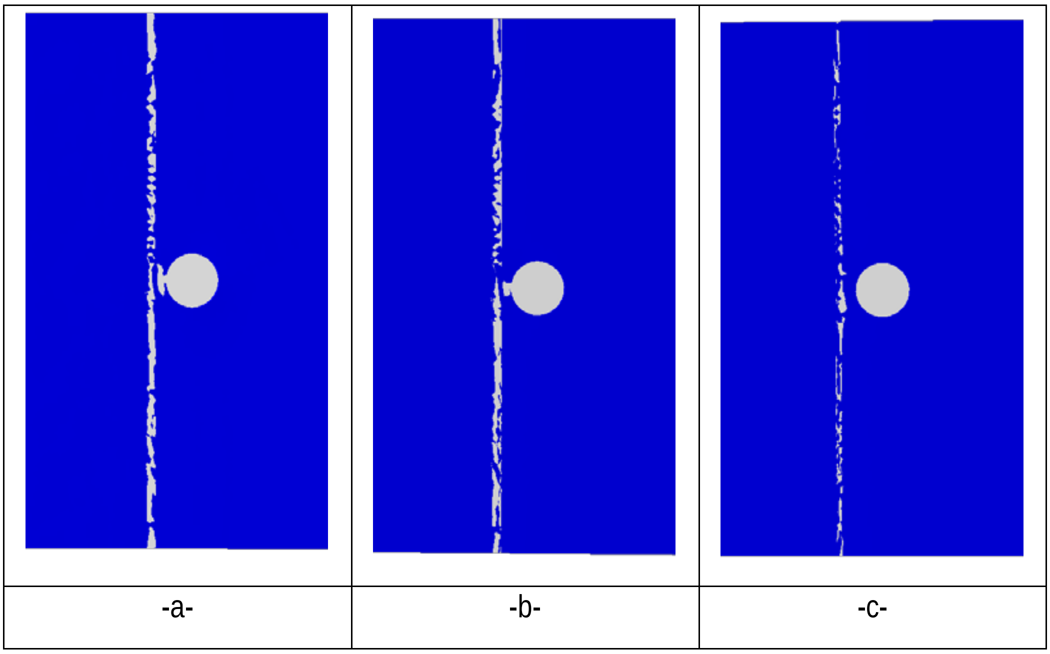

-a- -b- -c-

Figure 49: Final state of the interface of the DLC 2.5 µm for Q 750 N (a), 500 N (b) and 250 N (c)

Concerning the other applied loads, interface failure seems to depend linearly on the applied load Q. The higher the load, the larger the debonded zone (47a).

4.4.3.2 The intermediate DLC coating interface behavior

The intermediate coating's interface for an applied load of 1000 N presents a slightly different behavior to the previously discussed situations. The basic mechanism of damage initiation is the same as before. However, after failure initiation behind the blister, a second band of damaged interface extends parallel to the principal one (figure 50i).

Loads between 750 and 250 N lead to a limited debonding of the interface which reduces with the decrease in the external load Q (figure 51).

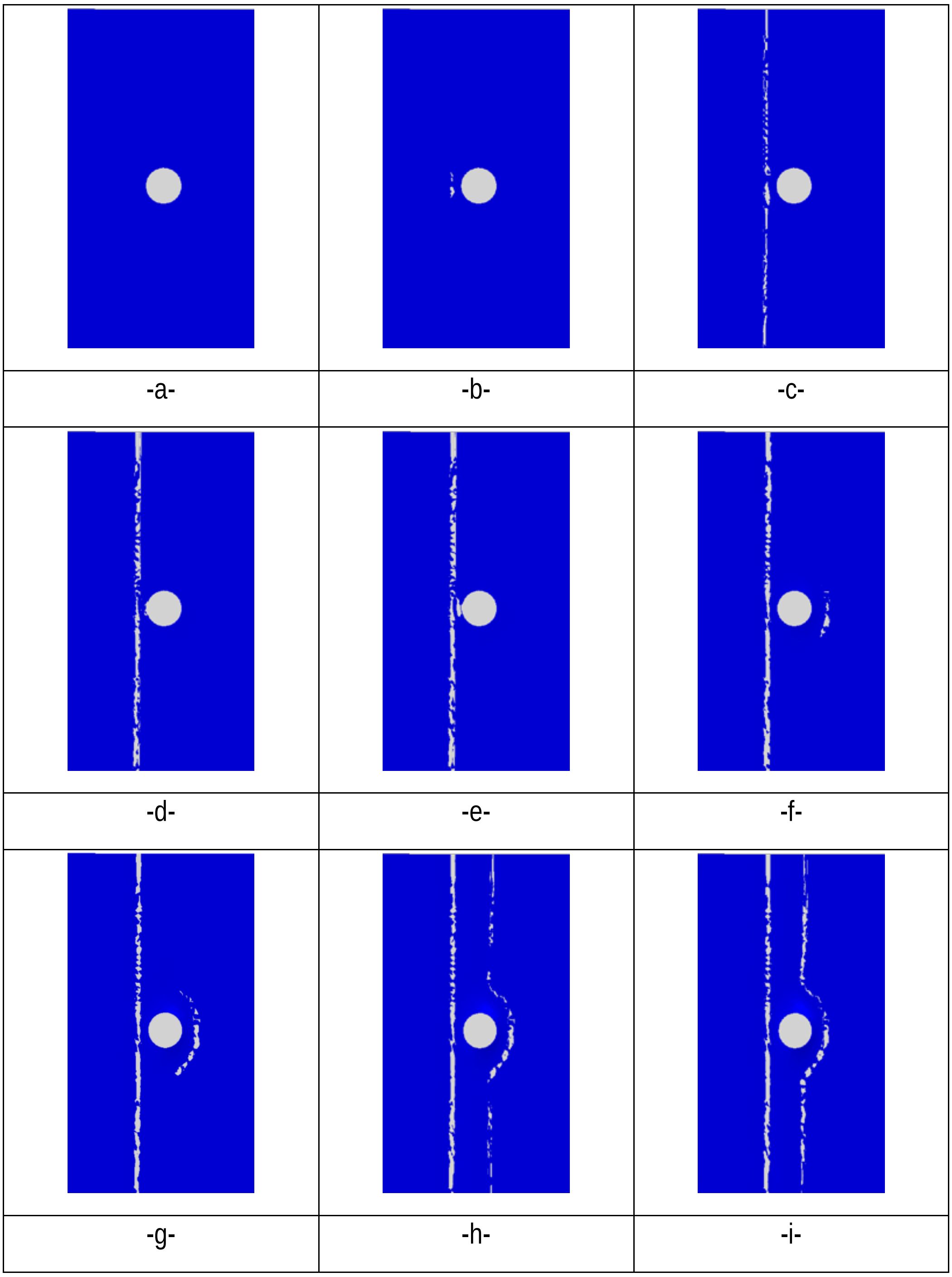

-a- -b- -c-

-d- -e- -f-

-g- -h- -i-

Figure 50: Evolution of interface failure of the DLC 1.5 μm for Q=1000 N

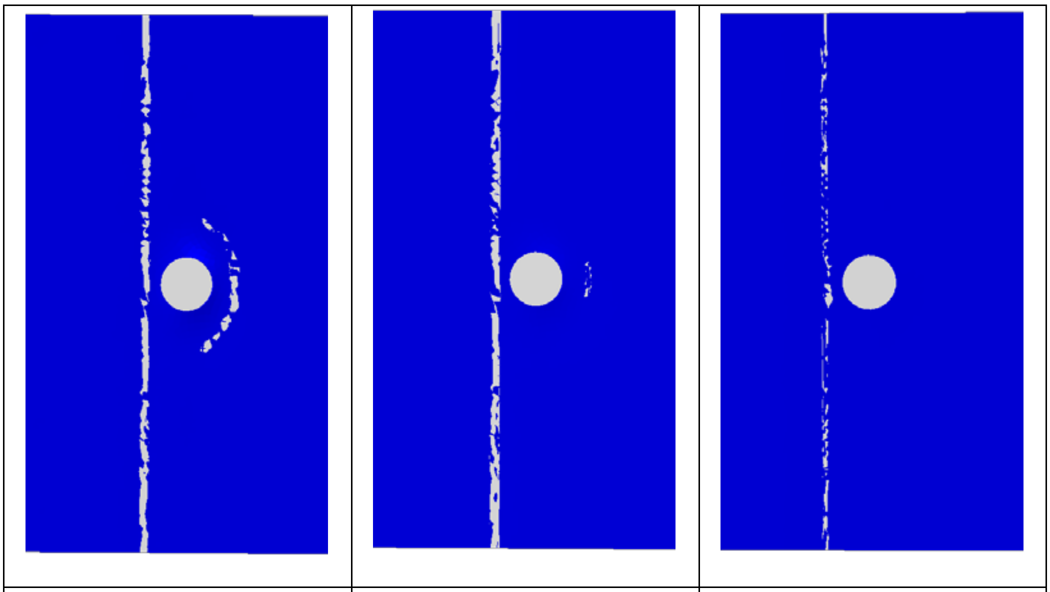

-a- -b- -c-

Figure 51: Final state of the interface of the DLC 1.5 µm for Q 750 N (a), 500 N (b) and 250 N (c)

4.4.3.3 The thin DLC coating interface behavior

Finally, the behavior of the interface of the thinnest coating will be examined. Same loads are applied as all the other cases.

The load of 1000 N results in a similar damage mechanism to the coating of 1.5 µm for the same load. A second delaminated band is present at the interface (52e).

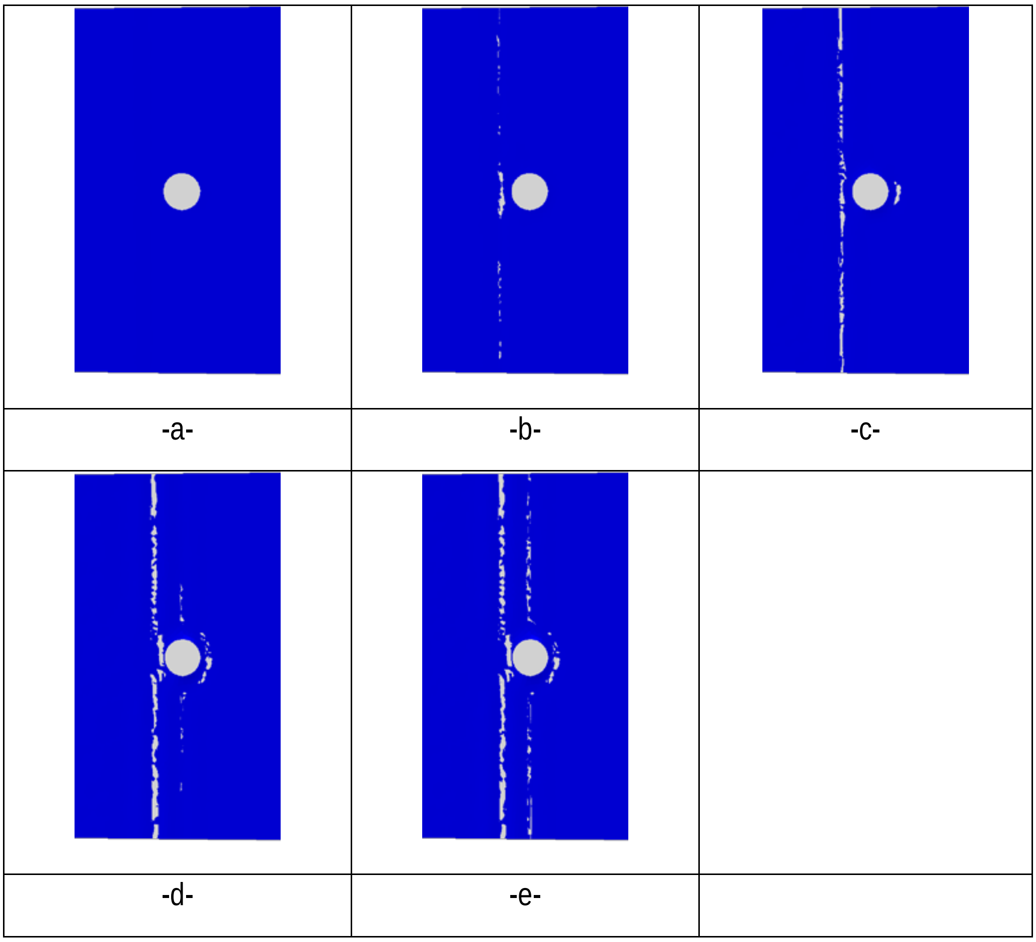
-a- -b- -c-

-d- -e-

Figure 52: Evolution of interface failure of the DLC 0.2 µm for Q=1000 N

Interface failure for the load of 750 N is identical to those of the intermediate DLC coating. Debonding is apparent behind the bister zone.

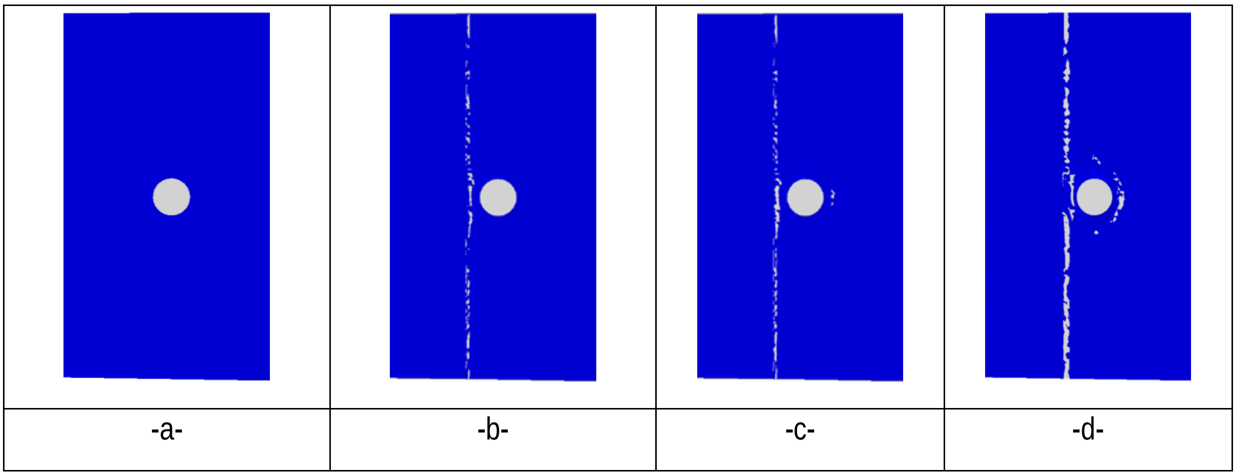
-a- -b- -c- -d-

Figure 53: Evolution of interface failure of the DLC 0.2 µm for Q=750 N

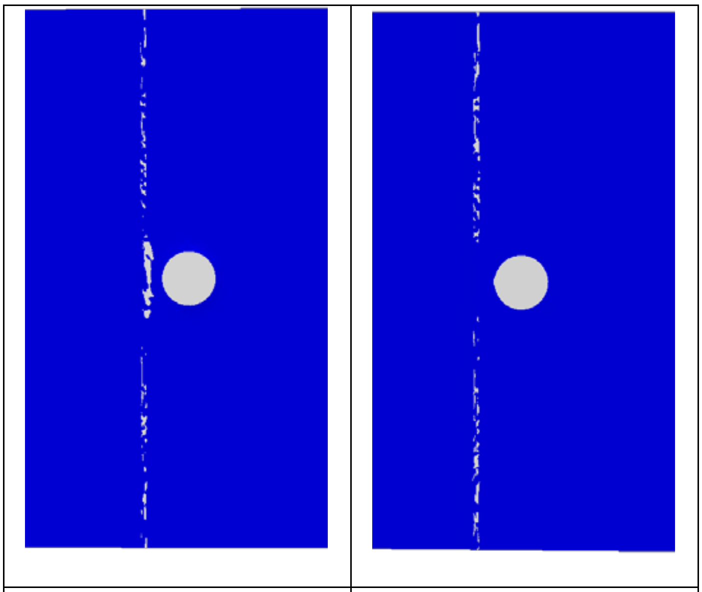

-a- -b-

Figure 54: Final state of the interface of the DLC 0.2 µm for Q 500 N (a) and 250 N (b)

On the contrary, the lower loads cause only failure propagation in front of the blister and not behind.

4.5 Contact stress field determination during DLC coating tribological testing

In order to simulate the stress field during the tribological experiment presented in chapter 2 and investigate crack initiation in the substrate, a 2D model was developed. A schematic representation of the model is given in figure 55.

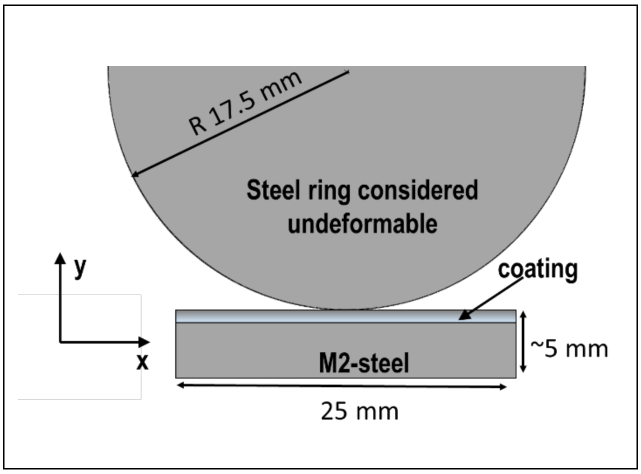

Figure 55: Contact modeling of the DLC-M2 steel system

This model consists of for main parts: a rigid cylindrical ring of radius 17.5 mm, a thin DLC layer, an interface having the same cohesion as in the other models and the M2 steel part (Ø25 and t=5mm). The steel is assumed elasto-plastic. The elasto-plastic steel and elastic DLC layer have properties identical to the ones considered previously, but a very small mesh size is used. All parts except the DLC are meshed with 6 µm wide elements. The coating is meshed with 1.7 µm wide elements. Of course, the residual stress of the film was taken into account. The imposed displacement of the rigid ring was calculated based on Hertz's theory for the contact between a plane with a cylinder and found to be ~1 µm. Two different DLC layer thicknesses were tested (2.5 and 1.5 µm).

Model with DLC 2.5 µm

Figure 46 shows the results corresponding to a 2.5µm thick DLC coating. The contact pressure and the stresses beneath the surface of the M2 steel are plotted. The contact pressure field is illustrated in figure 56a. It is slightly higher than the value predicted by Hertz' theory (530 MPa).

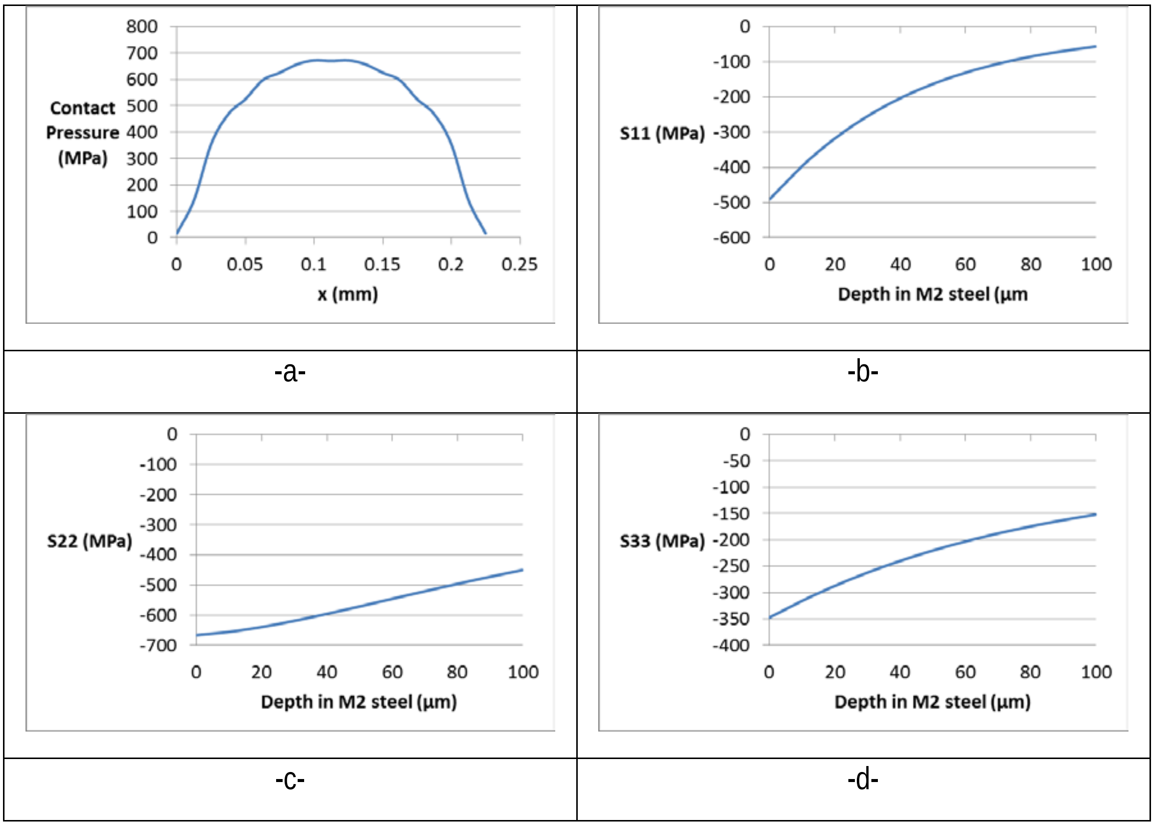

Figure 56: Contact pressure and stress state at the M2 steel

Model with DLC 1.5 µm

In the case of the 1.5 µm thick coating, the same approach was followed.

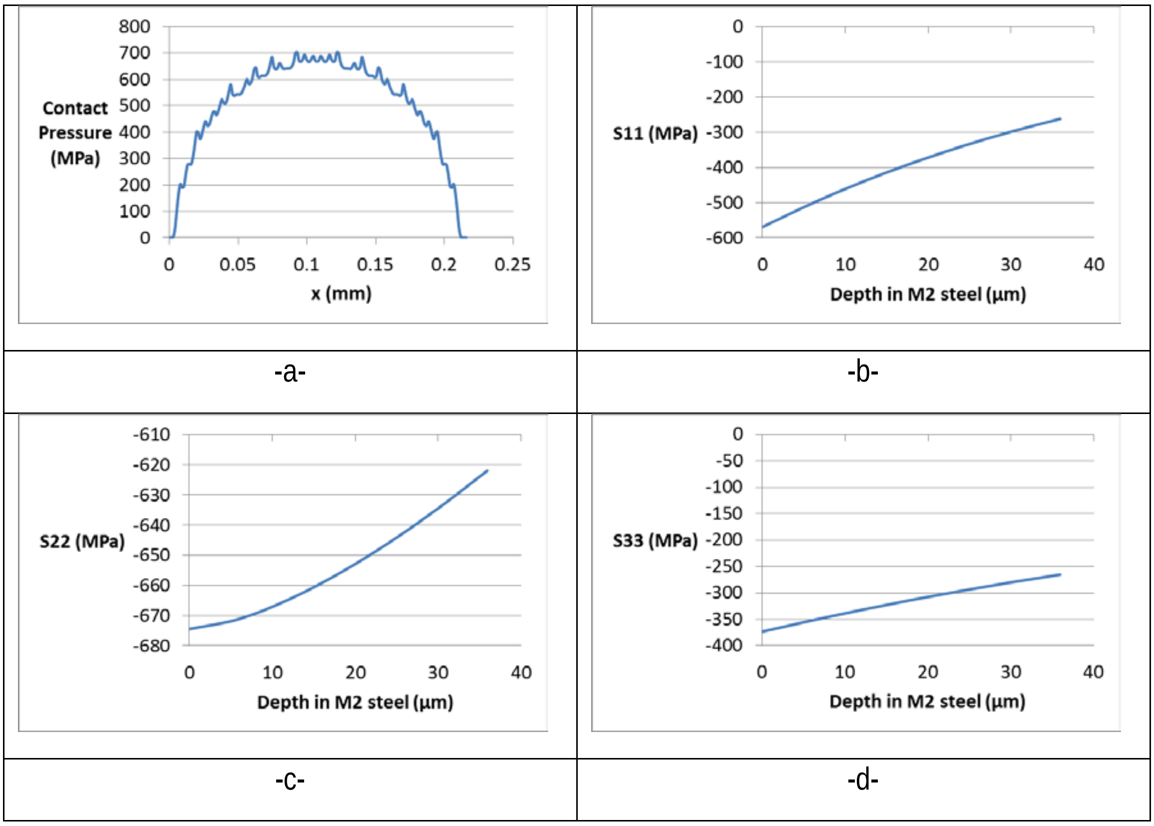

-a-

-b-

-c-

-d-

Figure 57: Contact pressure and stress state at the M2 steel

As shown in figure 57a, the contact pressure field is similar to the thicker DLC film case. Stress components are not higher than the yield stress of the M2 steel and consequently no failure is possible due only to the contact loading.

Figure 58 shows the most significant result of present approach. The von Mises stress for both coating thicknesses is depicted. The von Mises stress is much smaller than the yield stress. Thus the steel is elastic. Refining the mesh leads to more reliable numerical results. But, the real behavior (observed experimentally) corresponds to crack nucleation inside the M2-steel and propagation along the M2-steel/coating interface.

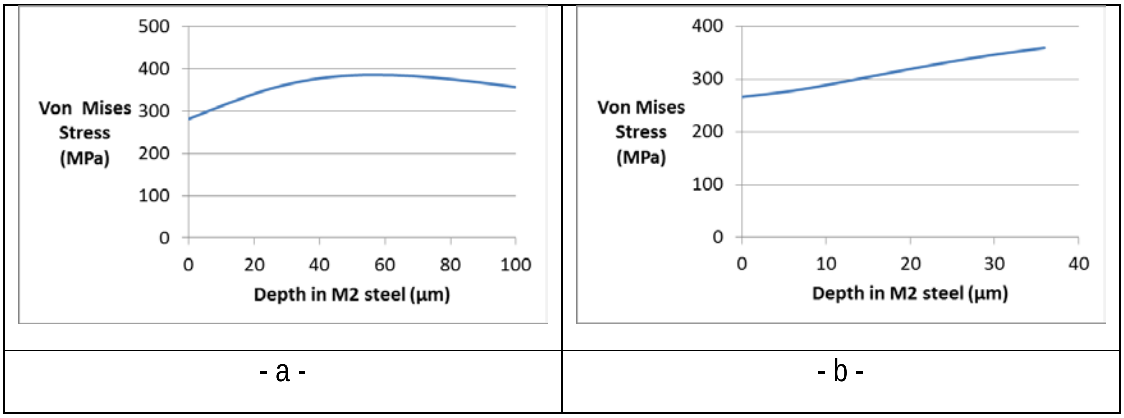

- a -

- b -

Figure 58. Von Mises stress in the M2-steel for two different coating thicknesses (a) 2.5µm and (b) 1.5µm.

The fact, of an elastic steel behavior without the presence of an initial defects only confirms the significance of local variations in the steel microstructure. Effectively, initial defects may correspond either to an initial crack (smallest possible local hardness) or on the other side the presence of a very hard carbide.

4.6 Conclusions

In this chapter, a first attempt to model the stress field and the debonding caused by existing debonded regions was made. First, Hertz elastic contact model between a cylinder and a plane surface was used to estimate the contact zone and thus the area the most affected. In order to analyze blister growth and propagation in thin hard DLC films, three simple models were built. All models consider the existence of a circular debonded region.

In the first model, a single defect in form of a debonded area, at the coating/steel interface is considered. The Finite Element simulation with a single initially debonded region lead to some major conclusions. The stress distribution clearly favors blister extension in the friction direction. To reach blister deflections determined by AFM, very high local values of the friction load have to be considered. This huge frictional load needed to reproduce AMF-measured blister deflections seems to confirm significant wear, and, hence a locally increased friction coefficient, prior to debonding. This would correspond to blistering observed outside the wear trace. Debonding behind the blister in the friction direction is favored. Hence, once more the tendency to form arrangements aligned in the friction direction is suggested. The close correspondence with the AFM data as well as the debonding patterns obtained with a single defect model highly encouraged the development of a multiple defect model.

In the second model, blister interaction was investigated by considering multiple initial defects, i.e. debonded areas. The major outcomes of this model may be summarized as follows. Initial defects (debonded zones) aligned along the friction direction and aligned in the orthogonal direction were considered. Alignment in the friction direction leads to a shielding effect of the front blister. The front defect will grow faster than the defects behind. On the contrary, alignment along an orthogonal direction leads to increased blister growth. Blister interaction may be interpreted by an increased remote stress for each single blister.

The third model addressed crack propagation inside the M2 steel as noticed experimentally. For that reason, a thin layer (~nm) of steel is placed beneath the DLC coating. Blister growth is favored compared to interface crack propagation. The most significant result of this model is that an initial defect inside the M2-steel leads significant yielding. Even, if the values predicted by this model have to be treated cautiously, the tendency of significant yielding opens a new field. Definitely, contact modelling at the grain scale based on crystal plasticity is needed as the next step.

Finally, the stress field during the tribological contact of the DLC coating was determined by a simple 2D model. Nevertheless, the stresses inside the steel do not seem elevated enough to cause yielding of the material. The steel remaining elastic highlights previous statements. Evidently, mesh refinement is not the solution to analyze contact problems, but considering defects inside the steel and allowing significant, but realistic yielding. This clearly requires to adapt the contact models to different scales. At the macroscopic scale, the classical Hertz model gives reliable results. The stress field predicted by this theory has to be applied at a local scale taking into account several probable initial defect distributions. These defects may correspond to a small crack or at the other end of the hardness scale a carbide. Of course, TEM observations have to inspire the local models. The stress field close to these defects should finally be used in crystal plasticity calculations. These steps were, unfortunately, far beyond the scope of present PhD.

General Conclusions

In this PhD, DLC coatings behavior deposited onto M2 steel substrate was investigated experimentally and by mechanical models.

For the experimental investigation, M2-steel samples were coated with a WC-interlayer and different DLC thicknesses reaching from 0.2µm to 2.5µm. The samples were submitted to severe tribological loading to simulate their behavior and test the adherence of the interface. But, prior to any external loading, the DLC coating/M2 steel substrate system characteristics were analyzed. The stress-strain curve of the DLC film was obtained as well as its hardness by means of nanoindentation and micro-pillar compression. Young's modulus, hardness and yield stress were determined with high accuracy. DLC micro-pillars exhibit small but significant strain hardening. Moreover, FIB cross-sections revealed the intact interface of the structure after film deposition. No SEM-visible decohesion was detected. This part led essentially to the development of very valuable technical knowhow. The nano-pillar compression in a very thin coating assumes a close control of the technical conditions as well as FIB cross-milling leaving a very neat surface. If the micro-hardness of the DLC was known prior to this work, the stress strain curves are completely novel.

Residual stresses were measured by Stoney's method to vary between -0.8 GPa for the interlayer and -2.0 GPa for the thick DLC coating (2.5 µm). The absolute stress values increases linearly with film thickness. Parallel a method to determine the residual stress by the deflection of FIB-milled beams was used on the thickest DLC. This method following techniques suggested in the literature, lead to the same stress values as determined by Stoney's method on Si-wafers.

After very extensive and careful characterization of the coatings, samples were submitted to a tribological test with in situ measurement of the friction coefficient on a tribometer used to qualify films for the automotive industry. After tribological loading, debonding, delamination and interface failure were analyzed. SEM observation of the coating after severe tribological loading show blisters forming a network and being oriented in the friction direction. This result cannot be reproduced by Rockwell indentation or scratch tests because they operate in a smaller order of magnitude. In addition, blisters presenting cracks in their borders were detected.

FIB observations of several blisters cross-sections revealed crack initiation in the substrate material. This was validated by local chemical EDX analysis which shows the presence of iron (Fe) in the layer of material attached beneath the interlayer. This completely new result opens a field of future developments. The influence of the substrate surface preparation should be analyzed. Fatigue induced local yielding may also plays a role. Preparation of thin specimens at the contact zone to be observed with by TEM seems useful new investigation.

Cracks are found to deviate at the vicinity of the carbides. Thus, the local M2 steel microstructure controls crack propagation. This novel finding could lead to the optimization of the coating/substrate couple. A systematic study is needed, correlating the size of carbides and their spatial distribution to crack deviation.

Neighboring blisters interact with each other. During FIB milling they often coalesce and form a larger delaminated area. This analysis is only possible with the present tribological experiment. Actually, this interaction can be observed by loading a minimum area of material. It could be interesting to make a statistical analysis of the surface defects prior external loading and their relationship to the regular spacing of the blisters after tribological loading.

The main novel experimental results can be summarized as follows :

- Blister nucleation inside the M2-steel
- Blisters form a network and elongated in the friction direction
- Blisters interact strongly and eventually coalesce
- The blister borders are partially cracked.

The last part of present PhD was dedicated to several mechanical models trying to explain the experimental results. One major drawback of all finite element model concerning coatings is the very huge number of elements needed due to the different lengths scales. Hence, the first step consisted in a simple application of the well-known Hertz contact theory to determine the size of the contact zone. This rough estimate was then used to determine the zone were mesh-refinement was needed. With this information, three models were considered. As interface crack nucleation was observed to occur inside the M2-steel, we decided right from the beginning not to address crack nucleation but only the effect of an existing “crack”. Thus, all models consider an existing “debonded” area. The first model is dedicated to the analysis of a single blister with a crack at the DLC-steel interface. The second model considered multiple blister interaction for the same interface cracks position, i.e. at the interface. Finally the 3rd model considers an “interface” crack some nm inside the M2-steel.

The main conclusions of the different models may be summarized as follows :

- Single blister growth is favored by a crack inside the M2-steel compared to a crack at the steel coating interface
- Very high local friction loads are needed to produce blisters corresponding to AFM-measurements
- Blister interaction favors growth of existing blisters in the friction direction.

Present PhD has answered the question where debonding and subsequent delamination occurs. Moreover, the results show the validity of the tribological test to characterize coating wear. Blister growth and interaction were modelled satisfyingly. But, why blister nucleate is still an open question. Some indications are given. Probably very significant yielding occurs in a very thin strip of steel. This point should be addressed by local contact models based on crystal plasticity in a future work.

École Nationale Supérieure des Mines

de Saint-Étienne

NNT : *Communiqué le jour de la soutenance*

Antonios CHOLERIDIS

EXPERIMENTAL AND MECHANICAL ANALYSIS OF WEAR INDUCED DELAMINATION FOR DLC COATED AUTOMOTIVE COMPONENTS

Speciality: Materials Science and Engineering

Keywords: DLC, In situ Wear, Delamination, Finite Element Analysis

Abstract:

DLC coatings behavior deposited onto M2 steel substrate was investigated experimentally and by mechanical models. M2-steel samples were coated with a WC-interlayer and different DLC thicknesses. After extensive characterization (residual stresses, micro-pillar compression), the samples were submitted to severe tribological loading to test the adherence of the interface.

SEM observations of the coating after tribological loading show blisters (with partially cracked borders) forming a network oriented in the friction direction. This result cannot be reproduced by Rockwell indentation or scratch tests. FIB observations of several blisters, combined with local chemical analysis by EDX, revealed crack initiation inside the substrate material. Neighboring blisters interact with each other. During FIB milling they often coalesce and form a larger delaminated area.

The last part of present PhD was dedicated to several mechanical models. First, the well-known Hertz contact theory allowed to determine the contact area. Based on this rough estimate, mesh-refinement was defined for three models. All models assume an existing “debonded” area. The first model is dedicated to the analysis of a single blister with a crack at the DLC-steel interface. The second model considered multiple blister interaction for the same interface crack position. Finally the 3rd model considers an “interface” crack some nm inside the M2-steel.

The main conclusions of the different models may be summarized as follows:

- Single blister growth is favored by a crack inside the M2-steel
- Very high local friction loads are needed to produce blisters
- Blister interaction favors growth of existing blisters in the friction direction.

Present PhD answered the question where debonding and subsequent delamination occurs. Moreover, the results show the validity of the tribological test to characterize coating wear. Blister growth and interaction were modelled satisfyingly

École Nationale Supérieure des Mines

de Saint-Étienne

NNT : Communiqué le jour de la soutenance

Antonios CHOLERIDIS

ANALYSE EXPERIMENTALE ET MODELISATION MECANIQUE DU DELAMINAGE DE DEPOTS DLC SUR DES COMPOSANTS AUTOMOBILES

Spécialité: Science et Génie des Matériaux

Mots clefs : DLC, in situ, usure, délaminage, éléments finis

Résumé :

Le comportement de revêtements DLC sur un substrat en acier M2 avec une couche intermédiaire en WC a été étudié expérimentalement et par des modèles mécaniques. Après une caractérisation poussée (contraintes résiduelles, compression des micro-piliers), les échantillons ont été soumis à un chargement tribologique.

Des observations post mortem au MEB montrent des cloques (avec des bords partiellement fissurées) formant un réseau orienté dans la direction du frottement. Ce résultat ne peut pas être reproduit par les tests d'indentation ou de Rockwell. Les observations FIB de plusieurs blisters, combinées à une analyse chimique locale par EDX, ont révélé une initiation de fissure à l'intérieur du substrat. Les blisters voisins interagissent les uns avec les autres. Pendant la découpe FIB, ils coalescent pour former une zone délaminée plus grande.

La dernière partie de la thèse est consacrée à 3 modèles éléments finis supposant l'existence d'une zone délaminée et un raffinement du maillage basé sur le modèle de Hertz. Le premier modèle considère un seul blister avec une fissure à l'interface acier-DLC. Le second modèle suppose l'existence de plusieurs blisters. Enfin, le 3ème modèle suppose une fissure quelques nm à l'intérieur de l'acier M2. Les principales conclusions des différents modèles peuvent être résumées comme suit:

● La formation de blisters simples est favorisée par une fissure à l'intérieur de l'acier M2.

● De très fortes charges de frottement locales sont nécessaires pour produire des blisters

● L'interaction des blisters favorise leur croissance dans le sens du frottement.

La thèse a répondu à la question où se produisent le décollement et le délaminage ultérieur. De plus, les résultats montrent la validité du test tribologique pour caractériser l'usure des revêtements. La croissance et l'interaction des cloques ont été modélisées de manière satisfaisante.